Liquid State Physics of the MgO-SiO$_2$ System at Deep Mantle Pressures

by

Nico Pieter Jan de Koker

A dissertation submitted in partial fulfillment
of the requirements for the degree of
Doctor of Philosophy
(Geology)
in The University of Michigan
2008

Doctoral Committee:

Professor Lars P. Stixrude, Co-chairperson
Professor Rebecca A. Lange, Co-chairperson
Professor John Kieffer
Professor Larry J. Ruff
Associate Professor Udo Becker

To Johan, Verelene and Estelle

ACKNOWLEDGEMENTS

Most importantly, my sincere gratitude to Lars Stixrude. I feel truly privileged to have had the opportunity to work under his guidance. He always challenged me, while affording me the freedom to explore and experiment. I continue to be inspired by the depth and breadth of his knowledge and skill, and the clarity with which he willingly shares this with students.

I am deeply grateful to my MSc advisor, Carolina Lithgow-Bertelloni, who selflessly encouraged me as I became increasingly fascinated by mineral physics. I wish her and Lars the greatest success and happiness in London.

Discussions with Larry Ruff, Udo Becker and Becky Lange invariably deepened my insight and broadened my perspective. I'd like to thank Becky for stepping in as co-chair when the need arose. I also appreciate the willingness of John Kieffer in Material Science and Engineering to serve as cognate member of my committee.

I further wish to acknowledge the help and support of my collaborators, Bijaya Karki at LSU, Stephen Stackhouse, Mainak Mookherjee and Ni Sun. Bijaya gave valuable input on the manuscripts presented in Chapters II and IV.

Finally, I would not have ventured abroad without the encouragement and sincere interest shown by Lew Ashwal, Chris Engelbrecht and Sue Webb. This dissertation is a confluence of the interests in petrology, condensed matter physics and global geophysics they instilled in me as an undergraduate.

TABLE OF CONTENTS

DEDICATION . . . . **ii**

ACKNOWLEDGEMENTS . . . . **iii**

LIST OF FIGURES . . . . **vi**

LIST OF TABLES . . . . **viii**

LIST OF APPENDICES . . . . **ix**

CHAPTER

I. Introduction 1

II. Thermodynamics, Structure, Dynamics, and Freezing of Mg_2SiO_4 Liquid at High Pressure 8

- 2.1 Abstract 8
- 2.2 Introduction 9
- 2.3 Computational Technique 11
- 2.4 Results 17
  - 2.4.1 Equation of State 17
  - 2.4.2 Melting Curve 18
  - 2.4.3 **Mg_2SiO_4** Hugoniot 19
  - 2.4.4 Liquid Structure 20
  - 2.4.5 Transport Properties 22
- 2.5 Discussion 23
- 2.6 Conclusions 28
- 2.7 Acknowledgements 29

III. Self-Consistent Thermodynamic Description of Silicate Liquids, with Application to Shock Melting of MgO **Periclase and** $MgSiO_3$ **Perovskite** 48

- 3.1 Abstract 48
- 3.2 Introduction 49
- 3.3 Previous Work 50
- 3.4 Fundamental Thermodynamic Relations 52
  - 3.4.1 Liquids 54
  - 3.4.2 Solids at High Temperature 57
- 3.5 First Principles Molecular Dynamics Simulations 59
- 3.6 Results 62
  - 3.6.1 Liquids 62
  - 3.6.2 Solids 64

3.7 Applications . . . 64
3.8 Discussion . . . 67
3.9 Conclusion . . . 71
3.10 Acknowledgements . . . 72

IV. Structure and Mixing of Liquids on the $\mathrm{MgO-SiO_2}$ Join and the Origin of Liquid Immiscibility . . . 94

4.1 Abstract . . . 94
4.2 Manuscript . . . 95
4.3 Acknowledgements . . . 99

V. Conclusion . . . 106

APPENDICES . . . **110**

BIBLIOGRAPHY . . . **118**

LIST OF FIGURES

Figure

1.1 Ambient pressure phase diagram of the MgO-SiO_2 join . . . 7
2.1 Snapshots of the simulated liquid at 3000 K, for $V/V_X = 1.0$ and $V/V_X = 0.5$ . . . 35
2.2 Equation of state of liquid Mg_2SiO_4 . . . 36
2.3 (a) Isochoric heat capacity (C_V) and (b) Grüneisen parameter (γ) of liquid (red circles) and forsterite (green squares) as a function of volume . . . 37
2.4 First principles melting curve for forsterite . . . 38
2.5 Density contrast expected during incongruent melting of forsterite . . . 39
2.6 Theoretical Hugoniot for Mg_2SiO_4 liquid . . . 41
2.7 (a) Si-O and Mg-O coordination, and (b) Si-O bond lengths as a function of volume 42
2.8 Polymerization state of the liquid as a function of volume, at 3000 K and 6000 K, as expressed by the abundance of $_{[Z]}\mathrm{Si}^{\mathrm{O}_B}$ species . . . 43
2.9 Free and bridging oxygen abundance as a function of Si-O coordination . . . 44
2.10 Time series of atomic movement within a 3.5 Å sphere relative to a reference silicon atom, illustrating dynamic speciation changes . . . 45
2.11 Mean square displacement as a function of time . . . 46
2.12 Self-diffusion coefficient (D_N) of Mg_2SiO_4 liquid, fit with an Arrhenius relation (equation 2.19) . . . 47
3.1 Pressure (P), internal energy (E) and thermal electronic entropy (S_{el}) of MgO liquid 81
3.2 Pressure (P), internal energy (E) and thermal electronic entropy (S_{el}) of Mg_2SiO_4 liquid . . . 82
3.3 Pressure (P), internal energy (E) and thermal electronic entropy (S_{el}) of $MgSiO_3$ liquid . . . 83
3.4 Pressure (P), internal energy (E) and thermal electronic entropy (S_{el}) of SiO_2 liquid 84
3.5 Grüneisen parameter (γ) and isochoric heat capacity (C_V) for the respective liquid compositions . . . 86
3.6 Thermodynamics of vaporization in Mg_2SiO_4 liquid . . . 87
3.7 Pressure (P) and internal energy (E) of MgO periclase . . . 88
3.8 Pressure (P) and internal energy (E) of $MgSiO_3$ perovskite . . . 89
3.9 Shock melting of MgO periclase . . . 91
3.10 Shock melting of $MgSiO_3$ perovskite . . . 93
4.1 Silicon ($Z_{\mathrm{Si-O}}$) coordination and Grüneisen parameter (γ) along the MgO-SiO_2 join 102
4.2 The distribution of oxygen species at 6000 K and 136 GPa (top), and 3000 K and 0 GPa (bottom) . . . 103
4.3 Liquid density along the MgO-SiO_2 join . . . 104
4.4 Enthalpy and volume of mixing along the MgO-SiO_2 join . . . 105
B.1 Pressure (P), internal energy (E) and thermal electronic entropy (S_{el}) of Mg_5SiO_7 liquid . . . 114
B.2 Pressure (P), internal energy (E) and thermal electronic entropy (S_{el}) of $Mg_3Si_2O_7$ liquid . . . 115
B.3 Pressure (P), internal energy (E) and thermal electronic entropy (S_{el}) of $MgSi_2O_5$ liquid . . . 116

B.4 Pressure (P), internal energy (E) and thermal electronic entropy (S_{el}) of $MgSi_3O_7$ liquid . . . 117

LIST OF TABLES

Table

2.1 Equation of state fit parameters for equations 2.4-2.13 30
2.2 Comparison of liquid equation of state to experimental data at 2163 K, 0 GPa . . . 31
2.3 Comparison of crystalline equation of state with experimental values computed from the model of Stixrude and Karki (2005) at 1000 K, 0 GPa 32
2.4 Comparison of simulated liquid structure to experimental data (Kohara et al., 2004) 33
2.5 Self-diffusion coefficient Arrhenius relation fit parameters (equation 2.19) 34
3.1 Limiting behavior of excess thermodynamic properties, and values of n and m required for these limits to hold 73
3.2 m values used in liquids F_{xs} fits 74
3.3 Thermodynamic properties of FPMD MgO liquid at 0 GPa, 3000 K 75
3.4 Thermodynamic properties of FPMD Mg_2SiO_4 liquid at 0 GPa, 1773 K 76
3.5 Thermodynamic properties of FPMD $MgSiO_3$ liquid at 0 GPa, 1773 K 77
3.6 Thermodynamic properties of FPMD SiO_2 liquid at 0 GPa, 3000 K 78
3.7 Thermodynamic properties of FPMD MgO periclase at 0 GPa, 2000 K 79
3.8 Thermodynamic properties of FPMD $MgSiO_3$ perovskite at 0 GPa, 2000 K 80
4.1 Thermodynamic properties of mixed liquids on the MgO-SiO_2 join at 0 GPa, 3000 K 100
4.2 Interaction parameters for H_{mix} obtained from fit of Equation 4.2 101

LIST OF APPENDICES

Appendix

A. F_{xs} coefficients 111

B. Equations of state for intermediate composition liquids 114

CHAPTER I

Introduction

The chemical history of a terrestrial planet such as Earth is intimately tied to its thermal history through fractionation processes associated with cooling of a magma ocean and partial melting of a solid mantle. Sufficient energy sources have been identified for the planet to have been entirely molten during the late stages of accretion (Urey, 1955; Tonks and Melosh, 1993; Ruff and Anderson, 1980; Hanks and Anderson, 1969). Seismic observations suggest the presence of partial melt atop the 410 km discontinuity, (Revenaugh and Sipkin, 1994; Song et al., 1994) and at the base of the mantle (Williams and Garnero, 1996; Revenaugh and Meyer, 1997; Garnero and Helmberger, 1995). Also, while decompression melting at mid-ocean ridges occurs at depths of $50 - 200$ km (McKenzie and Bickle, 1988; Asimow et al., 1995), evidence from xenoliths suggests that melt has reached the surface from significantly greater depths (Haggerty and Sautter, 1990; Collerson et al., 2000). Despite this variety of planetary settings where melts play a role, the physics of the liquid phase over the pressure and temperature range relevant to these settings is not well understood. Of especial interest are the transport and thermodynamic properties, and how these relate to the characteristics of liquid structure. Accurate estimates of freezing temperatures can therefore provide key constraints on the composition, thermal profile, dynamics and evolution of the mantle.

The goal of this dissertation is to apply state of the art theoretical methods to elucidate the properties of silicate liquids at pressures and temperatures relevant to the entire extent of the Earth's mantle. First principles methods describe the system directly in terms of the charge density by means of the Hohenberg-Kohn theorem and density functional theory (Hohenberg and Kohn, 1964; Kohn and Sham, 1965, DFT). The method is independent of experimental input, and the underlying theory is equally valid at ambient as well as very high pressure. It has been successfully applied to solids at high pressure (Karki et al., 2001; Stixrude, 2001; Oganov et al., 2001b), and has recently been used to simulate silicate liquids at pressures and temperatures relevant to the entire extent of Earth's mantle (Stixrude and Karki, 2005; Karki et al., 2007; Wan et al., 2007; Trave et al., 2002).

Reasons for focussing on liquids in the MgO-SiO_2 system are as follows. Firstly, MgO and SiO_2 are the two most abundant oxide components in the mantle, and account for a dominant fraction of the composition of a terrestrial magma ocean after core-mantle segregation. Secondly, the system has relatively few valence electrons, enabling extensive investigation of compositional space via computationally intensive first principles molecular dynamics (FPMD) simulations. Finally, the refractive nature of forsterite and periclase has limited the liquid compositions that have been studied experimentally. Our calculations can therefore test the existing extrapolations by which their properties are currently estimated.

The MgO-SiO_2 phase diagram at ambient pressure (Figure 1.1) is experimentally well constrained (Bowen and Andersen, 1914; Greig, 1927; Ol'Shanskii, 1951; Elliott et al., 1963; Riley, 1966; Chen and Presnall, 1975; Hageman and Oonk, 1986). Melts are by their very nature high temperature phenomena, the experimental study of which pose non-trivial technical challenges even at ambient pressure. Partial molar models based on extensive measurement of liquid state density (Lange and Carmichael, 1987; Lange, 1997), heat capacity (Stebbins et al., 1984; Lange and Navrotsky, 1992) and sound speed (Rivers and Carmichael, 1987; Ai and Lange, 2008) at ambient pressures continue to serve as the foundation for the thermodynamic investigation of silicate liquids. With higher pressure, static experiments are limited by progressively smaller sample sizes. Piston cylinder and multi anvil experiments have nonetheless elucidated upper mantle melting phase relations (Boyd et al., 1964; Davis and England, 1964; Ohtani and Kumazawa, 1981; Presnall and Walter, 1993; Presnall and Gasparik, 1990; Presnall et al., 1998; Dalton and Presnall, 1997) and the equations of state (Suzuki and Ohtani, 2003; Ohtani et al., 1993; Agee and Walker, 1993) of liquids in the upper mantle. At lower mantle pressures, melting has been measured with the laser heated diamond anvil cell (Zerr and Boehler, 1993, 1994; Shen and Lazor, 1995; Heinz and Jeanloz, 1987; Knittle and Jeanloz, 1989; Sweeney and Heinz, 1993). Measurement of the high pressure equation of state and melting has recently been made upon shock loading of solid samples (Mosenfelder et al., 2007; Akins et al., 2004; Luo et al., 2004, 2002; Hicks et al., 2006).

As with the experimental studies of liquid thermodynamics, high temperatures also hamper measurement of the structure of silicate liquids, and its response to pressure. The earliest inferences were based on X-Ray diffraction (XRD) studies of glasses (Warren and Biscoe, 1938; Mozzi and Warren, 1969), and later expanded through in situ conductivity (Bockris et al., 1948), XRD (Waseda and Toguri, 1977) and nuclear magnetic resonance (NMR) (Stebbins and Farnan, 1992) studies of liquids. These studies revealed silicate liquids to comprise fourfold coordinated silicon atoms arranged in a network modified to varying extent by other cations (network modifiers) (Bottinga and Weill, 1972). Pressure induced coordination increases were first predicted in analogy to changes in solids (Waff, 1975), and inferred from changes in glass measured by spectroscopy (Williams and Jeanloz, 1988) and NMR (Allwardt et al., 2007). Atomistic simulations have revealed that some liquids also accommodate compression by changing ring statistics (Stixrude and Bukowinski, 1990b).

In spite of the large contributions which these studies have made, large discrepancies exist and important problems remain. These include the pressure and compositional dependence of structural response to compression, the nature of the density contrast between melt and solid, high pressure melting temperatures, the possible presence of immiscibility at deep Earth pressure, as well as identifying the underlying structural response mechanisms responsible for thermodynamic phenomena. The functional form by which to describe liquid state thermodynamics as a function of pressure, temperature and composition also remains the subject of debate. These are the main issues addressed in this thesis.

Mg_2SiO_4 liquid has a high ambient freezing temperature (Bowen and Andersen, 1914, $2163 \pm 25\,\mathrm{K}$) and is very fragile, with the result that its structure has only been inferred from studies of flash quenched glasses (Cooney and Sharma, 1990; Williams, 1990; Kohara et al., 2004), while its thermodynamic properties are only known from extrapolation of partial molar values (Lange and Carmichael, 1987; Stebbins et al., 1984; Rivers and Carmichael, 1987) and from measurements in the super cooled state (Tangeman et al., 2001; Navrotsky et al., 1989). A density crossover within the stability field of olivine has been observed for high Mg-number peridotite melts (Agee and Walker, 1993), but forsterite melting curve measurements are disparate (Ohtani and Kumazawa, 1981; Presnall and Walter, 1993) and show no evidence of a density crossover in Mg_2SiO_4 liquid. However, at much higher pressure ($150 - 200\,\mathrm{GPa}$)

shock density measurements do predict a liquid denser than the solid (Mosenfelder et al., 2007). To shed light on these important issues, the liquid structure, equation of state, Hugoniot, forsterite coexistence curve and transport properties of Mg_2SiO_4 liquid are explored in Chapter II.

Chapter III presents a detailed consideration of the description of silicate liquid thermodynamics over large pressure intervals. The finite strain expansion of the energy (Birch, 1952, 1978) is often used to represent the liquid equation of state (Rigden et al., 1988; Ghiorso et al., 2002; Lange, 2003, 2007; Stixrude and Karki, 2005; Karki et al., 2006, 2007), yet concerns over its suitability for liquids has been raised (Ghiorso, 2004; Hofmeister, 1993), while the suitable treatment of temperature dependence has not been explored self consistently. Using theoretical relations for simple liquids as a starting point, I extend the finite strain free energy expansion to self consistently include temperature dependence. FPMD simulations provide a unique set of constraints with which to test this description, while also affording an account of the electronic free energy contribution. The resulting parameterization of silicate liquid thermodynamics is combined with a description of solids at high temperature to compute high pressure melting curves and Hugoniot loci for MgO periclase and $MgSiO_3$ perovskite, and make predictions of the changes in temperature, density and sound speed expected upon shock melting of these compounds.

To apply this thermodynamic description to liquids of arbitrary composition along the join, an appropriate model of mixing is required. The regular solution model, applied with the assumption of pressure independent enthalpy of mixing, works well over the limited range of composition and pressure considered in model parameterizations of experimental data (Ghiorso and Sack, 1995; Ghiorso et al., 2002; Lange and Carmichael, 1987; Stebbins et al., 1984; Lange, 1997; Ai and Lange, 2008), but the extent to which this assumption holds over larger ranges of composition and pressure needs to be rigorously explored. Notable contrasts exist in the response of structure and thermodynamics to compression found for MgO (Karki et al., 2006), Mg_2SiO_4 (Chapter II), $MgSiO_3$ (Stixrude and Karki, 2005) and SiO_2 (Karki et al., 2007). In Chapter IV, thermodynamic and structural properties are computed for four additional intermediate liquid compositions along the join (Mg_5SiO_7, $Mg_3S_2iO_7$, $MgSi_2O_5$ and $MgSi_3O_7$) and combined with existing results to explore the enthalpy and volume of mixing, as well as the underlying structural controls.

Chapter II is already published, while Chapters III and IV will be submitted for publication. Citations are as follows.

N. P. de Koker, L. Stixrude, and B. B. Karki. Thermodynamics, Structure, Dynamics, and Freezing of Mg_2SiO_4 Liquid at High Pressure. Geochimica et Cosmochimica Acta, 72:1427-1441, 2008a.

N. P. de Koker and L. Stixrude. Self-Consistent Thermodynamic Description of Silicate Liquids, with Application to Shock Melting of MgO Periclase and $MgSiO_3$ Perovskite. to be submitted to Geophysical Journal International, 2008b.

N. P. de Koker, L. Stixrude and B. B. Karki. Structure and Mixing of Liquids on the $MgO - SiO_2$ Join and the Origin of Liquid Immiscibility. to be submitted to Nature, 2008c.

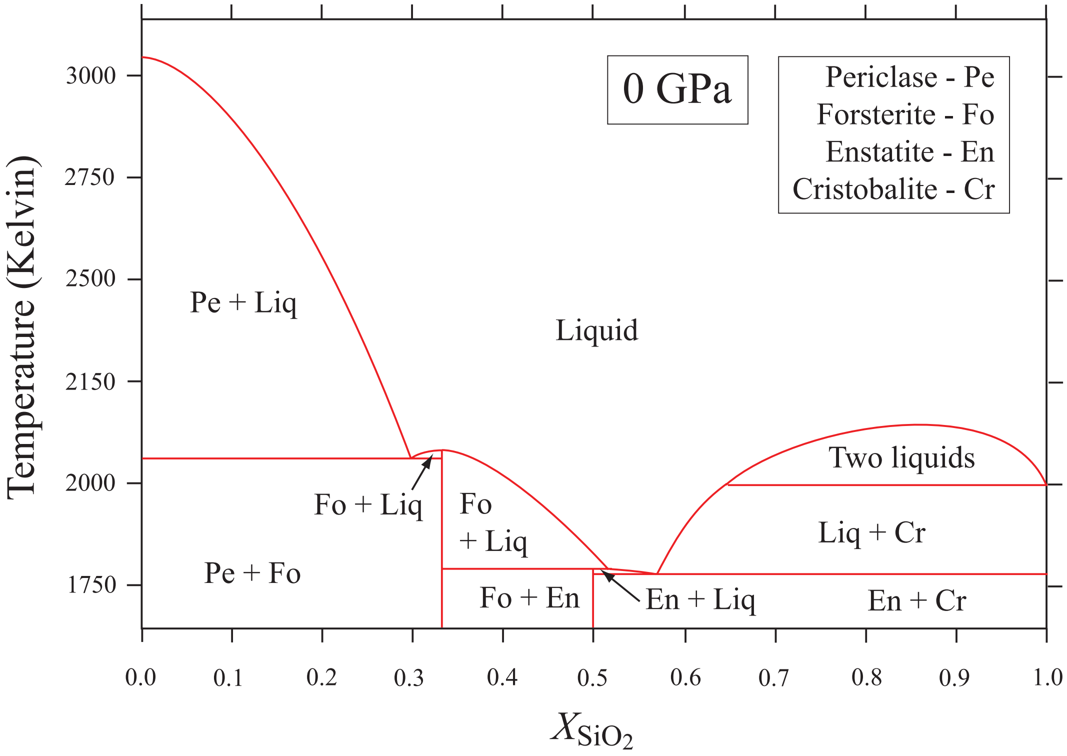

Figure 1.1: Ambient pressure phase diagram of the MgO-SiO_2 join. Note the liquid immiscibility field at high SiO_2 content and very refractory melting temperatures at the MgO end. Compiled from Bowen and Andersen (1914), Greig (1927), Ol'Shanskii (1951), Elliott et al. (1963), Riley (1966), Chen and Presnall (1975), Hageman and Oonk (1986).

CHAPTER II

Thermodynamics, Structure, Dynamics, and Freezing of Mg_2SiO_4 Liquid at High Pressure

2.1 Abstract

We perform first principles molecular dynamics simulations of Mg_2SiO_4 liquid and crystalline forsterite. On compression by a factor of two, we find that the Grüneisen parameter of the liquid increases linearly from 0.6 to 1.2. Comparison of liquid and forsterite equations of state reveals a temperature dependent density crossover at pressures of $\sim 12 - 17\,\mathrm{GPa}$. Along the melting curve, which we calculate by integration of the Clapeyron equation, the density crossover occurs within the forsterite stability field at $P = 13\,\mathrm{GPa}$ and $T = 2550\,\mathrm{K}$. The melting curve obtained from the root mean square atomic displacement in forsterite using the Lindemann law fails to match experimental or calculated melting curves. We attribute this failure to the liquid structure that differs significantly from that of forsterite, and which changes markedly upon compression, with increases in the degree of polymerization and coordination. The mean Si coordination increases linearly from 4 in the uncompressed system to 6 upon two-fold compression. The self-diffusion coefficients increase with temperature and decrease monotonically with pressure, and are well described by the Arrhenian relation. We compare our equation of state to the available high pressure shock wave data for forsterite and wadsleyite. Our theoretical liquid Hugoniot is con-

sistent with partial melting along the forsterite Hugoniot at pressures $150 - 170$ GPa, and complete melting at 170 GPa. The wadsleyite Hugoniot is likely sub-liquidus at the highest experimental pressure to date (200 GPa).

2.2 Introduction

The Earth's mantle is almost entirely solid, yet liquids play a disproportionately large role in our understanding of terrestrial chemical and thermal evolution. Silicates melt incongruently, and in the shallow mantle, the partial melt is readily separated from the residuum as a result of the large density contrast and low viscosity of the liquid. To accurately describe these processes, knowledge of the changes in liquid physical properties with pressure and temperature is needed, especially the density, Grüneisen parameter, chemical diffusivity and melting temperature. Furthermore, an understanding of liquid structure that ultimately governs these physical properties is key to predicting properties at conditions previously unexplored, and also offers deep insight into the physics of the liquid state.

Olivine and its polymorphs of dominantly Mg_2SiO_4 composition make up approximately 60 % of the upper mantle and transition zone. With increasing pressure, the eutectic composition on the $MgO - SiO_2$ join moves towards Mg_2SiO_4 (Ohtani and Kumazawa, 1981; Kato and Kumazawa, 1985; Presnall and Gasparik, 1990). The properties of Mg_2SiO_4 liquid are thus crucial to deep earth studies involving a liquid phase. These include magma ocean dynamics, lunar formation and mantle melting as the source for komatiitic and basaltic magmas. Buoyantly stable partial melt has been proposed to exist atop the 410 km discontinuity on the basis of seismic observations (Revenaugh and Sipkin, 1994; Song et al., 1994). In addition, the discovery of a ultra-low-velocity zone (ULVZ) at the core-mantle boundary (CMB) (Garnero and

Helmberger, 1995; Williams and Garnero, 1996) has lead to the speculation of the presence of partial melt in the bottom most part of the mantle. Indeed, estimates of the mantle geotherm in the lowermost mantle are similar to estimates of the lower mantle solidus (Holland and Ahrens, 1997; Luo et al., 2004; Stixrude and Karki, 2005).

The high melting temperature of forsterite ($2163 \pm 25\,\mathrm{K}$; Bowen and Andersen, 1914) has made accurate in situ experimental measurement of Mg_2SiO_4 liquid properties difficult. The volume at ambient pressure and its pressure and temperature derivatives are estimated from experimental measurements at lower temperature and more silica rich compositions, combined with the assumption of linear additivity of partial molar properties (Lange and Carmichael, 1987; Lange, 1997; Ai and Lange, 2008), or from fusion curve analysis and calorimetric data (Bottinga, 1985). The value of C_P measured for the supercooled liquid ($225\,\mathrm{J.mol^{-1}.K^{-1}}$; Tangeman et al., 2001) differs significantly from the model value calculated from partial molar heat capacities ($285 - 295\,\mathrm{J.mol^{-1}.K^{-1}}$; Stebbins et al., 1984; Lange and Navrotsky, 1992). Studies of non-crystalline structure have been limited to Mg_2SiO_4 glass (Cooney and Sharma, 1990; Kohara et al., 2004).

Here we apply first principles molecular dynamics to simulate Mg_2SiO_4 liquid and forsterite at pressures and temperatures relevant to the mantle. We investigate the equation of state, liquid structure and transport properties and compare with experiments and previous results based on semi-empirical inter atomic force models. By combining the liquid equation of state with that of forsterite, calculated using the same method, we integrate the Clapeyron equation to obtain the forsterite melting curve.

2.3 Computational Technique

The power and robustness of density functional theory (DFT) as a tool for determining the properties of earth materials at conditions relevant to planetary interiors have been extensively explored (Stixrude, 2001; Gillan et al., 2006). DFT was recently applied in combination with Born-Oppenheimer molecular dynamics to the simulation of silicate liquids over the entire mantle pressure-temperature regime (Stixrude and Karki, 2005; Karki et al., 2007).

DFT is based on the Hohenberg-Kohn theorem (Hohenberg and Kohn, 1964; Kohn and Sham, 1965), through which the wave function and total energy may be expressed as a unique functional of the ground state electron density. Although the theorem is exact, approximations are needed to account for the unknown exchange-correlation functional. In this study we adopt the most widely applied approximation, the local density approximation (LDA; Ceperley and Alder, 1980).

The influence of the core electronic wave functions of Mg, Si and O is approximated using ultrasoft pseudopotentials with core radii of 1.06 Å, 0.95 Åand 0.82 Å, and valence shells representing the $3s^2$, $3s^2 3p^2$ and $2s^2 2p^4$ electrons, respectively (Kresse and Hafner, 1994), as implemented in the VASP code (Kresse and Furthmüller, 1996). We perform molecular dynamics in the canonical ensemble (constant NVT), via a thermostat (Nosé, 1984). In order to make simulation with systems of sufficient size computationally feasible, the size of the plane-wave basis set is limited to a cutoff energy $E_{cut} = 400\,\mathrm{eV}$, for which we account by applying a finite basis set (Pulay) correction (Gomes Dacosta et al., 1986; Francis and Payne, 1990) to the calculated pressures (see below).

Simulations contain 112 atoms (16 formula units) with periodic boundary conditions (Figure 2.1). The initial condition is a $2 \times 1 \times 2$ supercell of forsterite homogeneously strained to a cubic cell shape and the desired volume. The Brillouin zone is sampled at the gamma point only. We simulate the liquid at volumes of $V/V_X = 1.2$, 1.1, 1.0, 0.9, 0.8, 0.7, 0.6 and 0.5 where $V_X = 52.36\,\mathrm{cm}^3/\mathrm{mol}$ is an estimate of the volume of Mg_2SiO_4 liquid at the ambient melting point (Lange and Carmichael, 1987). The initial configuration is melted at 6000 K, and then cooled isochorically to 3000 K and 4000 K. We also perform simulations of crystalline forsterite at 1000 K, 2000 K and 3000 K, and at volumes $V/V_X = 1.0$, 0.9, 0.8 and 0.7. We initiate crystalline simulations with the cell shape obtained by static structural relaxation at each volume, and then adjust cell parameters until the stress tensor is hydrostatic to within statistical uncertainty (Oganov et al., 2001b). The phase present in the simulation (crystal or liquid) is verified by inspection of the radial distribution function and the mean square displacement. Simulations of both liquid and solid are performed using a time step $\Delta t = 1\,\mathrm{fs}$, with each simulation running for at least 3000 time steps. The first 600 steps allow the system to converge, with equilibrium properties calculated over the remaining time. We estimate the uncertainty in the energy (E) and pressure (P) by applying the blocking method (Flyvberg and Petersen, 1989). Tests of convergence with respect to system size (70 and 336 atom supercells), run duration (6 ps), initial configuration (strained ringwoodite) and k-point sampling ($2 \times 2 \times 2$ Monkhorst and Pack (1976) grid) show that variations are well within the mean statistical uncertainty of the simulations ($\sigma_E = 8.8\,\mathrm{kJ/mol}$; $\sigma_P = 1.5\,\mathrm{GPa}$). Slow cooling over 3000 fs from 6000 K to 3000 K showed no cooling rate dependence of the thermodynamic or structural properties.

Two corrections are applied to the pressures calculated in the simulations as follows

$$P(V) = P_{MD}(V) + P_{Pulay}(V) + P_{emp}(V). \tag{2.1}$$

We compute the Pulay correction as

$$P_{Pulay}(V) = P_S(V; E_{cut} = 600\,\mathrm{eV}) - P_S(V; E_{cut} = 400\,\mathrm{eV}), \tag{2.2}$$

where P_S is the static pressure of the fully relaxed structure of forsterite computed with a $2 \times 2 \times 2$ Monkhorst Pack k-point mesh, and 600 eV as has been found in previous studies to yield fully converged results (Karki et al., 2001). We find that P_{Pulay} increases monotonically from 2.6 GPa at $V/V_X = 1.0$ to 5.1 GPa at $V/V_X = 0.5$. Values calculated for different atomic configurations obtained from the simulations, as well as for wadsleyite and ringwoodite, differ from the forsterite value by less than 0.2 GPa. The empirical correction accounts for the well known and systematic over-binding of LDA (Karki et al., 2001; Oganov et al., 2001a) and is computed as

$$P_{emp} = -P_S(V_{exp}; E_{cut} = 600\,\mathrm{eV}), \tag{2.3}$$

where V_{exp} is the experimental zero-pressure volume of forsterite at static conditions computed via the thermodynamic model of Stixrude and Lithgow-Bertelloni (2005). For forsterite we find $P_{emp} = 1.6$ GPa. Values calculated for wadsleyite and ringwoodite are 1.4 GPa and 1.7 GPa, respectively.

We fit the simulation pressure and internal energy results to the Mie-Grüneisen equation of state,

$$P(V,T) = P_C(V,T_0) + \frac{\gamma(V)C_V(V)}{V}\left[T - T_0\right], \tag{2.4}$$

$$E(V,T) = E_0 + E_C(V,T_0) + C_V(V)\left[T - T_0\right], \tag{2.5}$$

$$P_C(V,T_0) = 3K_0 f\,(1+2f)^{5/2}\Big[1 + a_1 f + \cdots\Big], \tag{2.6}$$

$$E_C(V,T_0) = T_0\int_{V_0}^{V}\frac{\gamma(V')C_V(V')}{V'}dV' + 9K_0V_0f^2\Big[\frac{1}{2} + \frac{a_1}{3}f + \cdots\Big], \tag{2.7}$$

$$a_1 = \frac{3}{2}\Big[K_0' - 4\Big], \tag{2.8}$$

$$f = \frac{1}{2}\Big[\left(\frac{V_0}{V}\right)^{2/3} - 1\Big], \tag{2.9}$$

where the expression for the internal energy follows from the Eulerian finite strain expansion of the Helmholtz free energy, F, (Birch, 1952; Stixrude and Bukowinski, 1990a), the Euler relation, $E = F + TS$, and the Maxwell identity $(\partial S/\partial V)_T = (\partial P/\partial T)_V$. E_0, V_0, K_0 and K_0' are respectively the internal energy, volume, isothermal bulk modulus (K_T) and its first pressure derivative at zero pressure and temperature T_0. The isochoric heat capacity (C_V) and Grüneisen parameter (γ), are determined from our simulations as the dependence of internal energy and pressure on temperature at constant volume, and are found to be linear to within our resolution:

$$C_V = \left(\frac{\partial E}{\partial T}\right)_V, \tag{2.10}$$

$$\frac{\gamma}{V} = \left(\frac{\partial P}{\partial E}\right)_V. \tag{2.11}$$

The volume dependence of C_V and γ are described accurately as

$$C_V(V) = C_V(V_X) + C_V'\Big[\frac{V}{V_X} - 1\Big] + \cdots, \tag{2.12}$$

$$\gamma(V) = \gamma(V_X) + \gamma' \left[\frac{V}{V_X} - 1 \right] + \cdots . \tag{2.13}$$

We estimate the uncertainty in a thermodynamic quantity at a given volume and temperature by repeated fitting of the equation of state to a Monte-Carlo sampling of the simulation data within its error estimates (values converge after about 10^4 iterations).

The melting curve is computed via the Clausius-Clapeyron relation

$$\frac{\partial T_M}{\partial P} = \frac{\Delta V}{\Delta H / T_M}, \tag{2.14}$$

where the volume and enthalpy differences are taken from our simulations, and the integration constant is set to the experimental melting point at ambient conditions ($2163 \pm 25\,\mathrm{K}$; Bowen and Andersen, 1914). This hybrid approach, in which we take only the initial melting temperature from experiment, and compute the melting temperature at all other pressures from our simulations is much more efficient than the fully first principles determination of melting temperatures (Sugino and Car, 1995; Alfe, 2005). Moreover, our approach is justified by the good agreement with experimental melting temperatures found in extremely demanding fully first principles computations of melting, which have not yet been attempted on systems as complex as forsterite. In order to compute the melting curve, we compare the properties of the liquid and the solid at constant pressure. This is accomplished via interpolation, and the error in the volume is estimated from that in the pressure as

$$\sigma_V = \left(\frac{\partial V}{\partial P} \right)_T \sigma_P . \tag{2.15}$$

Our forsterite simulations allow the determination of the mean square displacement of all the atoms ($\langle u_{rms} \rangle$) as a function of pressure and temperature. Together with the mean inter-atomic distance (a), the Lindemann law melting curve can be calculated in its original formulation (Lindemann, 1910)

$$f_c = \frac{\langle u_{rms} \rangle}{a}, \tag{2.16}$$

by determining the value of the constant critical fraction (f_c) at the experimental ambient melting point (Gilvarry, 1956).

We calculate the theoretical Hugoniot pressure (P_H), temperature (T_H) and internal energy (E_H) at a given volume (V_H) by iteratively solving equations 4 and 5 to satisfy the Rankine-Hugoniot relation,

$$(E_H - E_R) = -\frac{1}{2}\left(P_H + P_R\right)\left(V_H - V_R\right), \tag{2.17}$$

where E_R and V_R is the internal energy and volume of the unshocked sample at reference pressure P_R and temperature T_R.

The self-diffusion coefficient D_N for the N-particle periodic system is computed via

$$D_N = \lim_{t \to \infty} \frac{\langle [r(t)]^2 \rangle}{6t}, \tag{2.18}$$

where is the mean square displacement. The pressure and temperature dependence of is described by the Arrhenius relation,

$$D_N(P,T) = D_N^0 \exp\left[-\frac{E_a + PV_a}{RT}\right], \tag{2.19}$$

where E_a and V_a are the activation energy and volume. We account for finite size effects in the periodic system by applying a correction based on the Kirkwood-Riseman theory of polymer diffusion (Yeh and Hummer, 2004; Zhang et al., 2004). The diffusivity for an infinitely large system is calculated as

$$D_\infty = D_N + \frac{k_B T \xi}{6\pi\eta L}, \tag{2.20}$$

where D_N is the diffusivity from the N-particle simulation, ξ is a constant ($\approx$ 2.837297), L is the size of the box and η is the viscosity of the liquid. The viscosity is estimated by the Eyring relation

$$\eta = \frac{k_B T}{D_\infty \lambda}, \tag{2.21}$$

where λ was found by Lacks et al. (2007) to have a value of $16\,R_\mathrm{O}$ for $\mathrm{Mg_2SiO_4}$ liquid, $R_\mathrm{O} = 1.4\,\text{Å}$ being a canonical value for the ionic radius of oxygen.

2.4 Results

2.4.1 Equation of State

We find the third order expansion in f (equations 2.4 and 2.5) to be sufficient to represent the equation of state results (Figure 2.2), with the isochoric heat capacity (C_V) and Grüneisen parameter (γ) as linear functions of volume (equations 2.12-2.13; Figure 2.3). Values of the parameters in equations 2.4-2.13 for liquid and forsterite are reported in Table 2.1. Tables 2.2 and 2.3 compare theoretical and experimental values for liquid and solid, respectively.

Our computed values of the physical properties of the liquid at the ambient melting point are consistent with previous experimental data (Stebbins et al., 1984; Bottinga, 1985; Lange and Carmichael, 1987; Rivers and Carmichael, 1987; Rigden et al., 1989; Lange, 1997; Tangeman et al., 2001; Ai and Lange, 2008). Agreement with the volume, thermal expansivity and bulk modulus is excellent. The computed value of K_0' is much larger than a previous estimate based on fusion curve analysis, and more similar to values found for other silicate liquids by direct measurement of the equation of state (Rigden et al., 1989). Our value of the heat capacity lies between two previous experimental estimates. Our value of V_0 is very similar to that ($57.9\,\mathrm{cm^3/mol}$) found by Lacks et al. (2007) using empirical potentials. However, with compression their computed pressure deviates systematically and increasingly from our predictions, being 1.4 GPa less at the smallest volume of their study (33.5 cm^3/mol) and 3000 K.

We find that liquid state isotherms diverge upon compression: the thermal pressure coefficient $B = (\partial P/\partial T)_V = \gamma C_V/V$ increases as the volume decreases. The isochoric heat capacity decreases from 4.4 $\mathrm{Nk_B}$ at $V/V_X = 1.0$ to 3.7 $\mathrm{Nk_B}$ at $V/V_X = 0.5$, and the Grüneisen parameter of the liquid increases from 0.6 to 1.2 over the same range of compression (Figure 2.3), in contrast to the behavior of crystalline forsterite for which C_V remains essentially constant at a value of about 3.1 $\mathrm{Nk_B}$ and the Grüneisen parameter decreases on compression. Along the 3000 K isotherm, the enthalpy difference between liquid and solid decreases steadily, while the difference in volume reveals a density crossover at 16 ± 3 GPa (Figure 2.2, inset). The pressure of the density crossover decreases with decreasing temperature.

2.4.2 Melting Curve

We find that the melting temperature reaches a maximum of $T = 2550$ K at $P = 13$ GPa, well within the forsterite stability field (Akaogi et al., 1989), and has a negative slope at higher pressures as a result of a density crossover (Figure 2.4). The entropy and volume of fusion at ambient conditions ($\Delta H/T_M = 0.95 \pm 0.04\,\mathrm{Nk_B}$, $\Delta V = 5.7 \pm 0.1\,\mathrm{cm}^3$/mol) agree with experimental estimates ($\Delta H/T_M = 0.91 \pm 0.16\,\mathrm{Nk_B}$ (Navrotsky et al., 1989; Lange and Carmichael, 1987; Lange, 1997)). The entropy of fusion ($\Delta H/T_M$) along the melting curve decreases to 0.75 $\mathrm{Nk_B}$ at 20 GPa, significantly lower than the entropy of melting of $\mathrm{MgSiO_3}$ perovskite ($\sim 1.5\,\mathrm{Nk_B}$) found in a previous simulation study (Stixrude and Karki, 2005).

Experimentally determined melting curves of forsterite disagree with one another above 10 GPa (Davis and England, 1964; Ohtani and Kumazawa, 1981; Presnall and

Walter, 1993). At high pressures, our melting curve is in excellent agreement with the measurements of Presnall and Walter (1993), while at lower pressures it is slightly higher than the experimental measurements of both Davis and England (1964) and Ohtani and Kumazawa (1981).

Experimental evidence shows that, towards the high pressure end of the forsterite stability field, forsterite melts incongruently to a more silica rich liquid (Ohtani and Kumazawa, 1981; Kato and Kumazawa, 1985; Presnall and Gasparik, 1990) and either anhydrous B or periclase. Figure 2.5 illustrates that a more silica rich liquid is denser than both forsterite and Mg_2SiO_4 liquid, though less dense than crystalline anhydrous B and periclase (Karki et al., 2000a). Therefore partial melting of forsterite at high pressure produces a liquid denser than crystalline forsterite. The liquidus phases on Mg_2SiO_4 composition at the base of the upper mantle (periclase and anhydrous B) are denser than the liquid.

The mean $\langle u_{rms} \rangle$ in forsterite varies between $0.05\,\text{Å}^2$ at $1000\,\text{K}$ and $0.3\,\text{Å}^2$ at $3000\,\text{K}$, with a weak volume dependence of about $0.0065\,\text{Å}^2.\text{mol.cm}^{-3}$. Our Lindemann melting curve computed from interpolated values of $\langle u_{rms} \rangle$ (Figure 2.4), shows poor agreement with experimental data and fails to capture the slope as well as its change with pressure (curvature) seen in both our FPMD results as well as the experimental data (Presnall and Walter, 1993).

2.4.3 $\mathbf{Mg_2SiO_4}$ Hugoniot

We compare our theoretical Hugoniot for Mg_2SiO_4 liquid, together with Hugoniots for a partially molten sample of periclase + $MgSiO_3$ liquid (Stixrude and Karki, 2005), and solid phase assemblages perovskite + periclase (Pv+Pe), post-perovskite + periclase (PPv+Pe) and stishovite + periclase (St+Pe) (Stixrude and Lithgow-Bertelloni, 2005), to the published high pressure shock data for forsterite and wadsleyite (Jackson and Ahrens, 1979; Watt and Ahrens, 1983; Brown et al., 1987a,b; Luo et al., 2004; Mosenfelder et al., 2007) (Figure 2.6).

Pressure-density and temperature measurements on the forsterite Hugoniot agree well with our computed Hugoniots of the sub-solidus assemblage (PPv+Pe) at pressures below 150 GPa, a mixture of periclase and $MgSiO_3$ liquid between $150-170$ GPa, and with pure Mg_2SiO_4 liquid at higher pressures. We find that the pressure-volume relation on the wadsleyite Hugoniot (there are no temperature measurements) is consistent with the sub-solidus assemblage at 140 GPa, and pure liquid or a mixture of periclase and Mg_2SiO_4 liquid at 200 GPa. Shot #349 on wadsleyite is not consistent with any of our computed Hugoniots. The discrepancy with Mg_2SiO_4 liquid for wadsleyite shot #349 (almost 50 GPa) is much larger than the uncertainty in the simulated pressure (1.4 GPa), which includes the uncertainty estimates for P_{Pulay} and P_{emp} (equation 2.1).

2.4.4 Liquid Structure

We define the bond length as the mode of the first peak in the partial radial distribution function (RDF) (McQuarrie, 1984). Upon compression, the Si-O bond length increases initially from a value of 1.63 Å (Figure 2.7) to 1.64 Å at $V/V_X = 0.7$ and then decreases to 1.62 Å at 3000 K and the highest compression considered. Over the same compression interval the Mg-O bond length decreases from 1.97 Å to 1.83 Å. The mode and median of the first peak diverge, as the radial distribution function broadens with increasing distortion of the polyhedra on compression. Si-O and Mg-O bond lengths and coordination numbers at low pressure compare very well with experimental data (Kohara et al., 2004) on the structure of Mg_2SiO_4 glasses (Table 2.4).

The coordination number ($Z_{\alpha\beta}$) is computed as the integral of the radial distribution function

$$Z_{\alpha\beta} = 4\pi\rho \int_0^{r_{cut}} g_{\alpha\beta}(r) r^2 dr, \tag{2.22}$$

where ρ is the density and r_{cut} is the position of the first minimum in $g_{\alpha\beta}$. $Z_{\text{Si}-\text{O}}$ increases from 4.1 to 6.0, while $Z_{\text{Mg}-\text{O}}$ increases from 5.1 to 7.7 (Figure 2.7) on two-fold compression. The smooth and nearly linear increase on compression is facilitated by gradual changes in the abundances of the various coordination species, of which a mixture is present at all conditions studied (Figure 2.8). The variety of local coordination environments may also be characterized by the O-Si coordination number ($Z_{\text{O}-\text{Si}}$), which shows relative abundances changing upon compression (Figure 2.9). At low pressure, the liquid has $\sim 15\,\%$ (or 0.6 O per Si) bridging oxygens (O_B ; $Z_{\text{O}-\text{Si}} = 2$) and $\sim 70\,\%$ (2.8 O per Si) non-bridging oxygens (O_N ; $Z_{\text{O}-\text{Si}} = 1$). The remaining 15 % of O atoms are not bound to Si (O_F ; $Z_{\text{O}-\text{Si}} = 0$), and are hence referred to as 'free oxygens' (Hess, 1980) (red spheres in Figure 2.1). Changes in the concentrations of the various O and Si coordination species with pressure are associated with increased polymerization and Si coordination.

Analysis of atomic trajectories reveals that coordination increases through the following two reactions:

$$\text{O}_N +_{[Z]} \text{Si}^{\text{O}_B} \leftrightarrow_{[Z+1]} \text{Si}^{\text{O}_{B+1}}, \tag{2.23}$$

$$\text{O}_F +_{[Z]} \text{Si}^{\text{O}_B} \leftrightarrow_{[Z+1]} \text{Si}^{\text{O}_B}. \tag{2.24}$$

We describe the local structure about Si atoms as ${}_{[Z]}\text{Si}^{\text{O}_B}$, with $[Z]$ the coordination number and O_B the number of bridging oxygens. Our notation is a generalization of the commonly used Q^{O_B} notation, which specifies the number of bridging oxygens in systems for which $Z = 4$. Reactions 2.23 and 2.24 are illustrated by the increase in the proportion of bridging oxygens as the proportion of free oxygens decreases on compression (Figure 2.9). Bridging oxygens are almost never added to the coordination shell of another silicon and therefore do not contribute significantly to the coordination increase, consistent with Raman, infrared, and nuclear magnetic resonance spectroscopic observations in alkali-silicate glasses (Wolf et al., 1990; Xue et al., 1991) showing coordination increases primarily at the expense of non-bridging oxygens. Examples of reactions 2.23 and 2.24 are illustrated in Figure 2.10 in which ${}_{[4]}\mathrm{Si}^1$ is shown transforming into ${}_{[4]}\mathrm{Si}^0$ (top panel), and ${}_{[4]}\mathrm{Si}^3$ to ${}_{[3]}\mathrm{Si}^2$ and then to ${}_{[5]}\mathrm{Si}^4$(bottom panel).

2.4.5 Transport Properties

Characteristic bond lifetimes calculated from the bond breaking rate (Kubicki and Lasaga, 1991) reveal a strong decrease in the average Si-O bond lifetime from 2000 fs at ambient pressure and 3000 K to 500 fs at high pressure. Mg-O bond lifetimes increase only slightly over the same pressure range from 300 fs to 400 fs. Over the same compression range, the long lifetimes of O_F and O_N at low pressure (~ 1500 fs at 3000 K) decrease to values similar to that of O_B (500 fs at 3000 K) which remain essentially unchanged as a function of volume.

Self-diffusion coefficients increase with temperature and decrease with pressure (Figure 2.12), and do not show the initial increase with increasing pressure seen in more highly polymerized silicate liquids (Angell et al., 1982; Karki et al., 2007): The pressure and temperature dependence is well described by the Arrhenius relation. Fit parameters for Mg, Si, O and total self-diffusion (Table 2.5) are found to be independent of temperature over the range investigated.

By comparing with longer runs, we find 2400 ergodic timesteps to be sufficient to determine robust values of the self-diffusion coefficient values from the mean square displacement $\langle [r(t)]^2 \rangle$ (Figure 2.11), for all simulations except the $V/V_X = 0.5$; $T = 4000\,\mathrm{K}$ and $V/V_X = 0.6$; $T = 3000\,\mathrm{K}$ points, for which 5000 timesteps are sufficient. The $V/V_X = 0.5$; $T = 3000\,\mathrm{K}$ point is not included in the analysis of thermodynamic and transport properties, because we find it to be a glass: $\langle [r(t)]^2 \rangle$ flattens out at $0.25\,\text{Å}^2$, similar to values found in the solid at low pressure, though somewhat higher than solid values extrapolated to $V/V_X = 0.5$ ($0.17\,\text{Å}^2$).

Equation 2.20 implies a $N^{-1/3}$ dependence of diffusivity on system size. The corrected total diffusivity at $V/V_X = 1.0$; $T = 3000\,\mathrm{K}$, ($D_\infty = 6.13 \pm 0.6 \times 10^{-9}\,\mathrm{m}^2/\mathrm{s}$) calculated with equation 2.20 is similar to the value ($D_\infty = 6.7 \pm 0.7 \times 10^{-9}\,\mathrm{m}^2/\mathrm{s}$) we find from the linear relation

$$D_N = D_\infty + aN^{-1/3}, \tag{2.25}$$

fit to our results for 112 and 336 atoms.

2.5 Discussion

The structure of Mg_2SiO_4 liquid differs markedly from that of crystalline forsterite. Whereas in forsterite all O are bonded to Si, with SiO_4 tetrahedra isolated from one another (entirely Q^0 or $_{[4]}\mathrm{Si}^0$ in our notation), in the liquid free oxygens and tetrahedral linkages ($Q^{\geq 1}$ or $_{[4]}\mathrm{Si}^0$) appear. Free oxygens are also present in the high pressure crystalline polymorph wadsleyite, in which all tetrahedra exist as dimers (Si_2O_7). The difference in structure between Mg_2SiO_4 liquid and forsterite is important as it accounts for the very large enthalpy of vitrification of Mg_2SiO_4 (Kohara et al., 2004) and the failure of the Lindemann law in this system. Evidence of dimers in amorphous Mg_2SiO_4 had previously been obtained only for the glass, via vibrational spectroscopy, nuclear magnetic resonance, and x-ray diffraction (McMillan, 1984; Williams et al., 1989; Cooney and Sharma, 1990; Williams, 1990; Kohara et al., 2004). While experimental studies have found evidence only for Q^0 and Q^1 species, we also find a substantial number of Q^2 and Q^3. We find that the abundance of Q^2 and Q^3 species decreases with decreasing temperature so that they may not be detectable in the glass. The liquid also differs from the structure of crystalline phases in having $Z_{\mathrm{Mg-O}} = 5.1$, substantially less than that in the tetrahedrally coordinated crystalline polymorphs ($Z_{\mathrm{Mg-O}} = 6$), which accounts for the volume of melting.

The structure of the liquid remains distinct from that of crystalline phases at elevated pressure. The Si-O (and Mg-O) coordination number of the liquid increases monotonically with compression over the entire range studied, in sharp contrast to that of the crystalline phases in which the coordination number remains $Z_{\mathrm{Si-O}} = 4$ up to the transformation of ringwoodite to perovskite + periclase near 24 GPa, where it increases to $Z_{\mathrm{Si-O}} = 6$. Liquid structure is also distinct in that it shows an initial increase in Si-O bond length on compression, which we attribute to the increase in coordination number.

We suggest an alternative interpretation of the dynamic compression of forsterite that is consistent with our computed Hugoniots, the shock temperature measurements of Luo et al. (2004) and the pressure-volume data of Mosenfelder et al. (2007) except the wadsleyite portion of shot #349. Dynamic loading of forsterite produces incongruent melting to periclase and a more silica-rich liquid at $150 - 170\,\mathrm{GPa}$. At higher pressures, pure Mg_2SiO_4 liquid is present on the forsterite Hugoniot, while at lower pressures, sub-solidus assemblages (PPv+Pe) are present on the Hugoniot.

This picture has important implications for the interpretation of the wadsleyite Hugoniot (Mosenfelder et al., 2007) and of sound speed data (Brown et al., 1987a,b). We find the wadsleyite Hugoniot to be $1000 - 1400\,\mathrm{K}$ colder than that of forsterite at $150 - 200\,\mathrm{GPa}$. It is therefore likely that even the highest pressure wadsleyite point of

Mosenfelder et al. (2007) (shot #350) is either sub-solidus or only partially molten. We therefore suggest that determination of a liquid phase value of the Grüneisen parameter based on this datum should be treated with caution. While Mosenfelder et al. (2007) find that the Grüneisen parameter increases on compression in the liquid, in general agreement with the trend that we find, their value (2.6) is much higher than our predictions. This discrepancy is explained if the measured portion of the wadsleyite Hugoniot is less than completely molten. Our interpretation cannot account for shot #349 on wadsleyite of Mosenfelder et al. (2007) which lies at much lower pressures than all our computed Hugoniots. Sound speed measurements have been interpreted to indicate melting on the forsterite Hugoniot above 150 GPa. The measured value of the sound speed at 168 GPa (10.8 km.s^{-1}) is considerably less than what we find at the same pressure: 11.5 km.s^{-1} varying little with temperature from 3000 to 6000 K. The smaller experimental value may be due to incongruent melting: a solid-liquid mixture with proportions varying as the shock front passes. Because the experimental sample may be only partially molten, the value of the Grüneisen parameter determined (2.1), which is substantially higher than our predicted value, may not be representative of the liquid state. Indeed, at higher pressures (195 GPa) the experimental sound velocity (12.2 km.s^{-1} (Brown et al., 1987a)) agrees well with extrapolation of our results (12.4 ± 0.2 km.s^{-1}), consistent with complete melting in the shocked sample.

The behavior of the Grüneisen parameter that we calculate in the liquid - increasing on compression - is contrary to that of all mantle crystalline phases, for which the Grüneisen parameter decreases with compression (Figure 2.3). This behavior was first recognized in silicate liquids by Stixrude and Karki (2005), and has also been found in studies of non-silicate liquids (Davis and Gordon, 1967; Knopoff and Shapiro, 1970; Boehler and Kennedy, 1977; Vočadlo et al., 2003; Karki et al., 2006). The increase of the Grüneisen parameter on compression in the liquid can be understood as follows. While γ decreases with compression in crystalline phases, it increases across pressure induced phase transitions associated with an increase in Si coordination (Jeanloz and Roufosse, 1982) (Figure 2.3). Since the coordination number increases gradually and continuously in the liquid, we expect the Grüneisen parameter also to increase on compression as it adopts values characteristic of higher coordinated states.

Increasing coordination is further expressed as a density crossover, providing fundamental insight into the contrasting behavior of complex liquids and solids upon compression. Our results reveal the origin of olivine floatation in compositions thought to be representative of an initial magma ocean (Stolper et al., 1981; Agee and Walker, 1988; Ohtani, 1988; Trønnes and Frost, 2002). The density crossover originates primarily in the structure of the liquid and occurs, even in forsterite composition, at 13 GPa along the solidus, where the Si-O coordination number of the liquid is 4.4, greater than that in the crystal. In natural compositions the density of the liquid will be further enhanced relative to that of coexisting solids by the incompatibility of abundant heavy elements, such as Fe and Ca. The isochemical density crossover that we find supports the notion that buoyantly stable silicate melt may exist at the base of the olivine stability field in the mantle at 410 km depth (Revenaugh and Sipkin, 1994).

The discrepancy between our melting curve and experimental data at low pressures may be related to uncertainty in the ambient melting point of forsterite. To illustrate, also shown in Figure 2.4 is an alternative melting curve obtained by using $T_{M_0} = 2140\,\mathrm{K}$, which represents the lower bound of the quoted uncertainty for the ambient melting temperature determined by Bowen and Andersen (1914). Integration of the Clausius-Clapeyron equation (2.14) based on our results and this value of T_{M_0} improves agreement with the data of Davis and England (1964), while maintaining agreement at high pressure with the data of Presnall and Walter (1993).

The failure of the Lindemann law to capture the change in slope of the melting curve with pressure is not surprising, since it assumes that the structure of the liquid remains constant along the melting curve (Ross, 1969). The changes in liquid structure that we find reduce the volume of the liquid relative to the Lindemann picture, causing the melting slope to decrease rapidly with pressure. We thus reinforce the overall conclusion of Wolf and Jeanloz (1984) that the Lindemann criterion should not be used to extrapolate melting temperatures of mantle phases, although those authors found good agreement in the case of forsterite between the Lindemann law and the data of Ohtani and Kumazawa (1981), in notable contrast to other minerals considered in their study, and with our findings.

The short lifetime of the Mg-O bond relative to that of the Si-O bond is consistent with the smaller activation energy and higher self-diffusion coefficients found for Mg compared to Si (Table 2.5). While our activation energy values are similar to those obtained by Kubicki and Lasaga (1991), our finite size-corrected self-diffusion coefficients are much larger. Conversely, our low pressure self-diffusion coefficients are similar to results of Lacks et al. (2007), but the pressure dependence of their results implies a higher activation volume (Figure 2.12). These previous simulations are based on semi-empirical interatomic potentials, and differences likely reflect uncertainties related to the construction of inter atomic force models in the earlier studies, emphasizing the importance of our parameter free first principles simulations. No experimental values of self-diffusion in forsterite liquid exist; data that have been obtained are on more silica rich compositions. For example, the experimental value of the activation energy for diffusion of silicon and oxygen in $CaMgSi_2O_6$ melt (Kubicki et al., 1990; Reid et al., 2001), is much greater than our value for forsterite. This difference may reflect the difference in silica content, and therefore fragility (Angell, 1995) of forsterite versus diopside composition melts, as well as the lower temperature range over which the experimental value is obtained.

2.6 Conclusions

Our First Principles Molecular Dynamics calculations for Mg_2SiO_4 liquid show the Grüneisen parameter and thermal pressure coefficient increasing upon compression. Comparison of the liquid equation of state to that we calculate for forsterite shows the presence of a density crossover at pressures of $12 - 17\,\mathrm{GPa}$ and temperatures of $2000 - 3500\,\mathrm{K}$. Along the melting curve we determine by integration of the Clausius-Clapeyron equation, the density crossover is found at 13 GPa, within the stability field of forsterite. Comparison of our melting curve to an extrapolation of the ambient melting temperature through the Lindemann law indicates that such extrapolations for silicates cannot yield accurate results, due to significant differences in structure between the liquid and the solid, and significant changes in liquid structure on compression, primarily expressed as a continuous increase in coordination and polymerization. Comparison of the liquid equation of state to the available high pressure shock wave data is consistent with partial melting along the forsterite Hugoniot at pressures above 150 GPa, and complete melting at pressures above 170 GPa; and sub-liquidus conditions on the wadsleyite Hugoniot up to the highest pressures measured to date (200 GPa). Liquid diffusivities increase with temperature and decrease monotonically with pressure, and are found to be well described by the Arrhenian relation.

2.7 Acknowledgements

This research was supported by the National Science Foundation under Grants EAR-0409074 and EAR-0409121. Computing facilities were provided by CCT at Louisiana State University.

Table 2.1: Equation of state fit parameters for equations 2.4-2.13.

	Mg_2SiO_4	Forsterite
T_0 (Kelvin)	3000	1000
V_0 (cm^3/mol)	57.8 (3)	44.8 (2)
K_{T0} (GPa)	19 (3)	101 (7)
K'_{T0}	6.2 (5)	5.4 (7)
$C_V(V_X)$ (Nk_B)	4.29 (3)	3.10 (2)
C'_V	0.68 (16)	0.05 (8)
$\gamma(V_X)$	0.64 (6)	1.4 (2)
γ'	-1.2 (2)	1.8 (1.2)

Table 2.2: Comparison of liquid equation of state to experimental data at 2163 K, 0 GPa.

	This study	Experiment
V (cm^3/mol)	53.55	53.5 (2)[a]
K_T (GPa)	23 (8)	24.3 (1)[b], 59[c]
K'_T	7 (1)	3.75[c], 6.9[d,†]
$\alpha\, 10^{-6}\mathrm{K}^{-1}$	121 (50)	122 (7)[a]
C_V (Nk$_\mathrm{B}$)	4.4 (5)	3.7 (4)[a,e,‡], 4.9 (3)[a,f]
γ	0.6 (1)	0.22 (4)[a,f], 0.56 (3)[a,b,f], 0.74 (4)[a,b,e]

[a] Lange (1997), [b] Ai and Lange (2008), [c] Bottinga (1985), [d] Rigden et al. (1989), [e] Tangeman et al. (2001), [f] Stebbins et al. (1984)

[†] K'_T for $\mathrm{CaMgSi_2O_6}$ liquid

[‡] Supercooled liquid at $1040 - 1773$ K

Table 2.3: Comparison of crystalline equation of state with experimental values computed from the model of Stixrude and Karki (2005) at 1000 K, 0 GPa.

	This study	Experiment
V_0 (cm^3/mol)	44.8 (2)	44.5
K_0 (GPa)	101 (7)	113.4 (2)
K_0'	5.4 (7)	4.6 (2)
$\alpha\, 10^{-6}\mathrm{K}^{-1}$	44 (10)	35 (1)
C_V (Nk$_\mathrm{B}$)	3.10 (3)	2.92 (3)
γ	1.1 (3)	1.0 (3)

Table 2.4: Comparison of simulated liquid structure to experimental data (Kohara et al., 2004).

	This study $V/V_X = 1.0$; $T = 1000\,\mathrm{K}$	Experiment $P = 0\,\mathrm{GPa}$; $T = 300\,\mathrm{K}$ glass
$d_{\mathrm{Si-O}}$	$1.63\,\mathrm{\AA}$	$1.63\,\mathrm{\AA}$
$d_{\mathrm{Mg-O}}$	$1.97\,\mathrm{\AA}$	$2.00\,\mathrm{\AA}$
$Z_{\mathrm{Si-O}}$	4.1	4.1
$Z_{\mathrm{Mg-O}}$	5.1	5.0
${}_{[4]}\mathrm{Si}^0$	22 %	~ 50 %
${}_{[4]}\mathrm{Si}^1$	38 %	~ 50 %
${}_{[4]}\mathrm{Si}^2$	21 %	–
${}_{[4]}\mathrm{Si}^3$	10 %	–

Table 2.5: Self-diffusion coefficient Arrhenius relation fit parameters (equation 2.19).

	D^0_∞ (10^{-9} m^2/s)	D^0_N (10^{-9} m^2/s)	E_a (kJ/mol)	V_a (cm^3/mol)
Total	485 (70)	339 (49)	106 (5)	0.88 (7)
Si	476 (108)	332 (76)	124 (8)	0.76 (9)
Mg	359 (69)	251 (48)	87 (6)	1.00 (7)
O	560 (85)	391 (59)	113 (6)	0.87 (8)

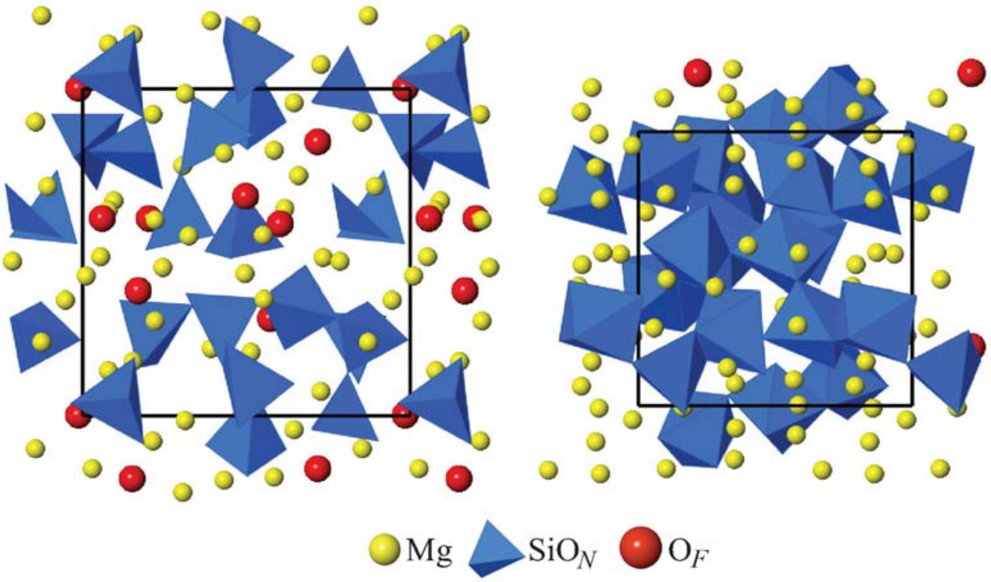

Figure 2.1: Snapshots of the simulated liquid at 3000 K, for $V/V_X = 1.0$ and $V/V_X = 0.5$. The uncompressed structure is very open, with Si almost entirely four-fold coordinated. Tetrahedra are mostly free-floating, with dimers and a four-membered chain also visible. The compressed structure is more densely packed, with Si mostly six-fold coordinated. Polyhedra are highly polymerized, some sharing edges. Free oxygen atoms (red spheres) are less abundant at higher pressures.

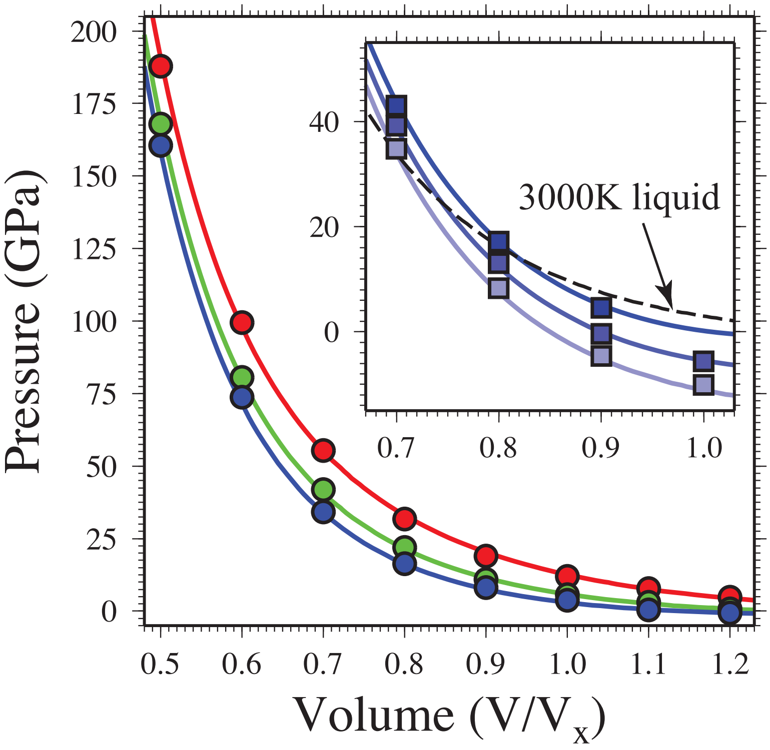

Figure 2.2: Equation of state of liquid Mg_2SiO_4. FPMD results are shown by the blue (3000 K), green (4000 K) and red (6000 K) circles, with the Mie-Grüneisen equation fit to these results shown by the colored lines. Note that the $V/V_X = 0.5$; 3000 K point is a glass and not included in the fit. A thermal pressure coefficient that increases on compression results in isotherms diverging upon compression. (inset) FPMD equation of state of forsterite at 1000 K, 2000 K and 3000 K, results shown by squares, Mie-Grüneisen fit by solid blue lines. The broken line is the 3000 K liquid isotherm, which crosses the 3000 K forsterite isotherm close to $V/V_X = 0.8$. The uncertainty in the pressure is similar to the size of the symbols.

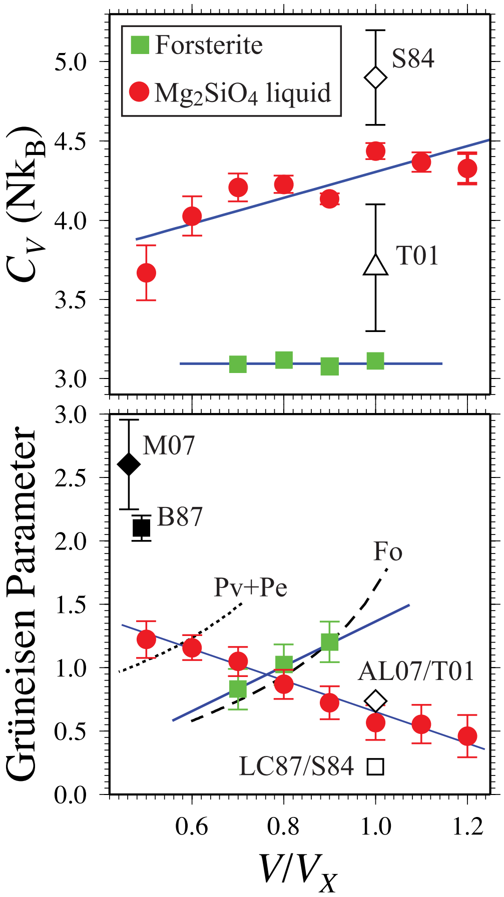

Figure 2.3: (a) Isochoric heat capacity (C_V) and (b) Grüneisen parameter (γ) of liquid (red circles) and forsterite (green squares) as a function of volume. Blue curves show the linear fit for the respective properties (see text). At ambient conditions, C_V falls between experimental estimates determined by Stebbins et al. (1984) (S84) and Tangeman et al. (2001) (T01), while Tangeman et al. (2001), Ai and Lange (2008) (AL07/T01), and Stebbins et al. (1984), Lange (1997), Ai and Lange (2008) (AL07/S84). While liquid γ values increase with compression, high pressure values are notably less than estimates from shock loading (M07, Mosenfelder et al., 2007; B87, Brown et al., 1987a. Forsterite (Fo) γ values are in excellent agreement with the values calculated from experimental data (dashed line; Stixrude and Lithgow-Bertelloni, 2005), while γ for an isochemical assemblage of perovskite + periclase (Pv+Pe) (dotted line; Stixrude and Lithgow-Bertelloni, 2005) is higher by a value similar to the increasing trend in the liquid.

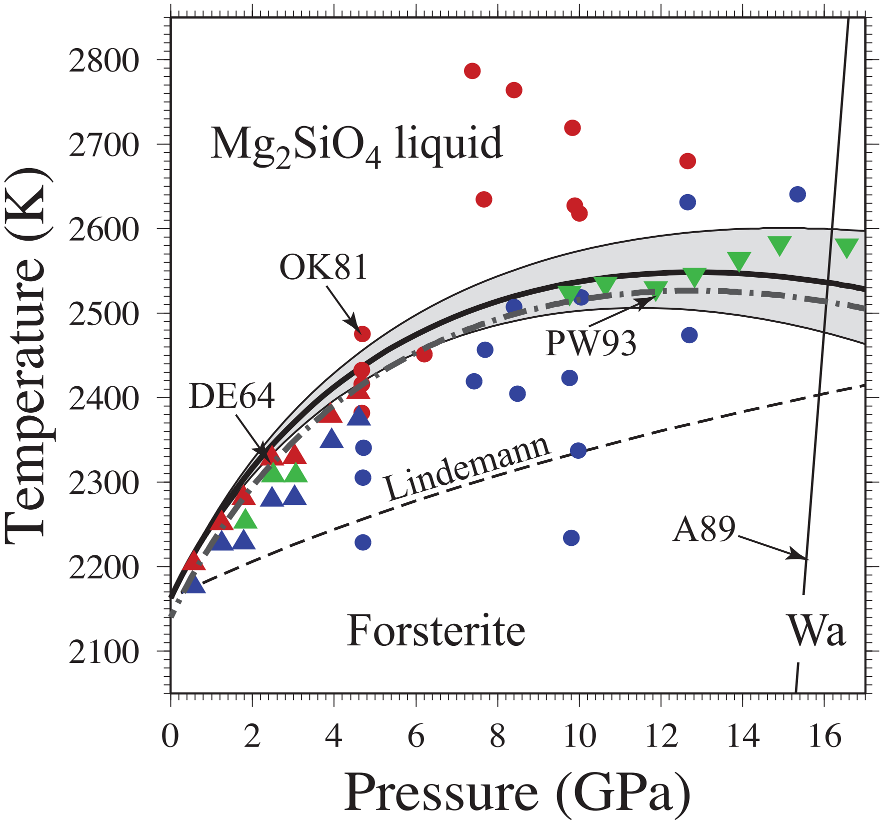

Figure 2.4: First principles molecular dynamics melting curve for forsterite. The curve is obtained by integrating the Clausius-Clapeyron equation (2.14), with the 0 GPa experimental melting point (Bowen and Andersen, 1914) of $T_{M_0} = 2163\,\mathrm{K}$ (thick black line) or $T_{M_0} = 2140\,\mathrm{K}$ (thick dot-dashed line) as integration constant. The grey envelope on either side of the 2163 K melting curve is based on integration with the upper and lower bounds of uncertainty in volume and enthalpy (see text). The slope becomes negative around 13 GPa due to a density crossover of the liquid relative to stable forsterite. Experimental data of Ohtani and Kumazawa (1981) (OK81; circles), Presnall and Walter (1993) (PW93; inverted triangles), Davis and England (1964) (DE64; triangles) are shown for observations of liquid (red symbols), crystal (blue symbols) and liquid-crystal coexistence (green symbols). The forsterite-wadsleyite (Wa) transition (thin black line) is from Akaogi et al. (1989) (A89). The Lindemann law melting curve obtained from the root mean square displacement $\langle u_{rms} \rangle$ in solid forsterite is also shown (dashed line).

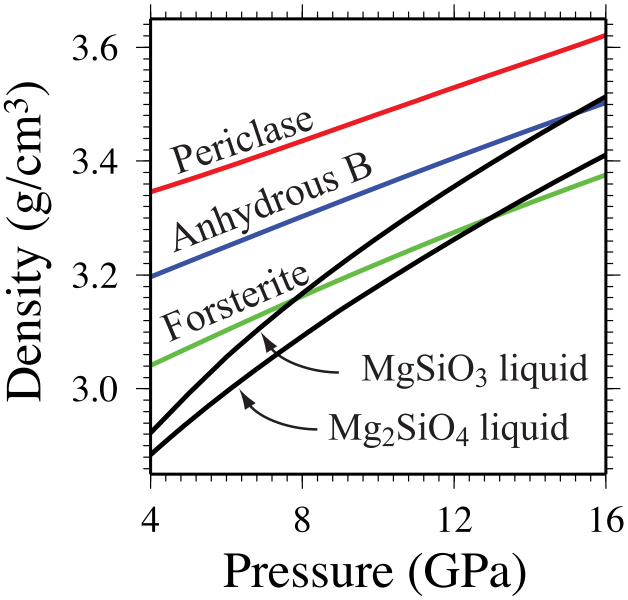

Figure 2.5: Density contrast expected during incongruent melting of forsterite. Contrasts are along the calculated melting curve, between Mg_2SiO_4 and $MgSiO_3$ liquids and the phases that will comprise the residual crystalline assemblage (Presnall and Gasparik, 1990). The density of anhydrous B is estimated by ideal mixing of periclase (Karki et al., 2000a) and forsterite.

Figure 2.6: Theoretical Hugoniot for Mg_2SiO_4 liquid. Hugoniot curves calculated using the thermodynamic model of Stixrude and Lithgow-Bertelloni (2005) for crystalline phase assemblages (Pv - perovskite; PPv - post perovskite; Pe - periclase; St - stishovite), as well as Mg_2SiO_4 liquid (this study) and a partially molten mixture of Pe and $MgSiO_3$ liquid (Stixrude and Karki, 2005), compared to the pressure-volume shock measurements for forsterite (Fo) and wadsleyite (Wa) (WA83 - Watt and Ahrens, 1983; JA79 - Jackson and Ahrens, 1979; M07 - Mosenfelder et al., 2007 and to pressure-temperature shock measurements of forsterite and olivine (Fo90) (Luo et al., 2004). Data point labels refer to the shot numbers assigned by Mosenfelder et al. (2007).

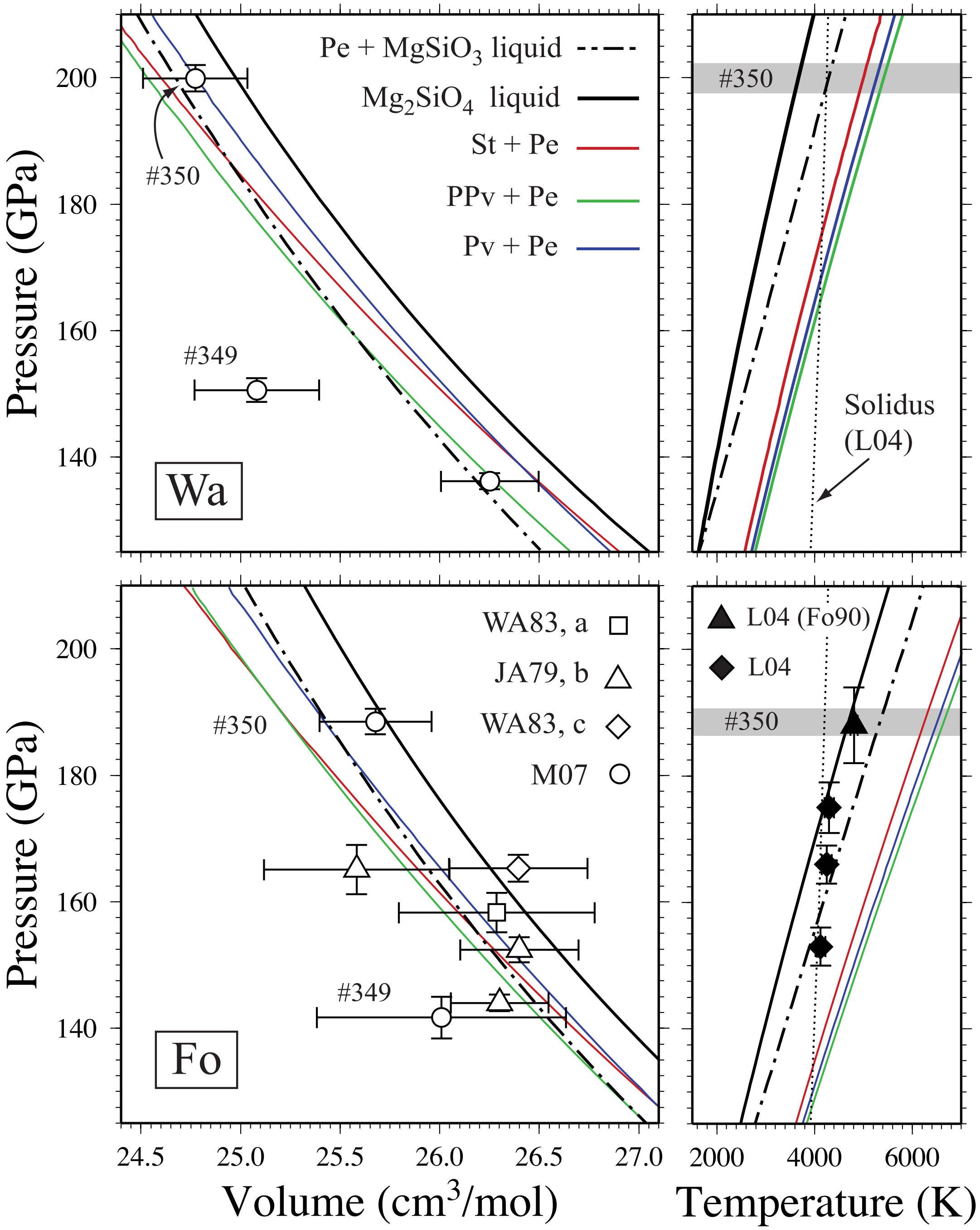
Pe + MgSiO$_3$ liquid
Mg$_2$SiO$_4$ liquid
St + Pe
PPv + Pe
Pv + Pe
#350
#349
Wa
#350
Solidus (L04)
WA83, a
JA79, b
WA83, c
M07
#350
#349
Fo
L04 (Fo90)
L04
#350
Pressure (GPa)
200
180
160
140
24.5
25.0
25.5
26.0
26.5
27.0
Volume (cm^3/mol)
2000
4000
6000
Temperature (K)

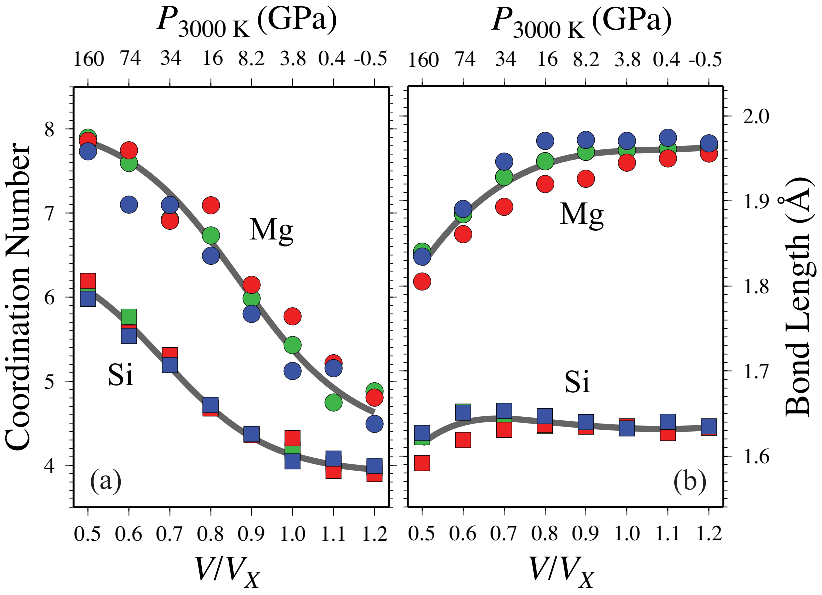

Figure 2.7: (a) Si-O and Mg-O coordination, and (b) Si-O bond lengths as a function of volume. Temperature is indicated by the color of the symbols: 3000 K (blue), 4000 K (green) and 6000 K (red).

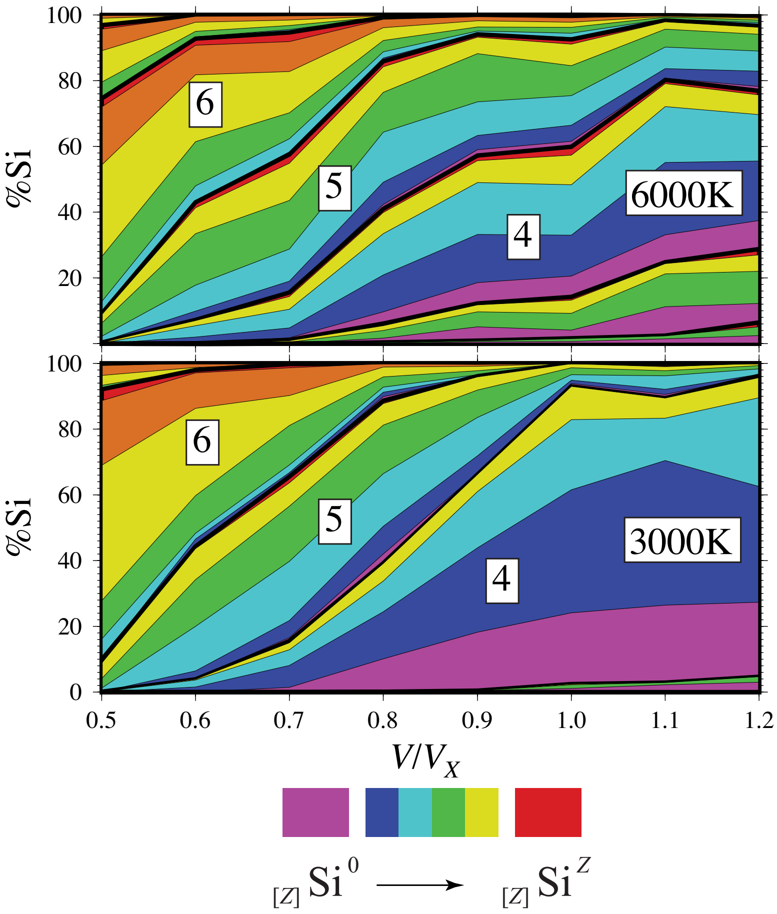

Figure 2.8: Polymerization state of the liquid as a function of volume, at 3000 K and 6000 K, as expressed by the abundance of $_{[Z]}\mathrm{Si}^{\mathrm{O}_B}$ species. Colors cycle from purple ($_{[Z]}\mathrm{Si}^0$; zero bridging oxygens) to red ($_{[Z]}\mathrm{Si}^Z$; all oxygens are bridging) with the number of intermediate colors depending on the coordination number. Coordination 'zones' result as the mean coordination number increases with compression. At 3000 K, low pressure liquids are almost entirely four-fold coordinated, with the majority of polyhedra free-floating (purple) or bound in dimers (dark blue). The liquid moves through intermediate states and five-fold coordination upon compression, reaching almost entirely six-fold coordination at the highest compression, where the majority of polyhedra have only one or two non-bridging oxygens.

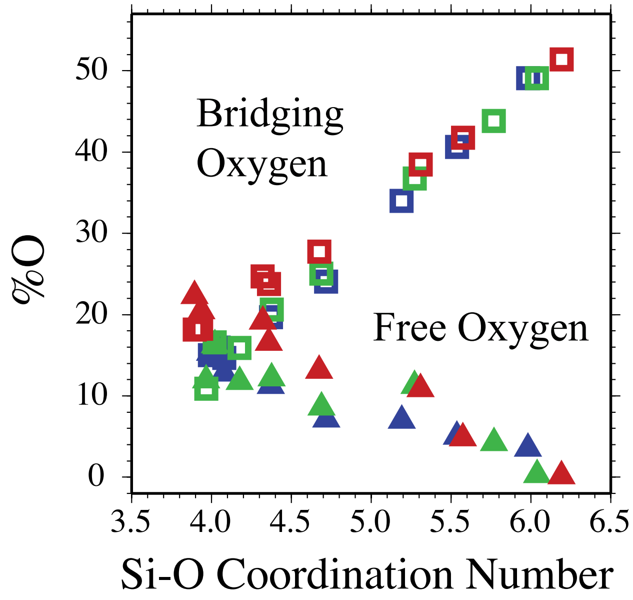

Figure 2.9: Free and bridging oxygen abundance as a function of Si-O coordination. Note that $\|\partial \mathrm{O}_B/\partial Z\| > \|\partial \mathrm{O}_F/\partial Z\|$, indicating that coordination increase occurs more frequently through the transformation of a non-bridging oxygen (O_N) into a O_B, compared to a O_F transforming to a O_N.

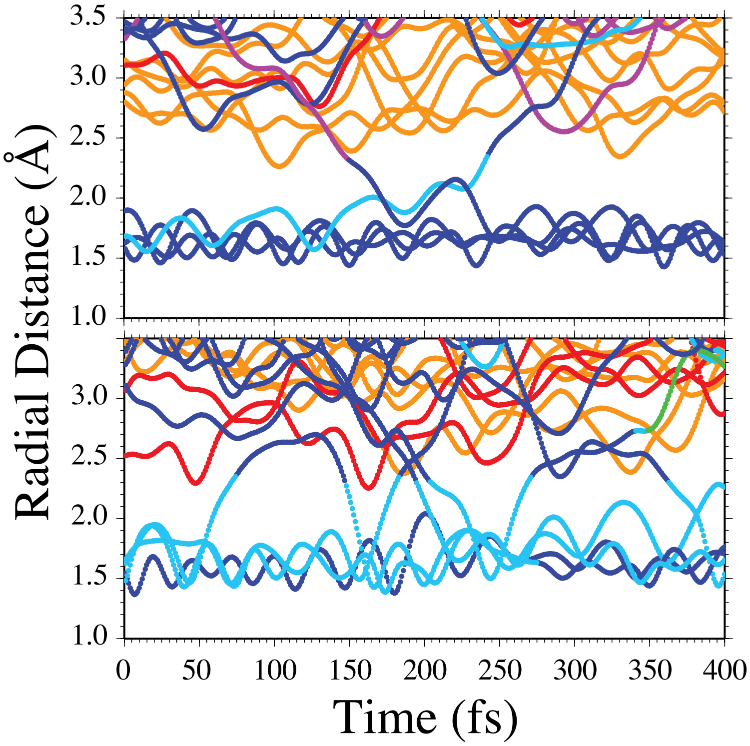

Figure 2.10: Time series of atomic movement within a 3.5 Å sphere relative to a reference silicon atom, illustrating dynamic speciation changes. Each trace represents a single atom, with speciation indicated by the color: free oxygen - purple; non-bridging oxygen - navy blue; bridging oxygen - light blue; three coordinated oxygen - green; magnesium - orange; silicon - red. In the top panel a free oxygen approaches the reference silicon eventually binding with it to become a non-bridging oxygen (equation 2.24). Coincident with this process a bridging oxygen moves away from the reference silicon, eventually losing its bond to become non-bridging (bound to a different silicon) (reverse of equation 2.23). The bottom panel shows a number of events where oxygen atoms transform between bridging and non-bridging. Also note the coupled movement of the silicon atom at around $t = 160$ fs, as it exchanges oxygens with the reference silicon.

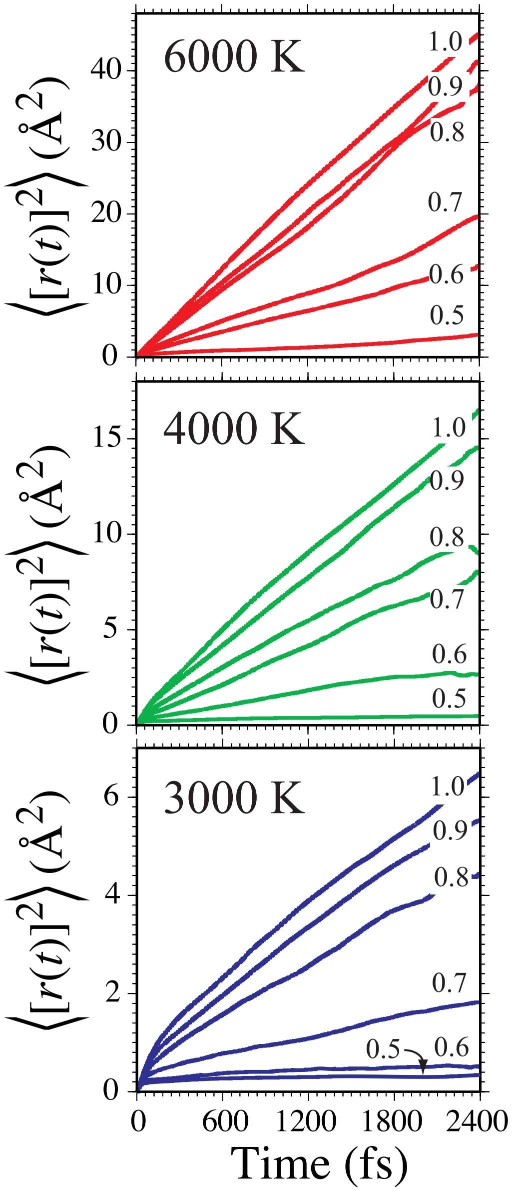

Figure 2.11: Mean square displacement as a function of time. Values increase with a constant slope after ∼ 100 fs, from which the diffusivity is calculated through equation 2.18. Labels refer to V/V_X values.

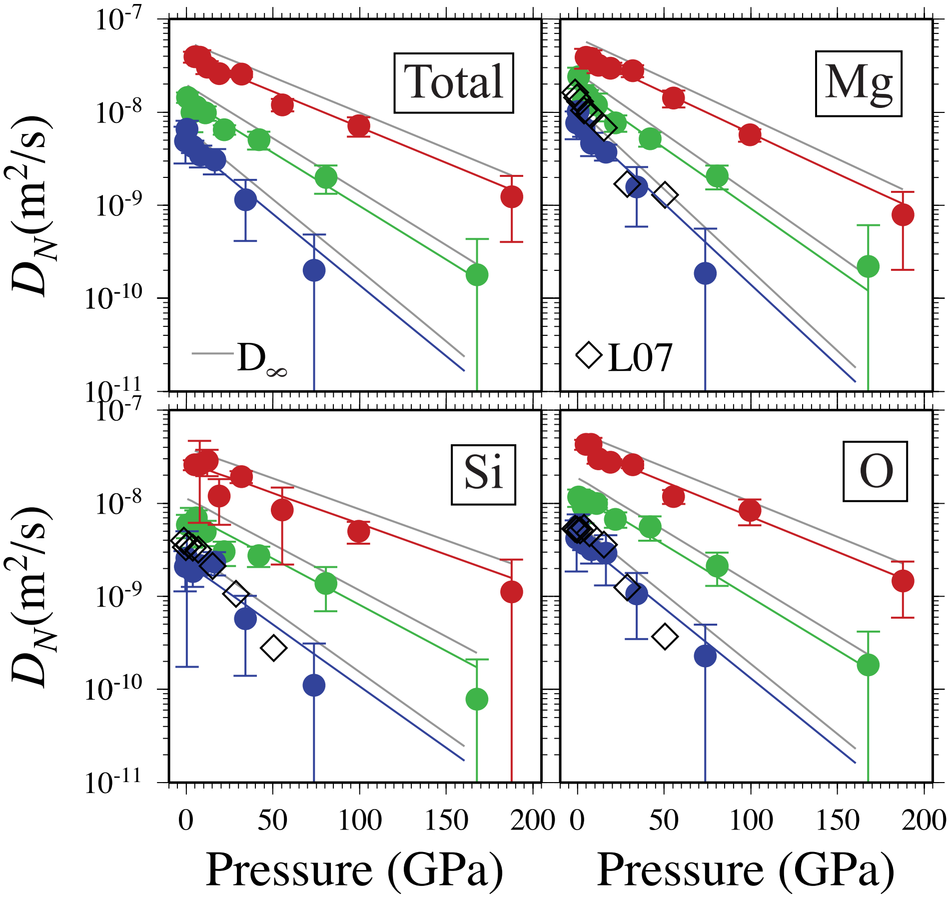

Figure 2.12: Self-diffusion coefficient (D_N) of Mg_2SiO_4 liquid, fit with an Arrhenius relation (equation 2.19). Fit parameters are reported in Table 2.5. Gray lines indicate the Arrhenius fit to diffusivities corrected for finite system size through equation 2.20. Open diamonds show the empirical potential calculation results of Lacks et al. (2007) (L07).

CHAPTER III

Self-Consistent Thermodynamic Description of Silicate Liquids, with Application to Shock Melting of MgO Periclase and $MgSiO_3$ Perovskite

3.1 Abstract

We develop a self-consistent thermodynamic description of silicate liquids applicable across the entire mantle pressure and temperature regime. The description combines the finite strain free energy expansion with an account of the temperature dependence of liquid properties into a single fundamental relation, while honoring the expected limiting behavior at high volume and temperature. We find that the fundamental relation describes well previous experimental and theoretical results for liquid MgO, $MgSiO_3$, Mg_2SiO_4 and SiO_2. We apply the description to calculate melting curves and Hugoniots of solid and liquid MgO and $MgSiO_3$. For periclase, we find a melting temperature at the CMB of 7360 ± 350 K, with the solid Hugoniot crossing the melting curve at 344 GPa, 8880 K, and the liquid Hugoniot crossing at 452 GPa, 9170 K. For complete shock melting of periclase we predict a density increase of 0.12 $\mathrm{g/cm^3}$ and a sound speed decrease of 2.3 km/s. For perovskite, we find a melting temperature at the CMB of 5320 ± 210 K with the perovskite section of the enstatite Hugoniot crossing the melting curve at 155 GPa, 5520 K, and the liquid Hugoniot crossing at 242 GPa, 6290 K. For complete shock melting of perovskite

along the enstatite principle hugoniot, we predict a density increase of 0.10 g/cm^3, with a sound speed decrease of 2.6 km/s.

3.2 Introduction

Liquid state thermodynamics have long played a central role in the study of mantle petrology and geochemistry. The chemical history of a terrestrial planet is intimately tied to its thermal history through fractionation processes associated with cooling of a magma ocean and melting of a solid mantle (Miller et al., 1991b; Ohtani, 1988; Solomatov and Stevenson, 1993; Agee and Walker, 1993; Ohtani and Sawamoto, 1987). Furthermore, seismic observations suggest the presence of partial melt atop the 410 km discontinuity, (Revenaugh and Sipkin, 1994; Song et al., 1994) and at the base of the mantle (Williams and Garnero, 1996; Revenaugh and Meyer, 1997; Garnero and Helmberger, 1995). Accurate estimates of the solidus temperature of the mantle at those depths can thus provide key constraints on the composition and geothermal profile of the mantle. Decompression melting close to the free surface is responsible for the mafic and ultramafic igneous rocks that, together with mantle xenoliths, provide our most direct chemical observations of the Earth's deep interior. Accurate estimates of the equations of state and phase equilibria of melts constrain the pressures at which melting primarily occurs (Asimow et al., 1995; McKenzie and Bickle, 1988) and the depth limits from which melts can reach the surface (Agee and Walker, 1988, 1993; Stolper et al., 1981; Rigden et al., 1989; de Koker et al., 2008a).

While the equations of state of many solid mantle phases have been measured to lower mantle pressures (Stixrude and Lithgow-Bertelloni, 2005, and references therein), the experimental study of silicate liquids remains challenging, even at low pressures (Shen and Lazor, 1995; Rigden et al., 1989; Lange and Carmichael, 1987;

Lange and Navrotsky, 1992; Ai and Lange, 2008). First principles molecular dynamics (FPMD) studies (Stixrude and Karki, 2005; Karki et al., 2006, 2007; de Koker et al., 2008a; Wan et al., 2007; Sun, 2008; Trave et al., 2002; Laudernet et al., 2004) have recently focused on silicate liquids at pressures and temperatures relevant to the full extent of the Earth's mantle, and revealed rich structural and thermodynamic compressional behavior. Thermodynamic properties were found to be significantly different from those of solids: the isochoric heat capacity (C_V) is generally larger than the high temperature limit seen in solids ($3\,Nk_B$) and varies significantly on compression; the Grüneisen parameter (γ) increases with compression, whereas it always decreases during isostructural compression of solids.

In this study, we develop a self consistent thermodynamic description of liquid state thermodynamics relevant to silicate liquids at pressures and temperatures characteristic of mantles and magma oceans associated with terrestrial planets. We apply our thermodynamic formalism to the description of FPMD results, using these as a guide to the functional forms and the relevant physics. In addition, we derive an anharmonic fundamental relation for solids at high temperature (i.e. in the classical limit), which we combine with the liquid descriptions to obtain melting curves and theoretical Hugoniot loci for MgO periclase and $MgSiO_3$ perovskite.

3.3 Previous Work

PVT equations of state were first described for the ideal gas (Boyle, 1662; Clapeyron, 1834). This equation of state treats particles as independent, and is thus unable to describe the liquid-vapor transition. At high pressures, this relation is commonly applied to stellar interiors (Chandrasekhar, 1939; Phillips, 1994), but it does not capture the comparative incompressibility of terrestrial materials such as silicate liquids at the conditions characteristic of planetary interiors. Subsequent Van der Waals (van der Waals, 1873) and Redlich-Kwong (Redlich and Kwong, 1949) equations were formulated to capture critical behavior and the liquid-vapor transition, but are only valid close to ambient conditions, predicting very incompressible behavior at higher pressure. Modified Redlich-Kwong forms (Brodholt and Wood, 1993; Halbach and Chatterjee, 1982; Holland and Powell, 1991) address this problem, but require many free parameters to constrain. Similarly, other empirical and semi-empirical forms, developed primarily for interpolation of large datasets of liquid and gas thermodynamic properties (Pitzer and Sterner, 1994; Belonoshko and Saxena, 1992; Span and Wagner, 1997), also require large numbers of free parameters with consequent poor extrapolation and unphysical oscillations in thermodynamic properties. None of these existing forms are thus able to capture the essentials of silicate liquids over a geophysically interesting pressure range with sufficiently few free parameters.

The Thomas-Fermi model (Slater and Krutter, 1935; Feynman et al., 1949; Marshak and Bethe, 1940) gives an approximate description of the equation of state at very high pressures, based on a simplified model of the electronic charge density. It has been successfully applied to stellar and gas giant interiors, but is too approximate to offer detailed insight into the behavior of materials within the Earth's interior (Knopoff and Uffen, 1954; Birch, 1952). In high pressure hydrodynamic simulations these problems are remedied to some extent by the quotidian equation of state (More et al., 1988; Young and Corey, 1995), but it assumes a number of simplifying relationships, in particular the Dulong-Petit law and the Lindemann law, which have been shown not to hold for silicate melts (Stixrude and Karki, 2005; Karki et al., 2007; de Koker et al., 2008a; Jeanloz and Roufosse, 1982; Stebbins et al., 1984).

Experimental studies of the equation of state of silicate liquids have been almost entirely limited to ambient and uppermost mantle pressures (Lange and Carmichael, 1987; Lange, 1997; Courtial et al., 1997; Ai and Lange, 2008; Agee and Walker, 1988, 1993; Bottinga, 1985), with only a few shock loading and multi-anvil measurements giving insight into the equation of state at pressures characteristic of the lower mantle (Mosenfelder et al., 2007; Rigden et al., 1984, 1989; Chen et al., 2002; Miller et al., 1991a; Suzuki and Ohtani, 2003; Sakamaki et al., 2006; Matsukage et al., 2005). These results have shown that simple polynomial descriptions of $P(V,T)$ or $V(P,T)$ (Ghiorso and Sack, 1995) are inadequate at high pressure (Ghiorso, 2004). The Birch-Murnaghan equation of state (Birch, 1952, 1978) has been widely used (Lange, 2003, 2007; Ghiorso et al., 2002; Rigden et al., 1989; Sakamaki et al., 2006; Matsukage et al., 2005; Suzuki and Ohtani, 2003), but more high pressure data are needed to test its validity, while its suitability for silicate liquids has been questioned on a theoretical basis (Hofmeister, 1993; Ghiorso, 2004).

A key issue which has not been carefully addressed, is the thermal contribution to the liquid equation of state. In describing the temperature and pressure dependence of a material simultaneously, great care must be taken to preserve thermodynamic self consistency (Ghiorso et al., 2002; Ghiorso, 2004; Dorogokupets, 2000; Pavese, 2002; Ai and Lange, 2008). The main goal of the work presented here is to derive a thermodynamic treatment of silicate liquids which self consistently describes their pressure and temperature dependence.

3.4 Fundamental Thermodynamic Relations

We obtain an expression for the Helmholtz free energy

$$F = F(V,T), \tag{3.1}$$

as a function of its natural variables, volume (V) and temperature (T). We follow Callen (1985) in referring to $F(V,T)$ as a "fundamental thermodynamic relation", because all thermodynamic information may be self consistently obtained from it by differentiation, reduction of derivatives and Legendre transformations,

$$P = -\left(\frac{\partial F}{\partial V}\right)_T, \tag{3.2}$$

$$S = -\left(\frac{\partial F}{\partial T}\right)_V, \tag{3.3}$$

$$K_T = V\left(\frac{\partial^2 F}{\partial V^2}\right)_T, \tag{3.4}$$

$$\alpha K_T = -\left(\frac{\partial^2 F}{\partial V \partial T}\right), \tag{3.5}$$

$$C_V = -T\left(\frac{\partial^2 F}{\partial T^2}\right)_V, \tag{3.6}$$

$$\frac{\gamma}{V} = \frac{\alpha K_T}{C_V}, \tag{3.7}$$

$$\frac{K_S}{K_T} = \frac{C_P}{C_V} = (1 + T\alpha\gamma), \tag{3.8}$$

$$G = F - V\left(\frac{\partial F}{\partial V}\right)_T = F + PV, \tag{3.9}$$

$$E = F - T\left(\frac{\partial F}{\partial T}\right)_V = F + TS, \tag{3.10}$$

$$H = F - T\left(\frac{\partial F}{\partial T}\right)_V - V\left(\frac{\partial F}{\partial V}\right)_T = F + TS + PV. \tag{3.11}$$

By deriving all the equilibrium thermodynamics from a single function, self-consistency among properties is guaranteed through Maxwell relations.

3.4.1 Liquids

The fundamental thermodynamic relation of the liquid phase is

$$F(V,T) = F_{ig}(V,T) + F_{xs}(V,T) + F_{el}(V,T), \tag{3.12}$$

where we have assumed the three contributions to F to be separable (McQuarrie, 1984). These contributions are: an ideal gas term (F_{ig}) arising from atomic momenta, an excess term (F_{xs}) which accounts for inter-atomic interaction, and an electronic term (F_{el}) describing the free energy due to thermal excitation of electrons.

Nuclear Momentum Contribution

The atomic momentum contribution (ideal gas term) is given by an ideal mixture of the free energy ($F_{ig\alpha}$) of the respective species (α) that make up the liquid (Lupis, 1983; McQuarrie, 1984),

$$F_{ig} = \sum_{\alpha} N_\alpha F_{ig\alpha} + RT \sum_{\alpha} N_\alpha \ln X_\alpha, \tag{3.13}$$

$$F_{ig\alpha} = -RT \left[\ln V_\alpha + \frac{3}{2} \ln T + \frac{3}{2} \ln \left(\frac{m_\alpha k_B}{2\pi\hbar^2} \right) + 1 \right], \tag{3.14}$$

where

$$X_\alpha = \frac{N_\alpha}{\sum_\alpha N_\alpha}, \tag{3.15}$$

and V_α and m_α is the volume and mass of one particle of type α.

Excess Nuclear Contribution

Let $f = f(V)$ and $\theta = \theta(T)$ such that $f(V_0) = 0$ and $\theta(T_0) = 0$, with V_0 and T_0 the reference volume and temperature at pressure P_0. Expand F_{xs} in f and θ about the origin in a two-dimensional Taylor series. From the resulting excess free energy

$$F_{xs}(V,T) = \sum_{i=0} \sum_{j=0} \frac{a_{ij}}{i!j!} f^i \theta^j, \tag{3.16}$$

follows

$$P_{xs}(V,T) = -\frac{\partial f}{\partial V}\sum_{i=0}\sum_{j=0}\frac{ia_{ij}}{i!j!}f^{i-1}\theta^{j}, \tag{3.17}$$

$$S_{xs}(V,T) = -\frac{\partial \theta}{\partial T}\sum_{i=0}\sum_{j=0}\frac{ja_{ij}}{i!j!}f^{i}\theta^{j-1}, \tag{3.18}$$

$$E_{xs}(V,T) = \sum_{i=0}\sum_{j=0}\frac{a_{ij}}{i!j!}f^{i}\theta^{j-1}\left(\theta - jT\frac{\partial \theta}{\partial T}\right). \tag{3.19}$$

$$K_{Txs}(V,T) = V\sum_{i=0}\sum_{j=0}\frac{ia_{ij}}{i!j!}\theta^{j}\left[\left(\frac{\partial^2 f}{\partial V^2}\right)f^{i-1} + \left(\frac{\partial f}{\partial V}\right)^2(i-1)f^{i-2}\right] \tag{3.20}$$

$$\alpha K_{Txs}(V,T) = -\left(\frac{\partial f}{\partial V}\right)\left(\frac{\partial \theta}{\partial T}\right)\sum_{i=0}\sum_{j=0}\frac{ija_{ij}}{i!j!}f^{i-1}\theta^{j-1} \tag{3.21}$$

$$C_{Vxs}(V,T) = -T\sum_{i=0}\sum_{j=0}\frac{ja_{ij}}{i!j!}f^{i}\left[\left(\frac{\partial^2 \theta}{\partial T^2}\right)\theta^{j-1} + \left(\frac{\partial \theta}{\partial T}\right)^2(j-1)\theta^{j-2}\right] \tag{3.22}$$

We follow Birch (1952) and choose

$$f = \frac{1}{n}\left[\left(\frac{V_0}{V}\right)^{\frac{n}{3}} - 1\right], \tag{3.23}$$

which reduces to the Eularian finite strain for $n = 2$. For $T = T_0$, Equation 3.17 reduces to the Birch-Murnaghan equation of state.

By describing the thermal variable as

$$\theta = \left[\left(\frac{T}{T_0}\right)^{m} - 1\right], \tag{3.24}$$

the internal energy (Equation 3.19) becomes

$$E_{xs}(V,T) = \sum_{i=0}\sum_{j=0}\frac{a_{ij}}{i!j!}f^{i}\theta^{j-1}\left[\left(\frac{T}{T_0}\right)^{m} - 1\right]^{j-1}\left[\left(\frac{T}{T_0}\right)^{m}(1-jm) - 1\right], \tag{3.25}$$

which after rearrangement of terms, may be summarized as

$$E_{xs}(V,T) = \sum_{j=0} b_j(f)T^{jm}, \tag{3.26}$$

where the coefficients b_j are polynomials in f that contain the excess free energy expansion coefficients a_{ij}.

Thermal Electronic Contribution

In a simple metallic system, the electronic heat capacity is (Wallace, 2002)

$$C_{Vel}^{cond}(V,T) = \frac{\pi^2}{3} n(\epsilon_f) k_B T, \tag{3.27}$$

where $n(\epsilon_f)$ is the electronic density of states at the Fermi level, ϵ_f.

Silicate liquids are known to become conductive at high temperatures (Hicks et al., 2006). Thus we adapt Equation 3.27 to apply only above the temperature of onset (T_{el}) where the liquid becomes conductive

$$C_{Vel}(V,T) = \begin{cases} \beta(V)\left[T - T_{el}(V)\right] & T \geq T_{el} \\ 0 & T < T_{el} \end{cases} . \tag{3.28}$$

With the electronic entropy (S_{el}) and free energy (F_{el}) zero at T_{el}, integration yields

$$S_{el} = \beta \left[T - T_{el} - T_{el} \ln \frac{T}{T_{el}} \right], \tag{3.29}$$

$$F_{el} = -\beta \left[\frac{1}{2}\left(T^2 - T_{el}^2\right) - T T_{el} \ln \frac{T}{T_{el}} \right], \tag{3.30}$$

from which the electronic energy (E_{el}) and pressure (P_{el}) follow as

$$E_{el} = \frac{1}{2}\beta \left[T - T_{el}\right]^2, \tag{3.31}$$

$$P_{el} = \frac{\partial \beta}{\partial V}\left[\frac{1}{2}\left(T^2 - T_{el}^2\right) - T T_{el} \ln \frac{T}{T_{el}} \right] + \beta \frac{\partial T_{el}}{\partial V}\left[(T - T_{el}) - T \ln \frac{T}{T_{el}} \right]. \tag{3.32}$$

The volume dependence of β and T_{el} is described by a power law relation

$$\beta = \beta_0 \left(\frac{V}{V_0}\right)^{\xi}, \tag{3.33}$$

$$T_{el} = T_{el_0} \left(\frac{V}{V_0}\right)^{\eta}. \tag{3.34}$$

Limiting Behavior

The liquid relation is designed such that the infinite temperature and volume limits capture the expected material properties at those conditions, given suitable values of n and m. Limiting values of the excess properties, derived from Equations 3.17-3.22 are summarized in Table 3.1. Total values follow from addition of ideal gas, excess and thermal electronic terms, with the exception of the Grüneisen parameter, which is not additive.

Also, the non-electronic portion of the liquid relation captures the physics of the liquid-vapor transition at moderately high volumes. The power law parameterization of volume dependence in the thermal electronic contribution does not capture the limiting behavior of F_{el} as $V \to \infty$.

3.4.2 Solids at High Temperature

We follow previous studies (Stixrude and Lithgow-Bertelloni, 2005; Stixrude and Bukowinski, 1990a) and describe the solid by

$$F = F_0 + F_{cmp} + F_{th}, \tag{3.35}$$

with the assumption that the various contributions to F are separable. F_0 is the free energy at reference volume (V_0) and temperature (T_0), F_{cmp} and F_{th} are the compressional and thermal contributions to the free energy, respectively. The contribution due to atomic momentum (F_{ig}) is negligible, and the thermal electronic contribution (F_{el}) is zero for silicate minerals.

F_{cmp} is expressed as an expansion in terms of the Eularian finite strain (f) (Birch, 1952, 1978)

$$F_{cmp} = 9K_{T0}V_0\left[\frac{1}{2}f^2 + \frac{1}{6}a_3f^3 + \frac{1}{24}a_4f^4 + \cdots\right], \tag{3.36}$$

$$a_3 = 3\left(K'_{T0} - 4\right), \tag{3.37}$$

$$a_4 = 9\left[K_{T0}K''_{T0} + K'_{T0}\left(K'_{T0} - 7\right)\right] + 143, \tag{3.38}$$

$$f = \frac{1}{2}\left[\left(\frac{V_0}{V}\right)^{\frac{2}{3}} - 1\right]. \tag{3.39}$$

The familiar form of the Birch-Murnaghan equation of state follows as the isothermal volume derivative of Equation 3.36. V_0, K_{T0}, K'_{T0}, and K''_{T0} are the volume, bulk modulus, and its frst and second pressure derivatives at zero pressure and a reference temperature (T_0).

F_{th} is obtained by integration of the entropy

$$F_{th} = -\int_{T_0}^{T} S(V,T')dT', \tag{3.40}$$

with the entropy obtained as

$$S(V,T) = S(V_0,T_0) + \int_{V_0}^{V} \alpha K_T(V',T_0)dV' + \int_{T_0}^{T} \frac{C_V(V,T')}{T'}dT', \tag{3.41}$$

with

$$\alpha K_T = \frac{C_V\gamma}{V}. \tag{3.42}$$

C_V is taken as constant, although its value is not constrained to allow for anharmonicity. Through the Maxwell relation

$$\frac{1}{T}\left(\frac{\partial C_V}{\partial V}\right)_T = \frac{1}{V}\left(\frac{\partial C_V\gamma}{\partial T}\right)_V, \tag{3.43}$$

C_V independent of V and T implies that γ is independent of T. We describe $\gamma(V)$ as

$$\gamma = \gamma_0 + \gamma_1 V^{-n/3} + \gamma_2 V^{-2n/3}, \tag{3.44}$$

which follows from

$$\gamma = \gamma_0' + \gamma_1' f + \gamma_2' f^2, \tag{3.45}$$

a form akin to Equation 44 of Stixrude and Lithgow-Bertelloni (2005).

F_{th} now follows as

$$\begin{aligned} F_{th}(V,T) = {} & -S_0\left[T - T_0\right] - C_V\left[T\ln\frac{T}{T_0} - [T-T_0]\right] \\ & -C_V\left[\gamma_0\ln\left(\frac{V}{V_0}\right) - \frac{3}{n}\gamma_1(V^{-\frac{n}{3}} - V_0^{-\frac{n}{3}}) \right. \\ & \left. -\frac{3}{2n}\gamma_2(V^{-\frac{2n}{3}} - V_0^{-\frac{2n}{3}})\right]\left[T - T_0\right], \end{aligned} \tag{3.46}$$

Applying Equations 3.2, 3.3 and 3.10 to Equation 3.35, we have

$$\begin{aligned} E(V,T) = {} & E_0 + 9K_{T0}V_0\left[\frac{1}{2}f^2 + \frac{1}{6}a_3 f^3 + \frac{a_4}{24}f^4 + \cdots\right] + C_V\left[T - T_0\right] \\ & +T_0 C_V\left[\gamma_0\ln\left(\frac{V}{V_0}\right) - \frac{3}{n}\gamma_1(V^{-\frac{n}{3}} - V_0^{-\frac{n}{3}}) - \frac{3}{2n}\gamma_2(V^{-\frac{2n}{3}} - V_0^{-\frac{2n}{3}})\right], \end{aligned} \tag{3.47}$$

$$\begin{aligned} P(V,T) = {} & 3K_{T0}(1+2f)^{\frac{5}{2}}\left[f + \frac{a_3}{2}f^2 + \frac{a_4}{6}f^3 + \cdots\right] \\ & +C_V\left[\frac{\gamma_0}{V} + \gamma_1 V^{-\frac{(n+3)}{3}} + \gamma_2 V^{-\frac{(2n+3)}{3}}\right]\left[T - T_0\right]. \end{aligned} \tag{3.48}$$

3.5 First Principles Molecular Dynamics Simulations

To test the solid and liquid fundamental relations, we use FPMD simulation results for MgO periclase, $MgSiO_3$ perovskite (Stixrude and Karki, 2005), as well as liquid MgO (Karki et al., 2006), $MgSiO_3$ (Stixrude and Karki, 2005), Mg_2SiO_4 (de Koker et al., 2008a) and SiO_2 (Karki et al., 2007). With the application to shock melting in mind, we supplement the $MgSiO_3$ and MgO liquid data of Stixrude and Karki (2005) and Karki et al. (2006) at high pressures. These systems are melted at higher temperatures (8000 K and 15000 K, respectively), and then cooled isochorically as in previous calculations. Mg_2SiO_4 and $MgSiO_3$ liquid simulations at 2000 K are also added to improve constraints at ambient pressure.

Our computational technique is described in detail in our previous work, and we only highlight a few salient points here. FPMD simulations based on DFT (Hohenberg and Kohn, 1964; Kohn and Sham, 1965) are performed as implemented in the VASP plane-wave code (Kresse and Furthmüller, 1996), using pseudopotentials (Kresse and Hafner, 1994), the local density approximation (LDA, Ceperley and Alder (1980)) and a single k-point at the Brillouin zone center (Γ). Systems consist of 64 (MgO liquid and periclase), 112 (Mg_2SiO_4 liquid), 80 ($MgSiO_3$ liquid and perovskite) and 72 atoms (SiO_2 liquid) in a periodic simulation cell. The cell is cubic for liquid simulations, with solid cell dimensions adjusted to obtain a hydrostatic stress tensor. Simulations are performed in the canonical ensemble (constant NVT) through the use of a thermostat (Nosé, 1984). We use a time increment of 1.0 fs and run durations of at least 3000 fs, sufficient for converged values of the pressure and internal energy, the mean values of which are obtained using the blocking method (Flyvberg and Petersen, 1989).

The pressure is adjusted to correct for the finite basis set (Francis and Payne, 1990) and overbinding of the LDA (Karki et al., 2001; Oganov et al., 2001b). Because atomic motion is entirely classical at all temperatures (Allen and Tildesley, 1987), energy values do not capture the quantum effects characteristic of atomic vibrations at low temperature in solids, and are thus only physical in the limit of high temperatures. Quantum corrections can be applied (Wigner, 1932; Kirkwood, 1933; Oganov et al., 2001a), but our interest here is in solids close to melting where such corrections will be negligible.

The electronic entropy is obtained from the electronic eigenvalues (ϵ) as (Kresse and Furthmüller, 1996; Mermin, 1965)

$$S_{el}^{DFT} = -2k_B \sum_i \left[\phi(\epsilon_i) \ln \phi(\epsilon_i) + [1-\phi(\epsilon_i)] \ln [1-\phi(\epsilon_i)]\right], \tag{3.49}$$

where

$$\phi(\epsilon_i) = \frac{1}{e^{\beta(\epsilon_i - \epsilon_f)} + 1} \tag{3.50}$$

is the Fermi-Dirac distribution function, with $\beta = k_B T$. The Fermi energy (ϵ_f) is determined by the number criterion.

We stress that our FPMD simulations do not give information on the value of the entropy. S_0 must be constrained by additional information. In liquids it is obtained by specifying the free energy of the coexisting solid at a fixed melting point, chosen from the available experimental estimates. For solids, S_0 may be found from the vibrational density of states, which we obtain here using an experimental implementation of the Debye approximation which partially accounts for intrinsic anharmonicity (Stixrude and Lithgow-Bertelloni, 2005). However, E, H, P and all second and higher order derivatives may be derived without knowing the value of S_0; it is only needed for values of the entropy (S) and free energy (F and G), properties crucial to phase equilibria calculations.

To perform the fit for the liquid, the order to which the excess free energy is expanded must be determined and n and m specified. We denote the respective orders of expansion in f and θ as $\mathcal{O}_f$ and $\mathcal{O}_\theta$. Considering its overwhelming success in fitting and extrapolating high pressure equations of state, we adopt the Eularian finite strain in our description for melts as well, i.e. we use $n = 2$. Similarly, the correct limiting behavior as $T \rightarrow \infty$ requires $m < 1$ for $\mathcal{O}_\theta = 1$ and $m < 1/2$ for

$\mathcal{O}_\theta = 2$. The value of m is therefore allowed to vary based on the composition and the value of $\mathcal{O}_\theta$ required to fit the data.

To constrain the liquid relation, electronic entropy is fit to Equation 3.29, with the subsequent E_{el} and P_{el} removed from the total E and P values to obtain the excess values. E_{xs} and P_{xs} are fit to Equations 3.19 and 3.17 in a single least squares inversion to constrain coefficients a_{ij}, which in turn are related to physical properties at the reference pressure (P_0) and temperature (T_0) (Equations A.5-A.19). To minimize the number of free parameters, we explicitly exclude coefficients that do not notably improve the fit.

The free parameters which describe the solid - E_0, C_V, γ_0, γ_1, γ_2, K_0, K_0' - are similarly determined by inversion of the total E and P from FPMD to Equations 3.47 and 3.48.

3.6 Results

3.6.1 Liquids

Consistent with the conclusions in the original studies, we find that MgO, Mg_2SiO_4 and $MgSiO_3$ liquid equations of state are sufficiently described with a third order finite strain expansion ($\mathcal{O}_f = 3$), while SiO_2 requires a fifth order expansion ($\mathcal{O}_f = 5$) (Figures 3.1-3.4). Values of m that optimize the first ($\mathcal{O}_\theta = 1$) and second ($\mathcal{O}_\theta = 2$) order fits to the FPMD data, are noted in Table 3.2. The quality of the optimal $\mathcal{O}_\theta = 1$ fit is only sufficient in the case of MgO, and marginally so for Mg_2SiO_4. High temperature low density points are poorly accounted for in all three silicate compositions, with the misfit increasing with SiO_2 content. These discrepancies are remedied using $\mathcal{O}_\theta = 2$. However, in SiO_2 the $\mathcal{O}_\theta = 2$ fit is significantly further improved when excluding the $T = 6000\,\mathrm{K}$, $V/V_X = 0.8$, 0.9 and 1.0 points (white circles in Figure 3.4). These points are at pressures below 15 GPa, where 6000 K is of less geophysical importance.

For the $\mathcal{O}_f = 3$ cases, we find that allowing a_{31} to vary as a free parameter improves the $\mathcal{O}_f = 3$, $\mathcal{O}_\theta = 1$ fits notably, as does including a_{31}, a_{22}, and a_{32} for $\mathcal{O}_\theta = 2$. In contrast, a_{51}, a_{42}, and a_{52} does not improve the SiO_2 fit to a meaningful extent, and are thus explicitly excluded to reduce the number of free parameters.

Thermodynamic properties at ambient pressure for the respective liquids are compared to previous experimental and theoretical estimates in Tables 3.3 - 3.6. Only partial molar experimental data for MgO liquid is available, and we mostly compare to previous theoretical estimates. Equation of state parameters differ slightly from those of Karki et al. (2006), because all the data are used in obtaining the equation of state fit. The added simulations at 2000 K for Mg_2SiO_4 and $MgSiO_3$ enable us to draw a direct comparison to experimental data collected at 1773 K. As with MgO, the 3000 K equation of state parameters parameters of SiO_2 also differ somewhat from those obtained by Karki et al. (2007). Notable discrepancies with α, C_V, and C_P likely result from the large thermal extrapolation. Uncertainties in each thermodynamic property is estimated by repeated fitting to a Monte-Carlo perturbation of the simulation data, constrained by its error estimates. Changes in C_V and γ with compression are shown in Figure 3.5.

The ability of the liquid relation to capture the thermodynamics of the liquid-vapor transition is illustrated by extrapolating the Mg_2SiO_4 3000 K isotherm to very large volumes (Figure 3.6). We ignore the thermal electronic contribution here, as it will likely vanish at these large volumes. The extrapolation yields a liquid-vapor coexistence pressure of 0.13 GPa, and a heat of vaporization of 1420 kJ/mol, comparible to the heat of vaporization of forsterite used in giant impact studies (Benz et al., 1989; Canup, 2004).

3.6.2 Solids

A third order finite strain expansion is sufficient to fit the periclase simulations up to a compression ratio of $V/V_X = 0.45$, but we find that a fourth order expansion is required to account for the points at higher pressures (Figure 3.7). Thermodynamic parameters at ambient pressure and reference temperature compare favorably with values from experiment and previous theoretical calculations (Table 3.7). Comparison of γ at high pressure with experiment and theory are also good (Figure 3.7, inset).

As found by Stixrude and Karki (2005), a third order finite strain expansion is sufficient to fit the perovskite results, including the added data points at $V/V_X = 0.4$ (Figure 3.8). Comparison of 0 GPa thermodynamic parameters to previous FPMD results is excellent (Table 3.8). The compressional decrease of γ compares reasonably with previous first principles estimates (Oganov et al., 2001a; Karki et al., 2000b) (Figure 3.8, inset).

3.7 Applications

To illustrate the power of our method, we compute ambient pressure thermodynamic properties as well as high pressure melting curves and Hugoniots for MgO periclase and $MgSiO_3$ perovskite (enstatite unshocked state), and the corresponding liquid phases. Our aim is to obtain a direct comparison of our simulation results to a broad range of low pressure measurements and high pressure shock loading data and make predictions of trends to expect where measurements have not yet been made.

Melting curves are obtained by finding the loci of pressure and temperature where solid and liquid Gibbs free energies correspond. As we use a reference melting temperature to constrain the liquid free energy from that of the solid, this approach is equivalent to integration of the Clapeyron equation, with integration done analytically rather than numerically.

For a given volume (V_h) or density (ρ_h), the theoretical Hugoniot state is given by the temperature (T_h) at which the pressure (P_h) and internal energy (E_h) satisfy the Rankine-Hugoniot relation,

$$(E_h - E_r) = -\frac{1}{2}(P_h + P_r)(V_h - V_r)\,, \tag{3.51}$$

where E_r and V_r is respectively the internal energy and volume of the unshocked state defined by pressure P_r and temperature T_r. We compute E_r from first principles by relaxing enstatite and periclase at the experimental volume V_r, and applying a thermal correction to account for the difference in energy between static conditions and 300 K (Stixrude and Lithgow-Bertelloni, 2005).

In a solid the longitudinal wave velocity is given by

$$v_P = \sqrt{\frac{K_S + 4/3\mu}{\rho}}. \tag{3.52}$$

where μ is the shear modulus. In liquids, $\mu = 0$, and v_P reduces to the bulk sound velocity

$$v_B = \sqrt{\frac{K_S}{\rho}}. \tag{3.53}$$

The sound velocity of the shock compressed phase can be measured in a shock loading experiment, with a large decrease with pressure being a strong indication of shock melting. For the liquid, we compute v_B along the Hugoniot (Equation 3.8) and compare to v_P of the solid, calculated with Equation 3.52 from experimental data using the model of Stixrude and Lithgow-Bertelloni (2005).

Consistent with previous theoretical estimates (Cohen and Gong, 1994; Vočadlo and Price, 1996; Belonoshko and Dubrovinsky, 1996; Strachan et al., 2001; Alfe, 2005), our periclase melting curve (Figure 3.9), has a distinctly higher initial Clapeyron slope than the experimental determination of Zerr and Boehler (1994). The slope remains positive over the entire pressure range considered. We find a melting temperature at the CMB of $7360 \pm 354\,\mathrm{K}$, which is 780 K lower than the LDA melting curve obtained by Alfe (2005) through FPMD simulation of direct phase coexistance.

The FPMD periclase Hugoniot agrees very well with the measured pressure-density Hugoniot (Svendsen and Ahrens, 1987; Duffy and Ahrens, 1995; Vassiliou and Ahrens, 1981; Marsh, 1980), but is somewhat warmer than the temperature measurements of Svendsen and Ahrens (1987). The periclase Hugoniot crosses the melting curve at $P = 344\,\mathrm{GPa}$, $T = 8880\,\mathrm{K}$, with the liquid phase periclase Hugoniot crossing the melting curve at $P = 452\,\mathrm{GPa}$, $T = 9170\,\mathrm{K}$. Complete shock melting is predicted to result in a $\sim 0.12\,\mathrm{g/cm^3}$ density increase and a 2.3 km/s sound velocity decrease along the Hugoniot. Liquid-solid sound velocity contrast along the Hugoniot is found from the p-wave velocity of periclase, calculated from experimental data using the model of Stixrude and Lithgow-Bertelloni (2005).

Our perovskite melting curve (Figure 3.10) is almost identical to the result of Stixrude and Karki (2005), being somewhat colder than the measurements of Zerr and Boehler (1993) and Shen and Lazor (1995), though warmer than the experimental measurements of Knittle and Jeanloz (1989), Heinz and Jeanloz (1987) and Sweeney and Heinz (1998), as well as the result of Stixrude and Bukowinski (1990a). The Clapeyron slope remains positive over the entire pressure range considered. We find a melting temperature at the CMB of $5320 \pm 213\,\mathrm{K}$, which is more than 2000 K lower than the melting temperature obtained by Brodholt (2008) through FPMD simulation of direct phase coexistance.

The FPMD perovskite component of the enstatite principle Hugoniot compares well with the measured pressure-density Hugoniot (Akins et al., 2004) points at 149 GPa and 170 GPa, but is notably warmer than the temperature measurements of Luo et al. (2004). The perovskite Hugoniot crosses the melting curve at $P = 155\,\mathrm{GPa}$, $T = 5520\,\mathrm{K}$, with the liquid phase Hugoniot crossing the melting curve at $P = 242\,\mathrm{GPa}$, $T = 6290\,\mathrm{K}$. Complete shock melting is predicted to result in a $\sim 0.10\,\mathrm{g/cm^3}$ density increase and a 2.6 km/s sound velocity decrease along the Hugoniot.

3.8 Discussion

For a given order of expansion in the thermal variable ($\mathcal{O}_\theta$), values of m are remarkably similar for all four compositions considered. We will highlight the implications of two aspects of this result. Firstly, the values of m obtained, especially in the $\mathcal{O}_\theta = 1$ case, and secondly, the degree to which $\mathcal{O}_\theta = 1$ fails in Mg_2SiO_4, $MgSiO_3$, and especially in SiO_2.

For $\mathcal{O}_\theta = 1$ and $m = 3/5$, the internal energy expression derived from our liquid fundamental relation (Equation 3.26) is equivalent to the theoretical expression for the energy of cold, dense, simple liquids (Rosenfeld and Tarazona, 1998)

$$E_{theory}(T) = E_{ig}(T) + c_0 + c_1 T^{\frac{3}{5}}, \tag{3.54}$$

where c_0 and c_1 are isochoric constants. Although one could perform independent $E(T)$ fits of Equation 3.54 along individual isochors and obtain reasonable agreement to the FPMD results, such an approach gives no information on the temperature dependence of the pressure. Taking this additional information into account, as is done in fitting the liquid fundamental relation to both $P(V,T)$ and $E(V,T)$ simultaneously, yields m values markedly higher than 3/5 for all the $\mathcal{O}_\theta = 1$ fits, though still consistent with limiting behavior constraints. Previous semi-emprical MD studies of

SiO_2, $MgSiO_3$, and Mg_2SiO_4 liquids (Saika-Voivod et al., 2001; Ghiorso et al., 2006; Martin et al., 2006) found Equation 3.54 to hold for individual isochors, but failed to account for all thermodynamic properties in a self-consistent way. The contrast of our results with these previous studies highlights the importance of describing the liquid state thermodynamic properties in terms of a single fundamental relation without rigid constraints on the functional form of individual properties.

For m independent of volume and temperature, $\mathcal{O}_\theta = 1$ fits do not sufficiently account for all the data in Mg_2SiO_4, $MgSiO_3$ and SiO_2 liquids, again in contrast to findings of the semi-emprical MD studies of these compositions (Saika-Voivod et al., 2001; Ghiorso et al., 2006; Martin et al., 2006). This difference likely results from changes in the $\mathrm{Si}-\mathrm{O}$ bonds with temperature not captured by semi-empirical techniques, and highlights the importance of obtaining the interatomic forces from the electronic structure *in situ* during molecular dynamics.

For $\mathcal{O}_\theta = 2$ and $\mathcal{O}_f = 3$, the fit for the excess free energy contribution requires ten free parameters (thirteen for $\mathcal{O}_f = 5$), in addition to the four required to fit the electronic contribution. As a result, the $\mathcal{O}_\theta = 2$ relation does not extrapolate well, and can only be applied within a grid of NVT points as we do here.

Nonetheless, $\mathcal{O}_\theta = 1$ fits do give reasonable results at temperatures within $\sim 1000\,\mathrm{K}$ of freezing. Equation 3.16 can therefore potentially be applied to silicate liquids of natural compositions at geophysically relevant conditions, constrained using experimental data. Since $a_{02} = 0$ for $\mathcal{O}_\theta = 1$, Equation A.10 gives

$$m = \frac{C_{Vxs0}}{S_{xs0}} + 1, \tag{3.55}$$

for $m \neq 0$. Therefore m can be found with knowledge of the liquid S and C_V at the reference point, making application of the liquid fundamental relation to experimental data possible.

The theoretical suitability of a Eularian finite strain expansion for use with highly compressible materials such as silicate liquids has been questioned (Ghiorso et al., 2002; Ghiorso, 2004; Hofmeister, 1993). The two main concerns that have been cited are firstly, that analytical inter-atomic potentials derived from the Birch-Murnaghan equation of state predict non-physical effects for $K_0' > 6$ (Hofmeister, 1993), and secondly, that the equation allows liquid bulk moduli to vanish at large volumes. Experimental and theoretical results for silicate liquids show K_0' values to vary from around 5 to as high as 12 (Rigden et al., 1989; Ai and Lange, 2008; Lange, 2003, 2007; Stixrude and Karki, 2005; Karki et al., 2007; de Koker et al., 2008a; Sun, 2008). These high values reflect the ability of silicate liquids to access structural compression mechanisms not available to solids, such as coordination and ring statistics, which enable liquids to become very compressible at high temperature and low density. The Hofmeister (1993) prediction only applies to simple ionic compounds, in which only the bond length is altered upon compression, and is therefore not relevant to silicate liquids. The second concern cited is, in fact, an asset of the finite strain expansion. When combined with an ideal gas term, as we have done, the relation shows a van der Waals loop (Figure 3.6), and thus also captures the thermodynamics of the liquid-vapor transition.

The relation for solids works well over the large range of pressure and temperature we consider, though the absence of a quantum correction requires caution in comparison with experimental equation of state data below about 1000 K. The requirement of a fourth order finite strain expansion for periclase is primarily due to the very large pressures attained in the smallest volume considered ($V/V_X = 0.35$). The relation requires only seven (eight for periclase) free parameters, and can therefore be extrapolated to higher temperatures and pressures with reasonable confidence.

The discrepancy between our respective melting curves for periclase and perovskite, and those determined by FPMD simulation of two-phase coexistence by Alfe (2005) and Brodholt (2008), highlights the pitfalls of the two-phase method. In the FPMD implementation, these simulations are limited in size to hundreds of atoms, with the result that the periodic boundary condition may favor the stability of the crystalline phase, and overestimate the melting temperature. Also, surface effects at the melt-crystal interface will alter a large portion of both the liquid and crystalline portions in such small systems, with the result that the simulation may not reflect the equilibrium phases, and a stable crystalline core will be absent. Of course, these surface effects are interesting in their own right, and two-phase coexistence simulations do have the advantage of giving estimates of melting completely independent of experimental input. However, the melting temperatures of geophysically relevant compositions are known at ambient pressures to within uncertainties far smaller than those realistically obtainable in two-phase FPMD simulations. Therefore, combining such experimental measurements with our approach is likely to provide the most accurate estimate of congruent melting temperatures at very high pressure.

Agreement with pressure-density Hugoniot data for perovskite is excellent, but poor for shock temperature measurements. Pressure-density measurements are far more robust than shock temperature measurements, in which a number of assumptions about the radiative properties of the material are made, including that the shock front is smooth and non-reflecting, and that the electronic temperature is in equilibrium with that of the lattice at the shock front. A Hugoniot obtained using the self consistent thermodynamic model of Stixrude and Lithgow-Bertelloni (2005), constrained with a variety of experimental data, is very similar to the FPMD Hugoniot, showing similar disagreement with the shock measured temperatures. The perovskite Hugoniot intersects the melting curve at a pressure slightly smaller than where incipient melting has been inferred on the measured enstatite Hugoniot, suggesting that some extent of overdriving into a superheated solid state may be present in the experimental data. Somewhat more troubling, however, is the large discrepancy between the density increase along the Hugoniot upon melting predicted by theory and observed in experiment. The three inferred liquid points in the data of Akins et al. (2004) are at pressures smaller than that at which the theoretical liquid Hugoniot crosses the melting curve, and are likely only partially molten. Indeed, extrapolation of the inferred experimental liquid Hugoniot to higher pressures gives good agreement with the theoretical prediction. The observed large increase in density may result from processes related to shock-induced phase transformation, such as a double shock front (Ng et al., 1991).

The fact that the liquid Hugoniot is at a larger density than that of the solid in both periclase as well as perovskite should not be confused with a density crossover. The larger liquid Hugoniot density results simply due to thermal contraction as heat is absorbed during melting. Indeed, along the melting curves the densities of periclase and perovskite remain larger than that of the respective coexisting liquids, as reflected by the positive Clapeyron slopes.

3.9 Conclusion

By extending the finite strain description of materials at high pressure of Birch (1952, 1978) to account for the thermal free energy contribution, we have constructed a thermodynamic description of silicate liquids that is self-consistent and requires relatively few free parameters. Application of this relation to silicate liquids simulated by FPMD reveals that the effect of excited electronic states cannot be ignored in these materials at temperatures well above that of melting, and that existing theoretical predictions for the temperature dependence of the liquid free energy fail for silicate liquids at high temperature.

Of particular geophysical interest is the melting of mantle minerals at deep lower mantle pressures, most readily achieved in shock loading experiments. Shock melting may be identified by large changes in the temperature, discontinuities in density, and a marked decrease in the sound velocity of the shocked state measured along the Hugoniot. We are able to apply the thermodynamic description to obtain melting curves and Hugoniot loci for perovskite and periclase, compare to existing shock loading measurements and make quantitative predictions of each of the melting criteria.

3.10 Acknowledgements

This research was supported by the National Science Foundation under Grants EAR-0409074 and EAR-0409121. Computing facilities were provided by CCT at Louisiana State University and by CAC at the University of Michgan.

Table 3.1: Limiting behavior of excess thermodynamic properties, and values of n and m required for these limits to hold. $\mathcal{O}_\theta$ denotes the order of expansion in θ.

	$\lim_{V\to\infty}$	n	$\lim_{T\to\infty}$	m
P_{xs}	0	> -3	∞	> 0
S_{xs}	$const(T)$	> 0	0	$< 1/\mathcal{O}_\theta$
E_{xs}	$const(T)$	> 0	∞	> 0
K_{Txs}	0	$> -3/2$	∞	> 0
αK_{Txs}	0	> -3	0	$< 1/\mathcal{O}_\theta$
C_{Vxs}	$const(T)$	> 0	0	$< 1/\mathcal{O}_\theta$

Table 3.2: m values used in liquids F_{xs} fits

$\mathcal{O}_\theta$	MgO	Mg_2SiO_4	$MgSiO_3$	SiO_2	Theory[a]
1	0.874	0.881	0.869	0.828	0.6
2	0.417	0.416	0.371	0.370	-

[a] Rosenfeld and Tarazona (1998)

Table 3.3: Thermodynamic properties of FPMD MgO liquid at 0 GPa, 3000 K

	This study	Previous Estimates
$V\,(\mathrm{cm}^3/\mathrm{mol})$	16.46	16.50^{a}, 16.26^{b}, $16.03^{c,d}$, 16.03^{f}
K_T (GPa)	33.2 (2)	30.8 (29)^{a}, 59.2^{b}
K_S (GPa)	43.1 (8)	33 (1)^{h}
K'_T	4.81	5.03 (33)^{a}, 3.83^{b}
$\alpha\,(10^{-}6\,\mathrm{K}^{-1})$	103.2 (1)	204^{f}
$S\,(\mathrm{Nk_B})^{\ddagger}$	10.51 (5)†	$11.03^{d,e}$
$C_V\, Nk_B$	3.5 (5)	3.0 (3)^{a}
$C_P\, Nk_B$	4.6 (9)	5.19 (3)^{g}
γ	0.97 (3)	0.95 (7)^{a}, $1.25^{f,g,h}$

[a] Karki et al. (2006); [b] Cohen and Gong (1994); [c] Karki et al. (2000b); [d] Alfe (2005); [e] Stixrude and Lithgow-Bertelloni (2005); [f] Lange (1997); [g] Stebbins et al. (1984); [h] Ai and Lange (2008)

‡ Value at melting temperature of 3070 K (Riley, 1966; Zerr and Boehler, 1994)

† Based on periclase Gibbs free energy at an assumed melting point of 3070 K, 0 GPa (Riley, 1966)

Table 3.4: Thermodynamic properties of FPMD Mg_2SiO_4 liquid at 0 GPa, 1773 K

	This study	Previous Estimates
V (cm^3/mol)	52.35	50.9^{a}
K_T (GPa)	17.9 (6)	$24.3\,(1)^{b}$
K_S (GPa)	19.5 (7)	$27\,(3)^{b}$
K'_T	8.92	$6.9^{d,*}$
$\alpha\,(10^{-}6\,\mathrm{K}^{-1})$	106 (2)	$122\,(7)^{a}$
$S\,(\mathrm{Nk_B})^{\ddagger}$	$8.5\,(3)^{\dagger}$	$8.10\,(16)^{g,h}$
$C_V\,Nk_B$	3.7 (5)	$3.7\,(4)^{a,e}$
$C_P\,Nk_B$	4.0 (6)	$3.9\,(4)^{e}$, $5.1\,3^{f}$
γ	0.46 (2)	$0.56\,(3)^{a,b,f}$, $0.69\,(4)^{a,b,e}$

[a] Lange (1997); [b] Ai and Lange (2008); [c] Rivers and Carmichael (1987); [d] Rigden et al. (1989); [e] Tangeman et al. (2001); [f] Stebbins et al. (1984); [g] Navrotsky et al. (1989); [h] Stixrude and Karki (2005)

[*] Value for $CaMgSi_2O_6$

[‡] Value at melting temperature of 2163 K (Bowen and Andersen, 1914)

[†] Based on forsterite Gibbs free energy at an assumed melting point of 2163 K, 0 GPa (de Koker et al., 2008a)

Table 3.5: Thermodynamic properties of FPMD $MgSiO_3$ liquid at 0 GPa, 1773 K

	This study	Previous Estimates
V (cm^3/mol)	37.63	38.88^{a}
K_T (GPa)	18.7 (5)	$16.81\,(7)^{b}$
K_S (GPa)	19.6 (6)	$22\,(2)^{b}$
K'_T	7.69	$6.9^{d,*}$
α ($10^{-}6\,\mathrm{K}^{-1}$)	72 (2)	$84\,(4)^{a}$, 60^{e}
S ($\mathrm{Nk_B}$)‡	$8.06\,(8)^{\dagger}$	$7.62\,(6)^{g,h}$
$C_V\,Nk_B$	3.4 (6)	$4.2\,(2)^{i}$
$C_P\,Nk_B$	3.5 (7)	$4.61\,(15)^{i}$
γ	0.36 (1)	$0.37\,(14)^{a,b,i}$

[a] Lange (1997); [b] Ai and Lange (2008); [c] Rivers and Carmichael (1987); [d] Rigden et al. (1989); [e] Tomlinson et al. (1958); [g] Richet and Bottinga (1986); [h] Stixrude and Lithgow-Bertelloni (2005); [i] Stebbins et al. (1984)

[*] Value for $CaMgSi_2O_6$

[‡] Value at metastable congruent melting temperature of 1840 K (Bowen and Andersen, 1914)

[†] Based on perovskite Gibbs free energy at an assumed melting point of 2900 K, 25 GPa (Stixrude and Karki, 2005, and references therein)

Table 3.6: Thermodynamic properties of FPMD SiO_2 liquid at 0 GPa, 3000 K

	This study	Previous Estimates
V (cm^3/mol)	27.6	27.6[a], 28.7[b], 28.6[c,b], 26.9[d], 31[h]
K_T (GPa)	8.3 (43)	5.2 (10)[a], 5.1[b]
K_S (GPa)	8.9 (45)	10.6 (6)[i]
K'_T	6.5	22.5 (30)[a]
$\alpha\,(10^{-}6\,\mathrm{K}^{-1})$	129 (9)	40.86[b], $12.3 - 123$[j]
S ($\mathrm{Nk_B}$)	8.92 (12)[†]	8.35[b], 8.26[e,f,g]
$C_V\,Nk_B$	5.4 (6)	5.0 (4)[a]
$C_P\,Nk_B$	5.9 (9)	3.4[b], 3.21 (3)[e]
γ	0.22 (4)	0.2 (1)[a]

[a] Karki et al. (2007); [b] Hudon et al. (2002); [c] Gaetani et al. (1998); [d] Lange (1997); [e] Stebbins et al. (1984); [f] Richet and Bottinga (1986); [g] Stixrude and Lithgow-Bertelloni (2005); [h] Bacon et al. (1960); [i] Ai and Lange (2008); [j] Dingwell et al. (1993)

[†] Based on stishovite gibbs free energy at an assumed melting point of 3120 K, 14 GPa (Zhang et al., 1993; Shen and Lazor, 1995)

Table 3.7: Thermodynamic properties of FPMD MgO periclase at 0 GPa, 2000 K

	This study	Previous Estimates
V (cm^3/mol)	12.2	12.23^a
K_T (GPa)	107.9 (6)	102^a
K_S (GPa)	127 (1)	126^a
K_T'	4.92	4.97^a
$K_T K_T''$	-6.65	-
$C_V\,Nk_B$	3.04 (3)	2.98^a
$C_P\,Nk_B$	3.6 (7)	3.69^a
$\alpha\,(10^{-}6\,\mathrm{K}^{-1})$	59.0 (5)	68.7^a, 53^b, 64^c, 48^d
γ	1.54 (2)	1.72^a, 1.47^e, 1.71^c, 1.69^d

[a] Stixrude and Lithgow-Bertelloni (2005); [b] Touloukian et al. (1977); [c] Karki et al. (2000a); [d] Oganov and Dorogokupets (2003); [e] Isaak et al. (1989)

Table 3.8: Thermodynamic properties of FPMD $MgSiO_3$ perovskite at 0 GPa, 2000 K

	This study	Previous Estimates
$V\,(\mathrm{cm}^3/\mathrm{mol})$	25.87	25.81^a, 26.26^b, 25.73^c
$K_T\,(\mathrm{GPa})$	191 (5)	189.06^a, 181^b, 210.6^c
$K_S\,(\mathrm{GPa})$	217 (11)	212.57^a
K_T'	4.30	4.96^a, 4.67, 4.49^c
$\alpha\,(10^-6\,\mathrm{K}^{-1})$	43 (1)	40^a, 45.2^b,37.3^c
$C_V\,Nk_B$	3.05 (30)	2.97^a, 2.99^b
$C_P\,Nk_B$	3.5 (9)	3.34^a, 3.46^b
γ	1.6 (1)	1.57^a, 1.9^b, 1.51^c

[a] Stixrude and Lithgow-Bertelloni (2005); [b] Karki et al. (2000b); [c] Oganov et al. (2001b)

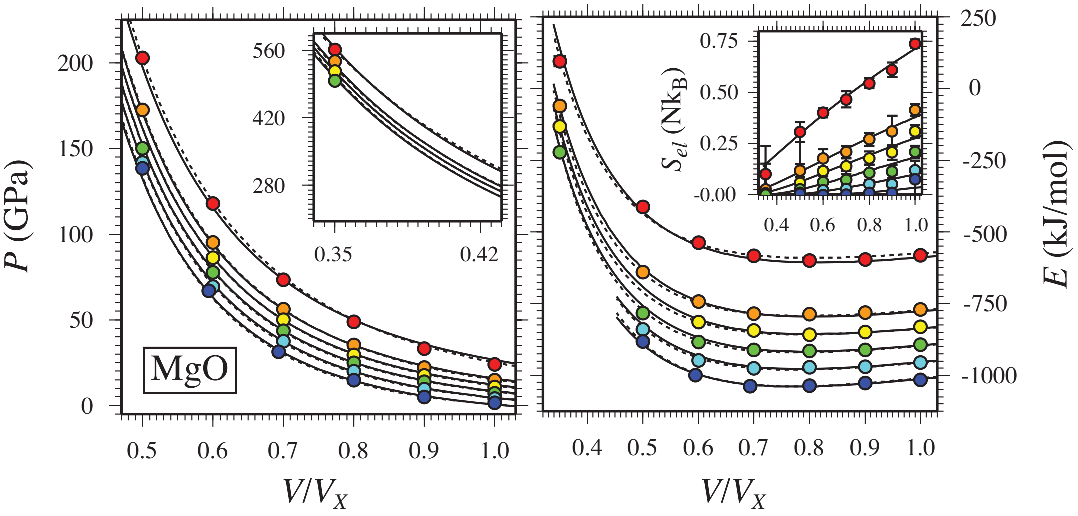

Figure 3.1: Pressure (P), internal energy (E) and thermal electronic entropy (S_{el}) of MgO liquid. Colored circles show values from FPMD simulations at 3000 K (blue), 4000 K (cyan), 5000 K (green), 6000 K (yellow), 7000 K (orange) and 10000 K (red) (Karki et al., 2006, except for points at $V/V_X = 0.35$ and $V/V_X = 0.42$). Black lines indicate the fit of P and E to Equation 3.16 with $\mathcal{O}_\theta = 1$ (solid lines) and $\mathcal{O}_\theta = 2$ (dashed lines), and a third order expansion in finite strain. Errorbars are smaller than the size of the symbols. Inset on the right shows electronic entropy (S_{el}), with black lines indicating the fit to Equation 3.30.

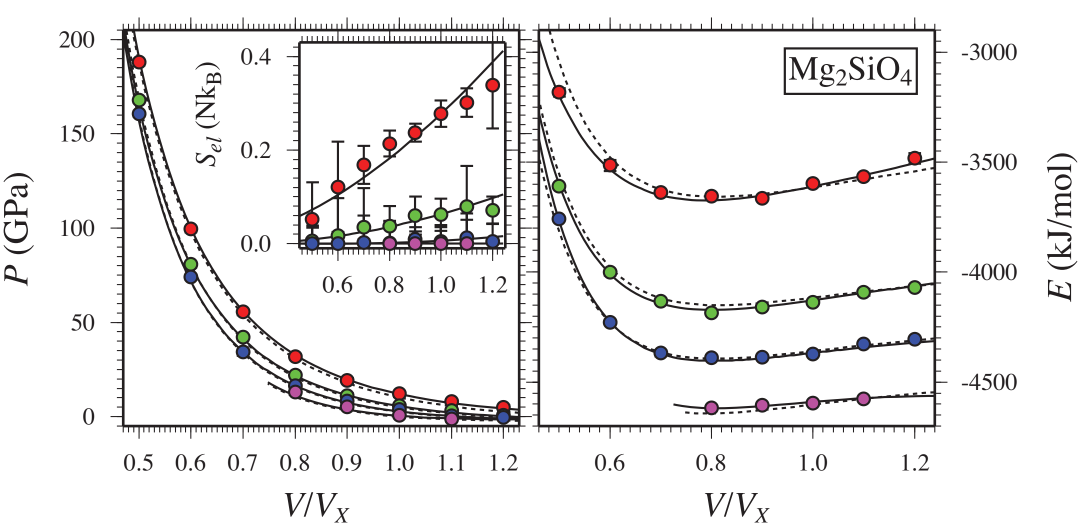

Figure 3.2: Pressure (P), internal energy (E) and thermal electronic entropy (S_{el}) of Mg_2SiO_4 liquid. Colored circles show values from FPMD simulations at 2000 K (purple), 3000 K (blue), 4000 K (green) and 6000 K (red) (de Koker et al., 2008a, except for points at 2000 K). Black lines indicate the fit of P and E to Equation 3.16 with $\mathcal{O}_\theta = 2$ (solid lines) and $\mathcal{O}_\theta = 1$ (dashed lines), and a third order expansion in finite strain. Errorbars are smaller than the size of the symbols. Inset shows electronic entropy (S_{el}), with black lines indicating the fit to Equation 3.30.

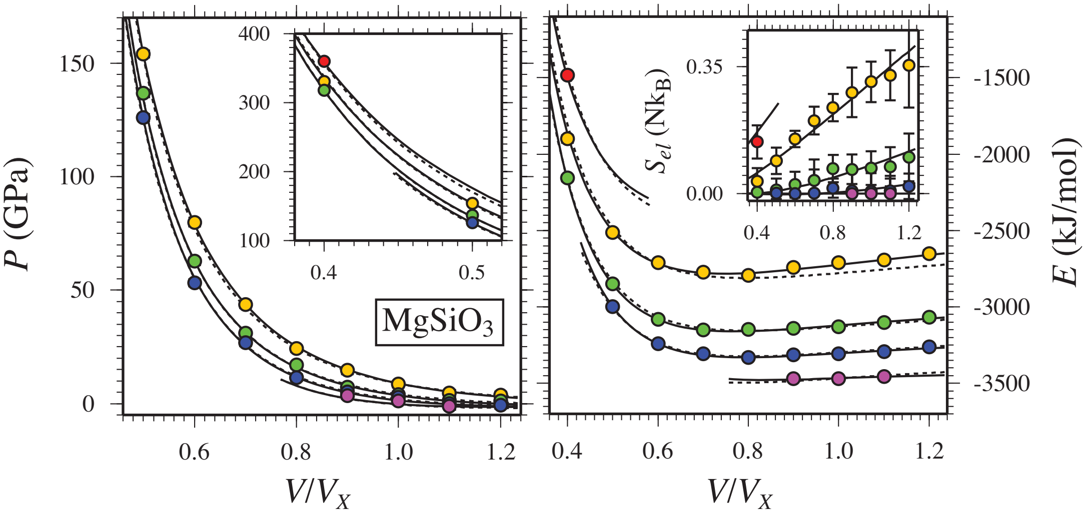

Figure 3.3: Pressure (P), internal energy (E) and thermal electronic entropy (S_{el}) of MgSiO$_3$ liquid. Colored circles show values from FPMD simulations at 2000 K (purple), 3000 K (blue), 4000 K (green), 6000 K (yellow) and 8000 K (red) (Stixrude and Karki, 2005, except for points at 2000 K and at $V/V_X = 0.4$). Black lines indicate the fit of P and E to Equation 3.16 with $\mathcal{O}_\theta = 2$ (solid lines) and $\mathcal{O}_\theta = 1$ (dashed lines), and a third order expansion in finite strain. Errorbars are smaller than the size of the symbols. Inset on the right shows electronic entropy (S_{el}), with black lines indicating the fit to Equation 3.30.

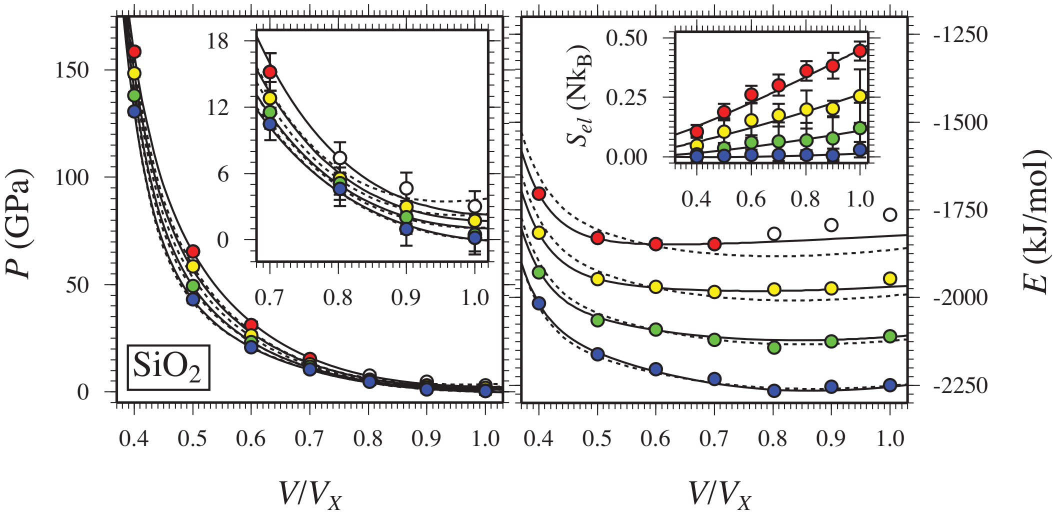

Figure 3.4: Pressure (P), internal energy (E) and thermal electronic entropy (S_{el}) of SiO_2 liquid. Colored circles show values from FPMD simulations at 3000 K (blue), 4000 K (green), 5000 K (yellow) and 6000 K (red, white) (Karki et al., 2007). Black lines indicate the fit of P and E to Equation 3.16 with $\mathcal{O}_\theta = 2$ (solid lines) and $\mathcal{O}_\theta = 1$ (dashed lines), and a fifth order expansion in finite strain. White points are not included in the fit. Errorbars are smaller than the size of the symbols. Inset on the right shows electronic entropy (S_{el}), with black lines indicating the fit to Equation 3.30.

Figure 3.5: Grüneisen parameter (γ) and isochoric heat capacity (C_V) for the respective liquid compositions. γ and C_V (units of Nk_B), follow the trends previously found by independent linear fits of FPMD results along each simulated isochor (white symbols)(Stixrude and Karki, 2005; Karki et al., 2006, 2007; de Koker et al., 2008a). Maxwell relations dictate that the volume dependence of C_V implies γ must be temperature dependent, so that independent isochoric fits are not thermodynamically self-consistent. Such linear fits are also inconsistent with the limiting behavior we require for C_V and γ. Our approach reveals detailed variations in C_V and γ with temperature, but also highlights that caution is required at the edges of the interpolated grid, as well as in extrapolation. Lines are colored by temperature: 3000 K (blue) through 6000 K (red) for SiO_2, $MgSiO_3$ and Mg_2SiO_4; 3000 K (purple) through 7000 K (orange) and 10000 K (red) for MgO

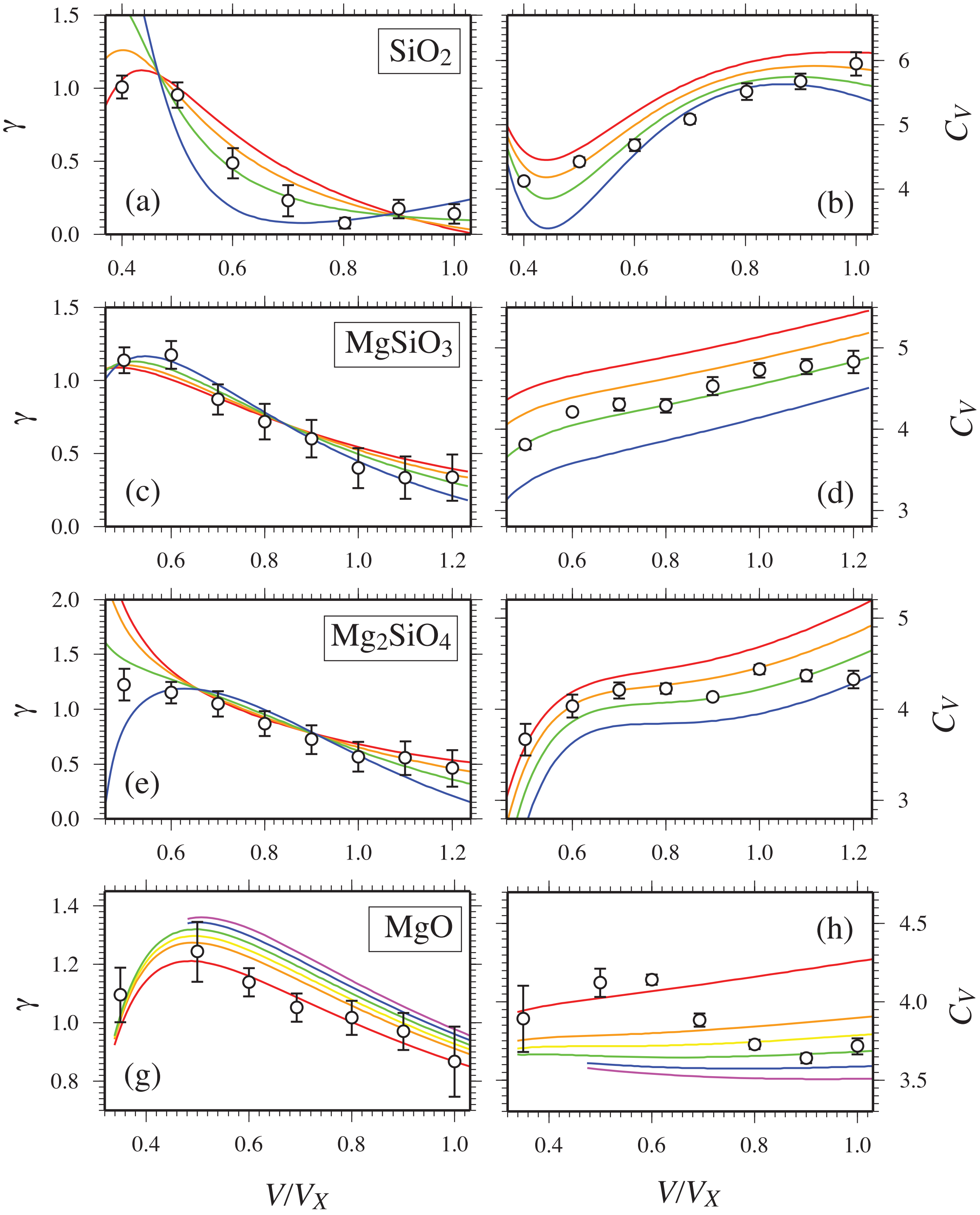
SiO$_2$
MgSiO$_3$
Mg$_2$SiO$_4$
MgO
(a)
(b)
(c)
(d)
(e)
(f)
(g)
(h)
γ
C_V
V/V_X
0.0
0.5
1.0
1.5
2.0
0.8
1.2
1.4
0.4
0.6
0.8
1.0
1.2
3
4
5
6
3.5
4.0
4.5

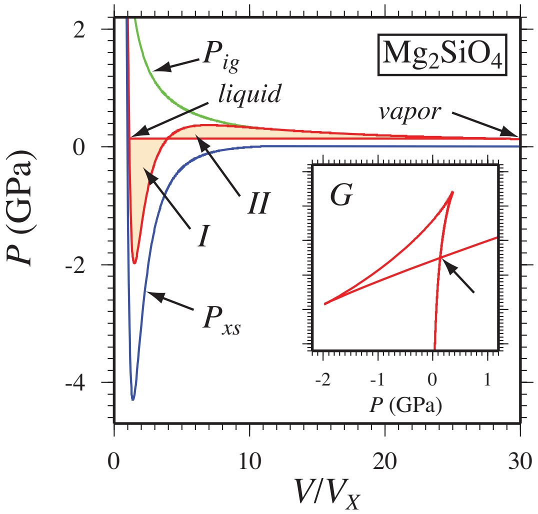

Figure 3.6: Thermodynamics of vaporization in Mg_2SiO_4 liquid. Equation 3.16 also captures the thermodynamics of vaporization, as illustrated by extrapolation of the 3000 K isotherm in Mg_2SiO_4. The pressure of liquid-vapor coexistence (0.13 GPa; horizontal red line) is found from the triplication in G (arrow in inset), or equivalently from the Maxwell equal area construction (area I = area II). The resulting heat of vaporization (1420 kJ/mol) is comparable to the heat of vaporization of forsterite used in giant impact studies (Benz et al., 1989; Canup, 2004).

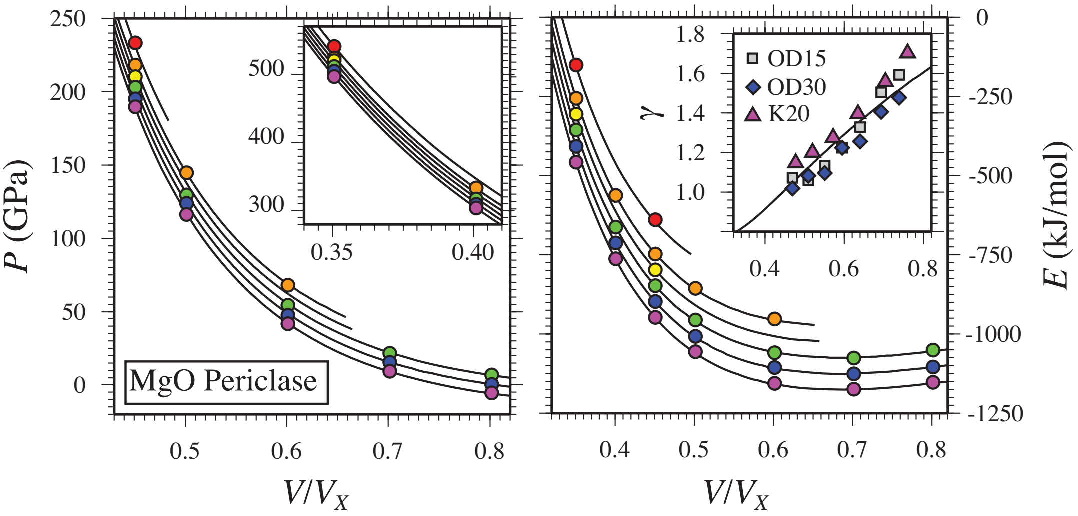

Figure 3.7: Pressure (P) and internal energy (E) of MgO periclase. Colored circles show values from FPMD simulations at 2000 K (purple), 3000 K (blue), 4000 K (green), 5000 K (yellow), 6000 K (orange) and 8000 K (red). Black lines indicate the fit of Equation 3.35, with a fourth order expansion in finite strain required to account for the points at $V/V_X = 0.35$ (left inset). Errorbars are smaller than the size of the symbols. Inset on the right compares Grüneisen parameter (γ) obtained from this fit to previous estimates. Karki et al. (2000a), γ at 2000 K from lattice dynamics (K20); Oganov and Dorogokupets (2003), FPMD at 1500 K (OD15) and 3000 K (OD30).

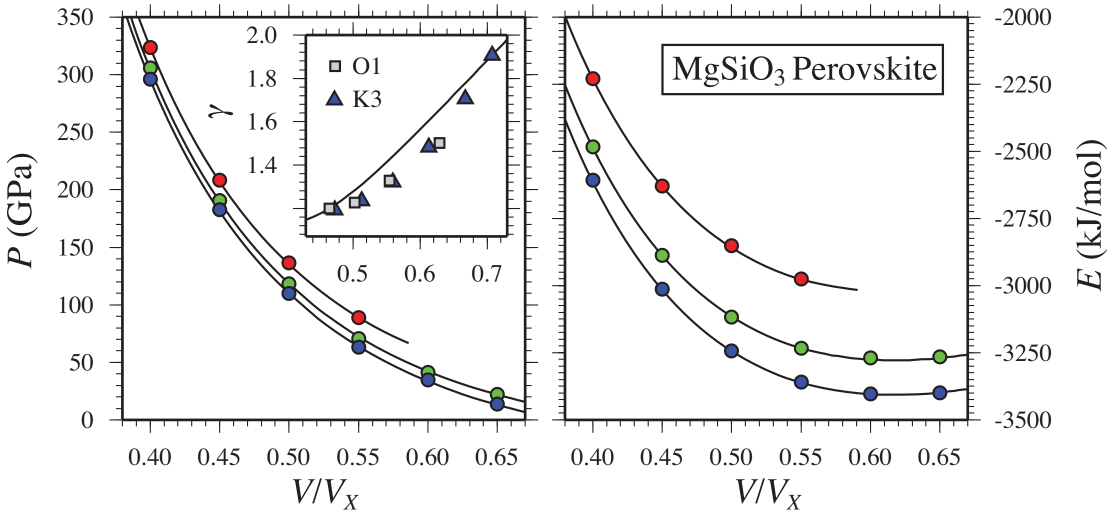

Figure 3.8: Pressure (P) and internal energy (E) of $MgSiO_3$ perovskite. Colored circles show values from FPMD simulations at 3000 K (blue), 4000 K (green) and 6000 K (red). Black lines indicate the fit of Equation 3.35, with a third order expansion in finite strain. Errorbars are smaller than the size of the symbols. Inset compares Grüneisen parameter (γ) obtained from this fit to previous estimates. Karki et al. (2000b), γ at 3000 K from lattice dynamics (K3); Oganov et al. (2001b), FPMD at 1000 K (O1).

Figure 3.9: Shock melting of MgO periclase. (top) FPMD melting curve of periclase with uncertainty given by gray envelope. Previous LDA FPMD calculation of Alfe (2005) (A05; red dotted line), and experimental measurement of Zerr and Boehler (1994) (ZB94) shown for comparison. The solid Hugoniot (green line) crosses the melting curve at 344 GPa, 8880 K, and the liquid Hugoniot crosses at 452 GPa, 9170 K (faint dotted lines). In between these points the equilibrium Hugoniot should follow the melting curve. Metastable Hugoniot sections are shown as broken lines. SA87 - shock temperature measurements of Svendsen and Ahrens (1987). (middle) Pressure-density Hugoniot, compared with measurements of Marsh (1980) (M80), Vassiliou and Ahrens (1981) (VA81), Svendsen and Ahrens (1987) (SA87) and Duffy and Ahrens (1995) (DA95). Complete shock melting is predicted to result in a $\sim 0.12\,\mathrm{g/cm^3}$ density increase along the Hugoniot, even though no density crossover is present along the melting curve. (bottom) Bulk sound velocity (v_B) of the liquid is 2.3 km/s slower than the p-wave velocity (v_P) calculated along the FPMD periclase Hugoniot from experimental data using the model of Stixrude and Lithgow-Bertelloni (2005) (SLB05).

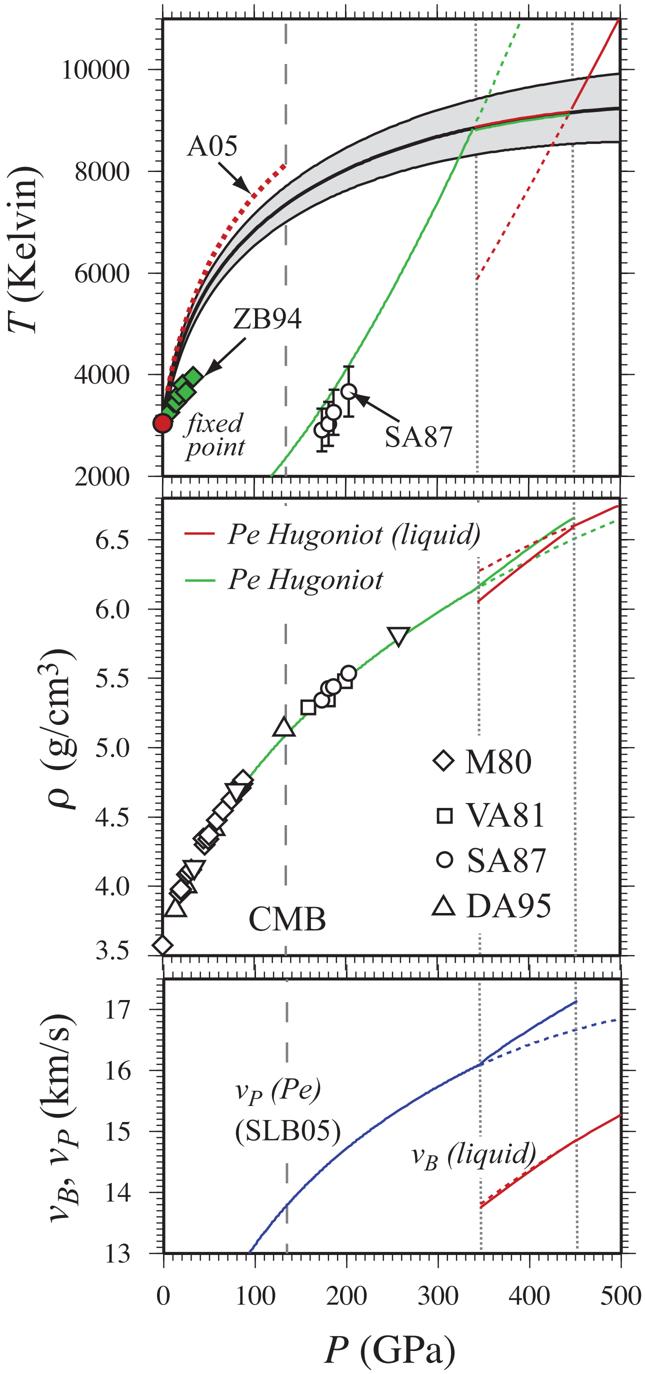
T (Kelvin)
10000
8000
6000
4000
2000
A05
ZB94
fixed point
SA87
ρ (g/cm³)
6.5
6.0
5.5
5.0
4.5
4.0
3.5
Pe Hugoniot (liquid)
Pe Hugoniot
◇ M80
□ VA81
○ SA87
△ DA95
CMB
v_B, v_P (km/s)
17
16
15
14
13
v_P (Pe)
(SLB05)
v_B (liquid)
0
100
200
300
400
500
P (GPa)

Figure 3.10: Shock melting of $MgSiO_3$ perovskite. (top) FPMD melting curve of perovskite with uncertainty given by gray envelope. Result of Stixrude and Karki (2005) (SK05; red dotted line), and experimental measurements of Heinz and Jeanloz (1987) (HJ), Knittle and Jeanloz (1989) (KJ), Sweeney and Heinz (1998) (SH), Zerr and Boehler (1993) (ZB93), and Shen and Lazor (1995) (SL95) shown for comparison. The solid Hugoniot (green line) is almost identical to that calculated from experimental data (Stixrude and Lithgow-Bertelloni, 2005), and crosses the melting curve at 155 GPa, 5520 K, with the liquid Hugoniot crossing at 242 GPa, 6290 K (faint dotted lines). In between these points the equilibrium Hugoniot should follow the melting curve. Metastable Hugoniot sections are shown as broken lines. L04 - shock temperature measurements of Luo et al. (2004). (middle) Pressure-density Hugoniot, compared with measurements of Akins et al. (2004) (A04), and Luo et al. (2004) (L04). Complete shock melting is predicted to result in a $\sim 0.1\,\mathrm{g/cm^3}$ density increase along the Hugoniot, even though no density crossover is present along the melting curve. (bottom) Bulk sound velocity (v_B) of the liquid is 2.6 km/s slower than the p-wave velocity (v_P) calculated along the FPMD perovskite Hugoniot from experimental data using the model of Stixrude and Lithgow-Bertelloni (2005) (SLB05).

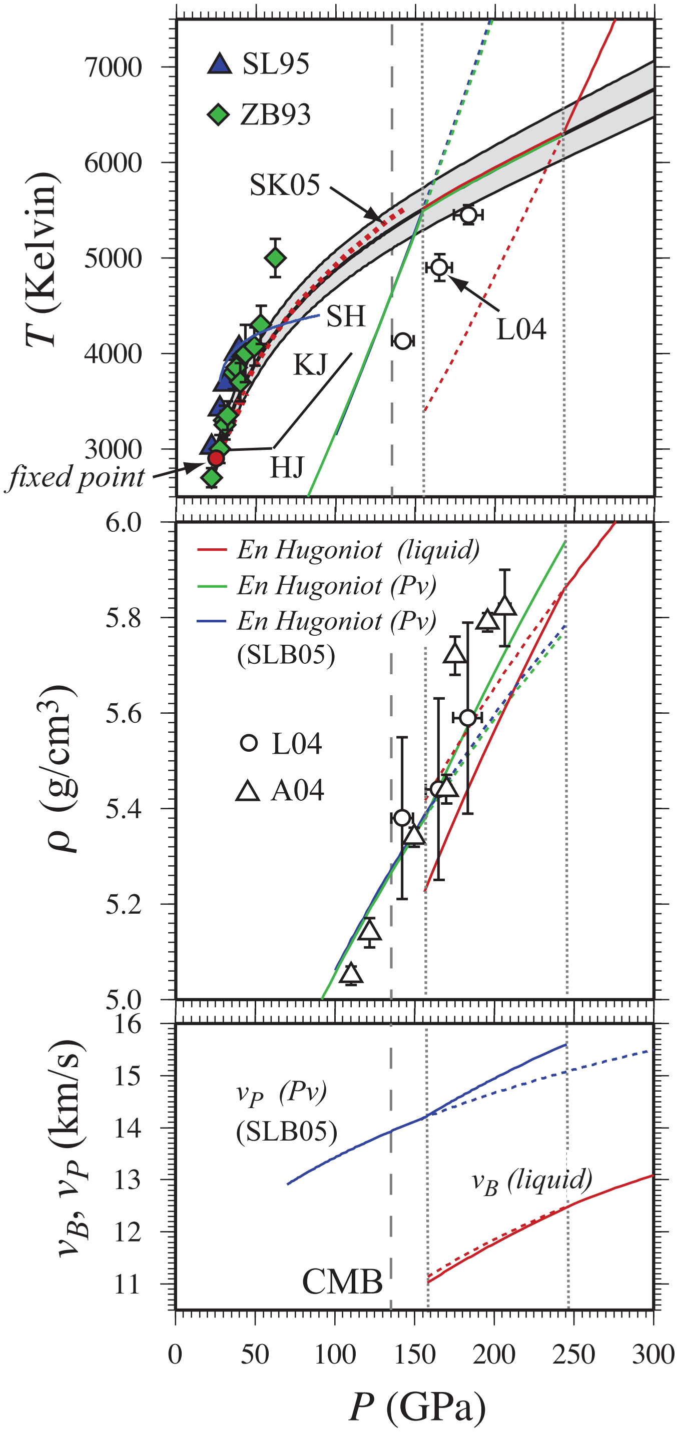
SL95
ZB93
SK05
SH
KJ
HJ
L04
fixed point
T (Kelvin)
3000
4000
5000
6000
7000
En Hugoniot (liquid)
En Hugoniot (Pv)
En Hugoniot (Pv)
(SLB05)
L04
A04
ρ (g/cm^3)
5.0
5.2
5.4
5.6
5.8
6.0
v_P (Pv)
(SLB05)
v_B (liquid)
CMB
v_B, v_P (km/s)
11
12
13
14
15
16
0
50
100
150
200
250
300
P (GPa)

CHAPTER IV

Structure and Mixing of Liquids on the $\mathrm{MgO-SiO_2}$ Join and the Origin of Liquid Immiscibility

4.1 Abstract

The properties of silicate melts in Earth's deep interior are key to our understanding of its thermal and chemical evolution. Using results from first principles molecular dynamics of six intermediate liquid compositions along the MgO-SiO_2 join, we investigate the compositional and pressure dependence of liquid state thermodynamics and structure. At low pressure the enthalpy of mixing is notably pressure dependent, primarily due to the disappearance with pressure of a maximum at high silica compositions. Experimentally observed liquid immiscibility is a direct consequence of this maximum. We identify the underlying contrasts in liquid structure between pure SiO_2 and intermediate composition liquids as the mechanism responsible for liquid immiscibility, and illustrate its expression in other liquid properties such as the Grüneisen parameter, isochoric heat capacity and compressibility. We further find that the enthalpy of mixing is described by a two-parameter asymmetric Margules solution model with pressure dependent interaction parameters.

4.2 Manuscript

It is widely recognized that the Earth was likely entirely molten during the late stages of accretion (Urey, 1955; Tonks and Melosh, 1993; Ruff and Anderson, 1980; Hanks and Anderson, 1969), and that melt may be present at great depth within current day the mantle (Revenaugh and Sipkin, 1994; Song et al., 1994; Williams and Garnero, 1996; Garnero and Helmberger, 1995). Knowledge of the eutectic composition and temperature of the lower mantle can thus constrain the geotherm and yield insight into the thermal and chemical evolution of the planet. Liquids in the MgO-SiO_2 system account for a major fraction of the composition of a terrestrial magma ocean after core-mantle segregation. Liquid immiscibility is known to exist in this system at ambient pressures (Bowen and Andersen, 1914; Hageman and Oonk, 1986; Dalton and Presnall, 1997), and its potential occurrence at great depth within a magma ocean has notable implications for its chemical evolution. To address these questions, knowledge of the thermodynamics of mixing at lower mantle pressures is required to combine results from experimental and theoretical studies of individual compositions into a universal thermodynamic model of silicate melts. Here, we use results from first principles molecular dynamics (FPMD) simulations of a number of liquid compositions along the MgO-SiO_2 join to investigate thermodynamics of mixing and the compositional dependence of liquid structure to very high pressures.

Our approach has been discussed extensively in previous studies (Stixrude and Karki, 2005; de Koker et al., 2008a,b). Constant NVT FPMD (Nosé, 1984) is performed in the local density approximation (Ceperley and Alder, 1980, LDA) with psuedopotentials (Kresse and Hafner, 1994) and the VASP planewave code (Kresse and Furthmüller, 1996). We combine published simulation results for liquid MgO

(Karki et al., 2006), Mg_2SiO_4 (de Koker et al., 2008a), $MgSiO_3$ (Stixrude and Karki, 2005) and SiO_2 (Karki et al., 2007), with new simulations for intermediate composition liquids, Mg_5SiO_7, $Mg_3Si_2O_7$, $MgSi_2O_5$ and $MgSi_3O_7$. These intermediate systems are initiated by removing and/or transforming an appropriate number of atoms from either $MgSiO_3$ or Mg_2SiO_4 and evolving the resulting high energy configuration to a favorable state at 10000 K for 6000 time steps by FPMD. The empirical pressure correction which accounts for the systematic overbinding in LDA for these compositions is determined by interpolation along the join using the known values for MgO, Mg_2SiO_4, $MgSiO_3$ and SiO_2.

As found previously for Mg_2SiO_4 and $MgSiO_3$, a third order finite strain and second order thermal variable (θ) expansion is required to fit $P(V,T)$ and $E(V,T)$ for the intermediate composition liquids to the liquid state fundamental relation (de Koker et al., 2008b) (Figures B.1 - B.4).

In all compositions $\mathrm{Si-O}$ coordination ($Z_{\mathrm{Si-O}}$) increases from 4 to 6 upon two-fold compression, with this increase notably delayed in pure SiO_2 (Figure 4.1). $Z_{\mathrm{Mg-O}}$ is close to 5 for all systems at $V/V_0 = 1.0$, with a strong compositional trend emerging by $V/V_0 = 0.5$, where $Z_{\mathrm{Mg-O}} = 7$ in MgO and $Z_{\mathrm{Mg-O}} = 7.2$ in Mg_5SiO_7 increases to $Z_{\mathrm{Mg-O}} = 8.8$ in $MgSi_3O_7$. Polymerization, as expressed by $Z_{\mathrm{O-Si}}$, changes strongly as a function of pressure and composition. At 0 GPa and 3000 K, only free ($\mathrm{O_F}$; $Z_{\mathrm{O-Si}} = 0$), non-bridging ($\mathrm{O_N}$; $Z_{\mathrm{O-Si}} = 1$), and bridging oxygen ($\mathrm{O_B}$; $Z_{\mathrm{O-Si}} = 2$) are present. $\mathrm{O_N}$ is present in all mixed compositions, but most abundant at $X_{\mathrm{SiO_2}} = 0.4$. Highly coordinated oxygen species appear upon compression, with $Z_{\mathrm{O-Si}} = 3$, and $Z_{\mathrm{O-Si}} = 4$ dominant in high silica liquids by 136 GPa and 6000 K (Figure 4.2). A larger variety of oxygen species are present at high pressures, with abundances more evenly spread along the join.

The changes in liquid structure with pressure and composition are strongly reflected by the thermodynamic properties. The increase in Grüneisen parameter (γ) with compression is seen for all liquids along the join, albeit delayed in SiO_2, and highlights the relation between γ and $Z_{\mathrm{Si-O}}$ (Figure 4.1). In solids, high pressure phase transitions involving an increase in $Z_{\mathrm{Si-O}}$ result in notable increases in γ, with similar effects predicted for other cations, including Mg^{2+} (Jeanloz and Roufosse, 1982). The increase of γ with MgO content, and its notably weaker volume dependence in MgO suggests that $\mathrm{Mg-O}$ bonds have intrinsically higher γ values, less sensitive to changes in bond length. The decrease in compressibility with compression is delayed in SiO_2 as well (Figure 4.3), while the decrease in K_{T0} values from 24 GPa in Mg_5SiO_7 to 9.9 GPa in $MgSi_3O_7$ is accompanied by an increase in K'_{T0} from 5.88 to 8.24 (Table 4.1), consistent with a more general K_{T0} - K'_{T0} anti-correlation observed in silicate liquids (Lange, 2007).

At 0 GPa and 3000 K, the enthalpy of mixing (H_{mix}) shows a minimum of $-22\,\mathrm{kJ/mol}$ for $Mg_3Si_2O_7$, and positive values at $MgSi_2O_5$ and $MgSi_3O_7$ (Figure 4.4). Extrapolating H_{mix} to the critical miscibility temperature of 2250 K (Hageman and Oonk, 1986), we estimate an entropy of mixing (S_{mix}) of $0.45\,Nk_B$ at $MgSi_3O_7$. Above 7 GPa all H_{mix} values are negative, showing increasingly symmetric compositional dependence. Pressure dependence in H_{mix}

$$\left(\frac{\partial H_{mix}}{\partial P}\right)_T = V_{mix}\left(1 - T\alpha_{mix}\right). \tag{4.1}$$

results in a volume of mixing (V_{mix}), which displays a notably asymmetrical V_{mix} minimum is at low pressure (Figure 4.4).

The contrast in compressional dependence of $Z_{\mathrm{Si-O}}$ between pure SiO_2 and liquid mixtures, also reflected by γ, C_V and K_T, may be understood in terms of differences in the liquid structure and its response to compression. In pure SiO_2, the liquid is completely polymerized, comprising an open framework topology (Karki et al., 2007). Upon compression, this open structure initially adapts through changes in ring statistics (Stixrude and Bukowinski, 1990b; Karki et al., 2007), before coordination increase sets in. These mechanisms are absent in the liquid mixtures, where the framework breaks down in the presence of a high field-strength network modifier (Hess, 1995). The contrast in topology is further responsible for the extremes in H_{mix} and V_{mix} at low pressure. The large density of high silica liquids relative to pure SiO_2 is consistent with the absence of an open framework. This less polymerized structure is not energetically favorable (Kieffer and Angell, 1989), resulting in the maximum in H_{mix}. Such a stability relation, whereby a low density two phase liquid assemblage is more stable than a more dense, single liquid phase can only occur at low pressures. The absence of a maximum in H_{mix} above about 7 GPa is in agreement with the experimental observation of liquid immiscibility disappearing above 5 GPa (Dalton and Presnall, 1997). Deep mantle liquid immiscibility can therefore not arise by this mechanism, consistent with the compositional dependence of H_{mix} at deep mantle pressures.

To model H_{mix} at constant P, we use a two-parameter Margules equation (Thompson Jr., 1967)

$$H_{mix} = W_{\mathrm{SiO_2}} Y_{\mathrm{SiO_2}} (1 - Y_{\mathrm{SiO_2}})^2 + W_{\mathrm{MgO}} (1 - Y_{\mathrm{SiO_2}}) Y_{\mathrm{SiO_2}}^2, \tag{4.2}$$

$$Y_{\mathrm{SiO_2}} = \frac{X_{\mathrm{SiO_2}}}{\lambda + X_{\mathrm{SiO_2}}(1-\lambda)}, \tag{4.3}$$

where $W_{\mathrm{SiO_2}}$ and W_{MgO} are interaction parameters, and λ is a endmember scaling parameter. For example $\lambda = 3/2$ changes the endmembers to Mg_2O_2 and Si_3O_6. Interaction parameters and the required endmember scaling change notably with pressure (Table 4.2). We thus find that the commonly applied assumption of

$(\partial H_{mix}/\partial P)_T = 0$ and $V_{mix} = 0$ is insufficient for the MgO-SiO_2 system. Although this assumption has been applied with great success to modeling experimental data for silicate liquids at low pressure (Stebbins et al., 1984; Lange and Carmichael, 1987; Ghiorso and Sack, 1995; Ghiorso et al., 2002; Ai and Lange, 2008), and has also been shown to hold for a liquid mixture with $CaAl_2Si_2O_8$ and $CaMgSi_2O_6$ as endmembers at pressures up to 25 GPa (Rigden et al., 1989), these studies focus on only a small section of compositional space, and are therefore unable to capture the rich thermodynamic behavior that our results reveal. Our results serve as a reminder that extrapolating these models outside the compositional range within which they are parameterized must be done with caution, especially in the case of endmembers for which liquid immiscibility is known to occur.

4.3 Acknowledgements

This research was supported by the National Science Foundation under Grants EAR-0409074 and EAR-0409121. Computing facilities were provided by CCT at Louisiana State University and by CAC at the University of Michgan.

Table 4.1: Thermodynamic properties of mixed liquids on the MgO-SiO_2 join at 0 GPa, 3000 K

	MgO	Mg_5SiO_7	Mg_2SiO_4	$Mg_3Si_2O_7$	$MgSiO_3$	$MgSi_2O_5$	$MgSi_3O_7$	SiO_2
$\rho\,(\mathrm{g/cm^3})$	2.45	2.45	2.41	2.40	2.40	2.42	2.40	2.18
$K_T\,(\mathrm{GPa})$	33.2 (2)	24 (1)	17.7 (7)	16.5 (5)	15.2 (5)	12.3 (6)	12.1 (6)	8.3 (43)
$K_S\,(\mathrm{GPa})$	43.1 (8)	32 (1)	19.2 (7)	17.7 (6)	16.8 (6)	13.2 (6)	12.4 (6)	8.9 (45)
K_T'	4.81	5.88	6.34	6.37	6.71	7.62	6.70	6.5
$\alpha\,(10^{-}6\,\mathrm{K}^{-1})$	103 (1)	134 (3)	82 (3)	77 (4)	97 (3)	96 (4)	49 (11)	129 (9)
$C_V\,Nk_B$	3.5 (5)	3.8 (3)	4.1 (6)	4.3 (7)	4.3 (3)	4.7 (4)	4.3 (7)	5.4 (6)
$C_P\,Nk_B$	4.6 (9)	5.1 (6)	4.5 (6)	4.6 (7)	4.7 (3)	5.1 (4)	4.4 (7)	5.9 (9)
γ	0.97 (3)	0.82 (2)	0.35 (2)	0.30 (2)	0.35 (2)	0.25 (2)	0.14 (1)	0.22 (4)

Table 4.2: Interaction parameters for H_{mix} obtained from fit of Equation 4.2

	0 GPa	5 GPa	10 GPa	25 GPa	60 GPa	100 GPa
W_{MgO} (kJ/mol)	175	140	10	-140	-140	-130
$W_{\mathrm{SiO_2}}$ (kJ/mol)	-210	-240	-235	-240	-225	-210
λ	3/2	3/2	5/4	1	1	1

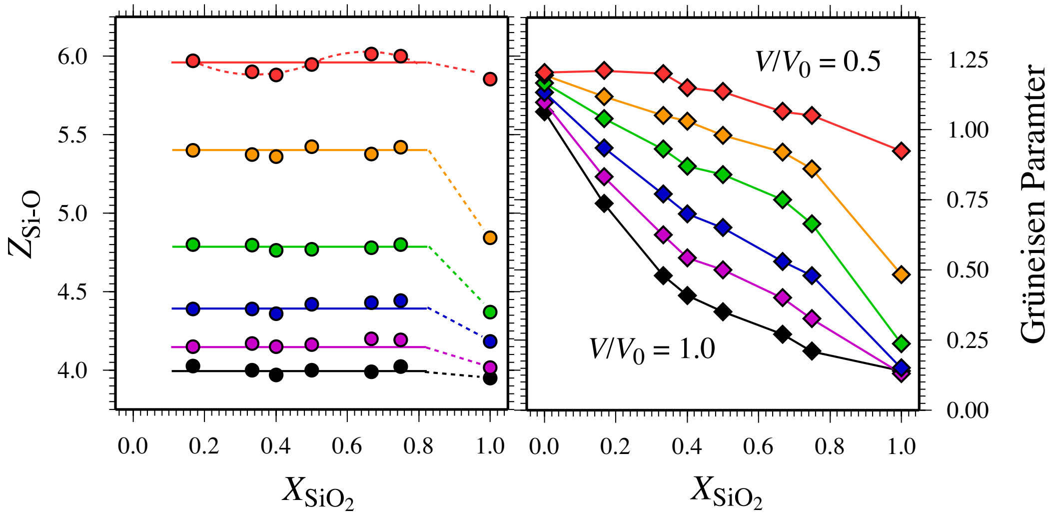

Figure 4.1: Silicon ($Z_{\text{Si-O}}$) coordination and Grüneisen parameter (γ) along the MgO-SiO$_2$ join. (left) ($Z_{\text{Si-O}}$) increases from 4 to 6 upon two fold compression along the whole join, with the increase notably delayed in SiO$_2$. (right) γ at 4000 K for all liquids on the join increases with compression and MgO content. The delay in its increase for SiO$_2$ reflects the delayed increase in Z_{Si-O}. V_0 is the volume at zero pressure as determined from fitting the equation of state.

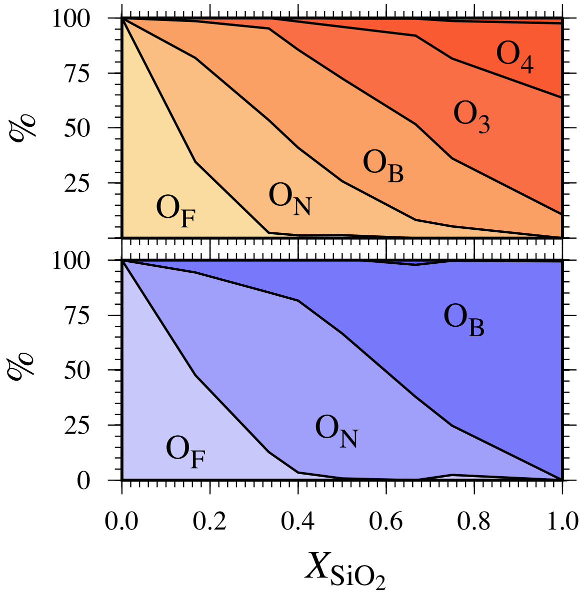

Figure 4.2: The distribution of oxygen species at 6000 K and 136 GPa (top), and 3000 K and 0 GPa (bottom). O_F - $Z_{O-Si} = 0$, O_V - $Z_{O-Si} = 1$, O_B - $Z_{O-Si} = 2$, O_3 - $Z_{O-Si} = 3$, O_4 - $Z_{O-Si} = 4$.

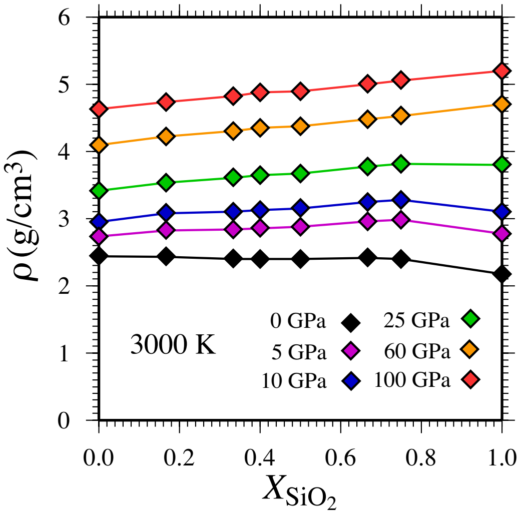

Figure 4.3: Liquid density along the MgO-SiO$_2$ join. Note the greater compressibility of high SiO$_2$ mixtures, with the compressibility of pure SiO$_2$ markedly higher.

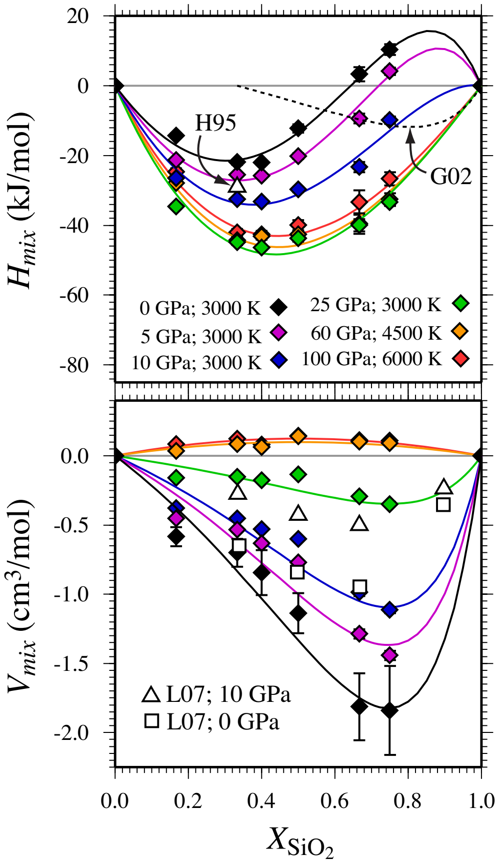

Figure 4.4: Enthalpy and volume of mixing along the MgO-SiO$_2$ join. (top) Enthalpy of mixing (H_{mix}) is notably asymmetrical at low pressures, becoming more symmetrical and less pressure dependent at higher pressures. Lines indicate fits obtained using Equation 4.2, interaction parameters for which is given in Table 4.2. The 0 GPa minimum agrees well with the value estimated by Hess (1995) by combining solid enthalpies of mixing and of fusion (H95). The low pressure maximum and its absence above 7 GPa is qualitatively similar to the finding in a empirical potential study (Wasserman et al., 1993). The poor agreement with the prediction of Ghiorso et al. (2002) (G02) highlights the pitfalls of extrapolating their model to the pure MgO-SiO$_2$ binary. (bottom) The large pressure dependence in H_{mix} results in a large volume of mixing (V_{mix}) at low pressures. The minimum coincides with the decreasing maximum in H_{mix}, reflecting the absence of the open framework topology of pure SiO$_2$ liquid in the presence of a high field-strength network modifier (see text). White symbols are results obtained by Lacks et al. (2007) using empirical potentials (L07).

CHAPTER V

Conclusion

Two recurring conclusions emerge in the work presented here. The first is that liquid structure, and its ability to change readily with compression, has a profound influence on the macroscopic thermodynamic properties of the liquid. This is exemplified in the origin of an isochemical density crossover along the melting curve of forsterite (Chapter II), and of liquid immiscibility at low pressures, expressed in the thermodynamics of mixing (Chapter IV). Properties and trends that distinguish silicate liquids of varying composition from each other, and especially from the crystalline polymorphs, such as the increasing Grüneisen parameter, high compressibility and high K'_{T0} values, are all the direct expression of liquid structure and its response to compression.

Because liquid structure depends directly on bonding, obtaining the correct liquid structure requires the valence electronic structure to be accurately described. Indeed, the second recurring conclusion is that describing the system directly in terms of the charge density invariably gives superior results to that obtained by empirical potential atomistic simulation techniques. Results are accurate over a very large pressure range, and information about the valence electronic structure and its contribution to the free energy are computed self consistently. This is especially important in liquids since, as we have shown in Chapter III, the thermal electronic free energy contribution is not negligible at high temperatures.

Although we have illustrated the significant utility of first principles molecular dynamics (FPMD), one should not lose sight of the fact that the various theoretical components of our implementation, notably the local density approximation (LDA), the Γ-point only Brillouin zone sampling, and the use of a periodic boundary condition, are not without shortcomings. In calculating the equation of state and transport properties, we corrected for these factors by estimating their likely effects. The validity of these corrections remains to be tested by future studies as larger computational resources and superior theoretical techniques become available.

In the introduction (Chapter I) we speculated regarding the presence of liquid immiscibility and density crossovers within the deep mantle. We have subsequently shown that liquid immiscibility is absent at pressures above about 7 GPa, and that the structural mechanism responsible is only favorable at low pressure. We further found that while Mg_2SiO_4 forsterite shows a density crossover, neither MgO periclase, nor $MgSiO_3$ perovskite melts to form a denser liquid, despite the continued increase in cation coordination shown to be responsible for the density crossover in forsterite. Therefore, if perovskite is the liquidus phase within a crystallizing magma ocean, it will sink to depths where it may be re-assimilated, diminishing chemical differentiation and prolonging the crystallization time scale.

We have also shown the increasing trend in the Grüneisen parameter (γ) to hold for all liquids along the join. From the definition of the Grüneisen parameter and Maxwell relations follow that

$$\left(\frac{\partial \ln T}{\partial \ln \rho}\right)_S = \gamma \frac{T}{\rho}. \tag{5.1}$$

Therefore, given the density profile of a magma ocean, the adiabat found for γ increasing with density will be steeper than that found where γ decreases. An increasing γ thus places existing estimates of the adiabatic profile within a magma ocean under renewed scrutiny, since these estimates assume γ to decrease with compression (Miller et al., 1991b).

Because the melting temperatures of liquids that contain Fe, Ca, Al and H_2O will be lower than those of the MgO-SiO_2 system, our respective melting curves serve as upper bounds for the melting temperatures of Fe-bearing olivine, perovskite and ferropericlase, as well as for the mantle solidus. Given these estimates, should we expect melt to be present at depth within the mantle? Our metastable congruent melting temperature for forsterite at the experimental forsterite-wadsleyite transformation (2540 ± 60 K) is well above the estimated mantle temperature at the 410 km discontinuity (1800 K; Stixrude and Lithgow-Bertelloni (2007)). The eutectic melting temperature of a garnet-peridotite mantle composition will therefore need to be around 740 K lower to account for seismic observations. This difference is rather high (Zhou and Miller, 1997; Presnall et al., 1998), even with a mantle geotherm increase of $100 - 150$ K associated with an upwelling plume, and additional factors, such as water are needed for melting atop the 410 km discontinuity. Similarly, the melting temperature of perovskite at the core-mantle boundary (5320 ± 210 km) is well above estimates of the adiabatic temperature profile of the mantle at that depth ($2400 - 3100$ K, Stixrude and Lithgow-Bertelloni (2007); Boehler (1996); Jeanloz and Morris (1986)). Adjusting the melting temperature by $800 - 1300$ K (Zhou and Miller, 1997) to account for freezing point depression and the effect due to additional major elements is therefore not sufficient for melt to be present. However, melting at the core-mantle boundary can occur if the geothermal profile within the thermal boundary layer crosses the solidus. This is not unlikely, given the general estimates of the melting temperature of Fe at this depth (4800 ± 200 K, Williams et al. (1991)), and is consistent with the observation that the ultra-low velocity zone is limited to the very base of the D".

Clearly a number of questions remain. We were able to compute congruent melting curves for forsterite, perovskite and periclase, but can only approximate the effect of incongruent melting. Accurate description of incongruent melting requires knowledge of the chemical potential, for which both the enthalpy and entropy of mixing must be known along the full extent of the join. We have shown that the liquid structure comprises a number of $\mathrm{Si-O}$ coordination states, so that simple configurational models for estimating the entropy of mixing (Hess, 1995; Charles, 1969) are not sufficiently accurate to describe phase equilibria.

In relating our calculated melting curves to the mantle and its chemical composition, we make estimates of the potential effect of other major elements in the mantle, notably Fe, Ca and Al. These estimates are based on systematics and simple thermodynamic arguments, and can only be accurately quantified through simulations that include these elements. Due to the large number of valence electrons which must be treated, FPMD simulations of Fe-bearing liquids require significantly more computational resources, but it is certainly within reach. Studies of Ca-bearing, as well hydrous liquids are under way (Sun, 2008; Mookherjee et al., 2008).

APPENDICES

APPENDIX A

F_{xs} coefficients

The excess free energy contribution to the liquid state fundamental relation is given by

$$F_{xs}(V,T) = \sum_{i=0} \sum_{j=0} \frac{a_{ij}}{i!j!} f^i \theta^j, \tag{A.1}$$

$$f = \frac{1}{n}\left[\left(\frac{V_0}{V}\right)^{\frac{n}{3}} - 1\right], \tag{A.2}$$

$$\theta = \left[\left(\frac{T}{T_0}\right)^{m} - 1\right]. \tag{A.3}$$

By the assumption that the individual free energy contributions can be separated, any excess thermodynamic property (A_{xs}) which is a direct free energy derivative (instead of following from reduction of derivatives) is obtained from the total value (A) by removing the ideal gas and electronic terms

$$A_{xs} = A - A_{ig} - A_{el}. \tag{A.4}$$

The coefficients of the excess free energy expansion (a_{ij}) are directly related to the excess thermodynamic properties of the liquid at reference volume (V_0) and temperature (T_0), and follow from taking the appropriate derivatives and substituting f_0 and θ_0. These relations are

$$a_{00} = F_{xs0}, \tag{A.5}$$

$$a_{10} = 3V_0 P_{xs0}, \tag{A.6}$$

$$a_{01} = -\frac{1}{m} T_0 S_{xs0}, \tag{A.7}$$

$$a_{20} = 9V_0 K_{Txs0} - 3(n+3) V_0 P_{xs0}, \tag{A.8}$$

$$a_{11} = \frac{3}{m} V_0 T_0 \alpha K_{Txs0}, \tag{A.9}$$

$$a_{02} = -\frac{1}{m^2} T_0 C_{Vxs0} + \frac{m-1}{m^2} T_0 S_{xs0}, \tag{A.10}$$

$$a_{30} = 27 V_0 K_{Txs0} (K'_{Txs0} - (n+2)) + 3(n+3)(2n+3) V_0 P_{xs0}, \tag{A.11}$$

$$a_{21} = -\frac{9}{m} V_0^2 T_0 \left(\frac{\partial \alpha K_T}{\partial V} \right)_{Txs0} - -\frac{3(n+3)}{m} V_0 T_0 \alpha K_{Txs0}, \tag{A.12}$$

$$a_{12} = \frac{3}{m^2} V_0 T_0^2 \left(\frac{\partial \alpha K_T}{\partial T} \right)_{Vxs0} - \frac{3(m-1)}{m^2} V_0 T_0 \alpha K_{Txs0}, \tag{A.13}$$

$$a_{03} = \frac{(3m-2)}{m^3} T_0 C_{Vxs0} - \frac{1}{m^3} T_0^2 \left(\frac{\partial C_V}{\partial T} \right)_{Vxs0} - \frac{(m-1)(2m-1)}{m^3} T_0 S_{xs0}, \tag{A.14}$$

$$\begin{aligned} a_{40} = {} & 81 V_0^3 \left(\frac{\partial^2 K_T}{\partial V^2} \right)_{Txs0} + 162(n+2) V_0^2 \left(\frac{\partial K_T}{\partial V} \right)_{Txs0} \\ & + 9V_0 (11n^2 + 36n + 27) K_{xs0} - 3V_0 (n+3)(6n^2 + 15n + 9) P_{xs0}, \end{aligned} \tag{A.15}$$

$$\begin{aligned} a_{31} = {} & \frac{27}{m} V_0^3 T_0 \left(\frac{\partial^2 \alpha K_T}{\partial V^2} \right)_{Txs0} + \frac{27(n+3)}{m} V_0^2 T_0 \left(\frac{\partial \alpha K_T}{\partial V} \right)_{Txs0} \\ & - \frac{3(n+3)(2n+3)}{m} V_0 T_0 \alpha K_{Txs0}, \end{aligned} \tag{A.16}$$

$$\begin{aligned} a_{22} = & \frac{-9}{m^2}V_0^2T_0\left(\frac{\partial^2 C_V}{\partial V^2}\right)_{Txs0} - \frac{3(n+3)}{m^2}V_0T_0\left(\frac{\partial C_V}{\partial V}\right)_{Txs0} \\ & + \frac{9(m-1)}{m^2}V_0^2T_0\left(\frac{\partial \alpha K_T}{\partial V}\right)_{Txs0} + \frac{3(n+3)(m-1)}{m^2}V_0T_0\alpha K_{Txs0}, \end{aligned} \tag{A.17}$$

$$\begin{aligned} a_{13} = & \frac{3}{m^3}V_0T_0^3\left(\frac{\partial^2 \alpha K_T}{\partial T^2}\right)_{Vxs0} - \frac{9(m-1)}{m^3}V_0T_0^2\left(\frac{\partial \alpha K_T}{\partial T}\right)_{Vxs0} \\ & + \frac{3(m-1)(2m-1)}{m^3}V_0T_0\alpha K_{Txs0}, \end{aligned} \tag{A.18}$$

$$\begin{aligned} a_{04} = & \frac{-1}{m^4}T_0^3\left(\frac{\partial^2 C_V}{\partial T^2}\right)_{Vxs0} + \frac{2(3m-2)}{m^4}T_0^2\left(\frac{\partial C_V}{\partial T}\right)_{Vxs0} \\ & - \frac{(11m^2-12m+3)}{m^4}T_0C_{Vxs0} - \frac{(m-1)(6m^2-5m+1)}{m^4}T_0S_{xs0}. \end{aligned} \tag{A.19}$$

APPENDIX B

Equations of state for intermediate composition liquids

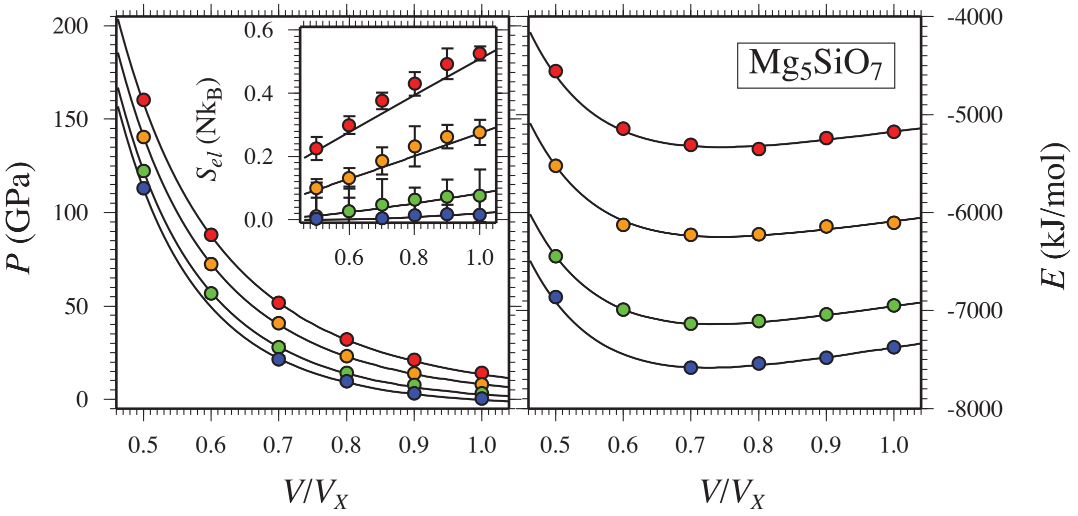

Figure B.1: Pressure (P), internal energy (E) and thermal electronic entropy (S_{el}) of Mg_5SiO_7 liquid. Coloured circles show values from FPMD simulations at 3000 K (blue), 4000 K (green), 6000 K (orange) and 8000 K (red). Black lines indicate the fit of P and E to Equation 3.16 with $\mathcal{O}_\theta = 2$ and a third order expansion in finite strain. Errorbars are smaller than the size of the symbols. Inset shows electronic entropy (S_{el}), with black lines indicating the fit to Equation 3.30.

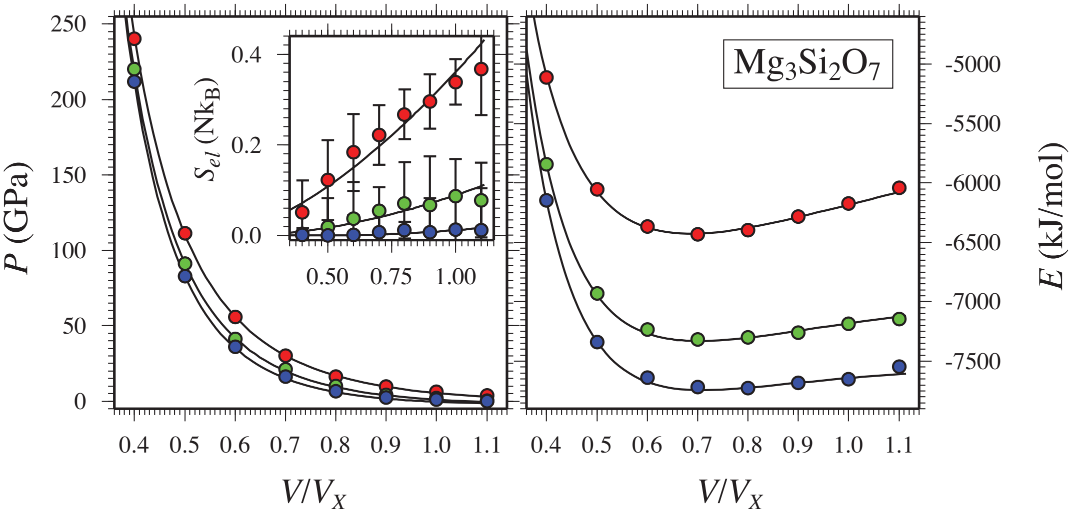

Figure B.2: Pressure (P), internal energy (E) and thermal electronic entropy (S_{el}) of $Mg_3Si_2O_7$ liquid. Coloured circles show values from FPMD simulations at 3000 K (blue), 4000 K (green) and 6000 K (red). Black lines indicate the fit of P and E to Equation 3.16 with $\mathcal{O}_\theta = 2$ and a third order expansion in finite strain. Errorbars are smaller than the size of the symbols. Inset shows electronic entropy (S_{el}), with black lines indicating the fit to Equation 3.30.

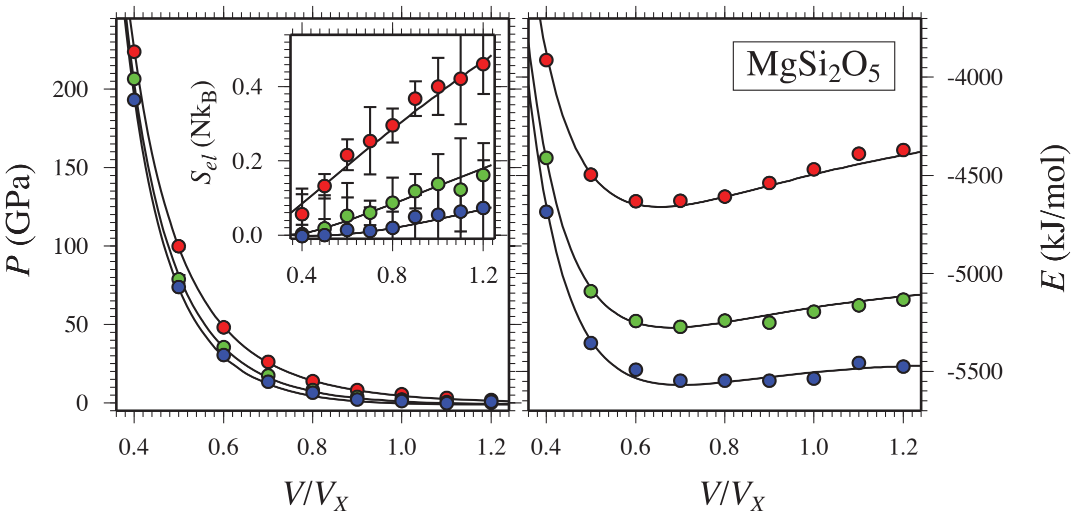

Figure B.3: Pressure (P), internal energy (E) and thermal electronic entropy (S_{el}) of $MgSi_2O_5$ liquid. Coloured circles show values from FPMD simulations at 3000 K (blue), 4000 K (green) and 6000 K (red). Black lines indicate the fit of P and E to Equation 3.16 with $\mathcal{O}_\theta = 2$ and a third order expansion in finite strain. Errorbars are smaller than the size of the symbols. Inset shows electronic entropy (S_{el}), with black lines indicating the fit to Equation 3.30.

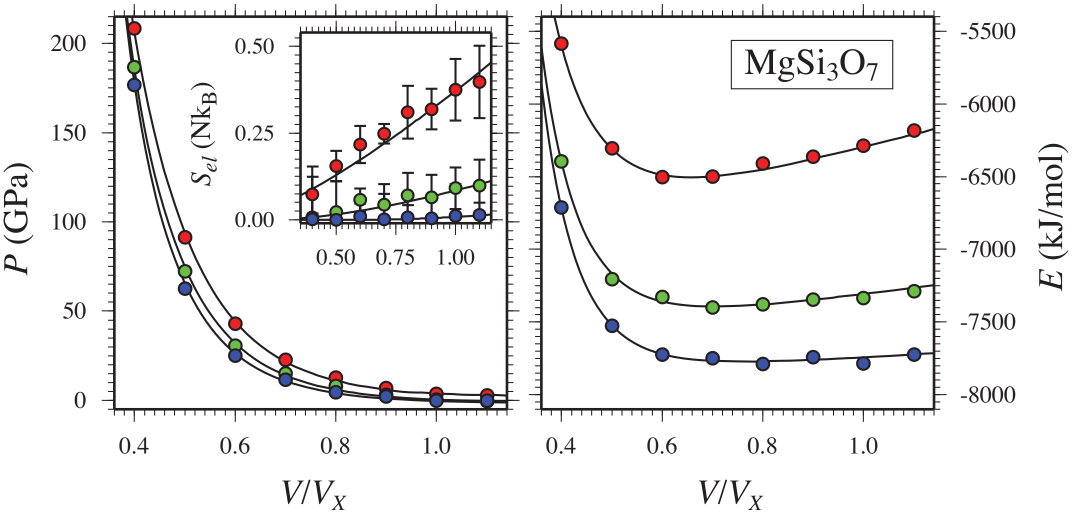

Figure B.4: Pressure (P), internal energy (E) and thermal electronic entropy (S_{el}) of $MgSi_3O_7$ liquid. Coloured circles show values from FPMD simulations at 3000 K (blue), 4000 K (green) and 6000 K (red). Black lines indicate the fit of P and E to Equation 3.16 with $\mathcal{O}_\theta = 2$ and a third order expansion in finite strain. Errorbars are smaller than the size of the symbols. Inset shows electronic entropy (S_{el}), with black lines indicating the fit to Equation 3.30.

BIBLIOGRAPHY

C. B. Agee and D. Walker. Static compression and olivine flotation in ultrabasic silicate liquid. Journal of Geophysical Research, 93:3437–3449, 1988.

C. B. Agee and D. Walker. Olivine flotation in mantle melt. Earth and Planetary Science Letters, 114:315–324, 1993.

Y. Ai and R. A. Lange. The compressibility of CaO-MgO-Al_2O_3-SiO_2 liquids from new acoustic velocity measurements: Reevaluation of the equation of state of $CaMgSi_2O_6$-$CaAl_2SiO_8$ liquids to 25 GPa. Journal of Geophysical Research, in press, 2008.

M. Akaogi, E. Ito, and A. Navrotsky. Olivine-modified spinel-spinel transitions in the system Mg_2SiO_4-Fe_2SiO_4 - calorimetric measurements, thermochemical calculation, and geophysical application. Journal of Geophysical Research, 94(B11): 15671–15685, 1989.

J. A. Akins, S. N. Luo, P. D. Asimow, and T. J. Ahrens. Shock-induced melting of $MgSiO_3$ perovskite and implications for melts in Earth's lowermost mantle. Geophysical Research Letters, 31:L14612, 2004.

D. Alfe. Melting curve of MgO from first-principles simulations. Physical Review Letters, 94:235701, 2005.

M. P. Allen and D. J. Tildesley. Computer Simulation of Liquids. Oxford University Press, Oxford, 1st edition, 1987.

J. R. Allwardt, J. F. Stebbins, H. Terasaki, L. S. Du, D. J. Frost, A. C. Withers, M. M. Hirschmann, A. Suzuki, and E. Ohtani. Effect of structural transitions on properties of high-pressure silicate melts: ^{27}Al NMR, glass densities, and melt viscosities. American Mineralogist, 92:1093–1104, 2007.

C. A. Angell. Formation of glasses from liquids and biopolymers. Science, 267(5206): 1924–1935, 1995.

C. A. Angell, P. A. Cheeseman, and S. Tamaddon. Pressure enhancement of ion mobilities in liquid silicates from computer-simulation studies to 800 Kilobars. Science, 218:885–887, 1982.

P. D. Asimow, M. M. Hirschmann, M. S. Ghiorso, M. J. O'Hara, and E. M. Stolper. The effect of pressure-induced solid-solid transitions on decompression melting of the mantle. Geochimica et Cosmochimica Acta, 59(21):4489–4506, 1995.

J. F. Bacon, A. A. Hasapis, and J. W. Wholley. Viscosity and density of molten silica and high silica content glasses. Physics and Chemistry of Glasses, 1:90–98, 1960.

A. B. Belonoshko and L. S. Dubrovinsky. Molecular dynamics of NaCl (B1 and B2) and MgO (B1) melting: Two-phase simulation. American Mineralogist, 81: 303–316, 1996.

A. B. Belonoshko and S. K. Saxena. A unified equation of state for fluids of C-H-O-N-S-Ar composition and their mixtures up to very high temperatures and pressures. Geochimica et Cosmochimica Acta, 56:3611–3626, 1992.

W. Benz, A. G. W. Cameron, and H. J. Melosh. The origin of the moon and the single-impact hypothesis iii. Icarus, 81:113–131, 1989.

F. Birch. Elasticity and constitution of the Earth's interior. Journal of Geophysical Research, 57(2):227–286, 1952.

F. Birch. Finite strain isotherm and velocities for single-crystal and polycrystalline NaCl at high pressures and 300 K. Journal of Geophysical Research, 83(B3):1257–1268, 1978.

J. O. Bockris, J. A. Kitchener, and S. Ignatowicz. The electrical conductivity of silicate melts - systems containing Ca, Mn and Al. Discussions of the Faraday Society, pages 265–281, 1948.

R. Boehler. Melting temperature of the earth's mantle and core: Earth's thermal structure. Annual Reviews of Earth and Planetary Sciences, 24:15–40, 1996.

R. Boehler and G. C. Kennedy. Pressure-dependence of thermodynamical Grüneisen parameter of fluids. Journal of Applied Physics, 48:4183–4186, 1977.

Y. Bottinga. On the isothermal compressibility of silicate liquids at high-pressure. Earth and Planetary Science Letters, 74:350–360, 1985.

Y. Bottinga and D. F. Weill. Viscosity of magmatic silicate liquids - model for calculation. American Journal of Science, 272(5):438–475, 1972.

N. L. Bowen and O. Andersen. The binary system $MgO - SiO_2$. American Journal of Science, 37:487–500, 1914.

F. R. Boyd, J. L. England, and B. T. C. Davis. Effects of pressure on the melting and polymorphism of enstatite, $MgSiO_3$. Journal of Geophysical Research, 69(10):2101–2109, 1964.

R. Boyle. New Experiments Physico-Mechanical, touching the Spring and Weight of the Air, and its Effects. Oxford, 1662.

J. Brodholt. The melting curve of $MgSiO_3$ perovskite from ab initio molecular dynamics using the coexistience method. 2008 APS March Meeting, New Orleans, LA, page Abstract: J40.00001, 2008.

J. Brodholt and B. Wood. Simulations of the structure and thermodynamic propreties of water at high pressures and temperatures. Journal of Geophysical Research, 98(B1):519–536, 1993.

J. M. Brown, M. D. Furnish, and D. A. Boness. Sound velocities for San Carlos olivine. In S. C. Schmidt and N. C. Holmes, editors, Shock Waves in Condensed Matter. Elsevier, Amsterdam, 1987a.

J. M. Brown, M. D. Furnish, and R. G. McQueen. Thermodynamics for $(\mathrm{Mg,Fe})_2\mathrm{SiO}_4$ from the Hugoniot. In M. H. Manghnani and Y. Syono, editors, High-Pressure Research in Mineral Physics. American Geophysical Union, Washington, D.C., 1987b.

H. B. Callen. Thermodynamics and an Introduction to Thermostatistics. John Wiley and Sons, New York, 2nd edition, 1985.

R. M. Canup. Simulations of a late lunar-forming impact. Icarus, 168:433–456, 2004.

D. M. Ceperley and B. J. Alder. Ground-state of the electron-gas by a stochastic method. Physical Review Letters, 45:566–569, 1980.

S. Chandrasekhar. An Introduction to the Study of Stellar Structure. University of Chicago Press, Chicago, 1939.

R. J. Charles. The origin of immiscibility in silicate solutions. Physics and Chemistry of Glasses, 10(5):169–178, 1969.

C. H. Chen and D. C. Presnall. The system $\mathrm{Mg_2SiO_4}$-$\mathrm{SiO_2}$ at pressures up to 25 kilobars. American Mineralogist, 60:398–406, 1975.

G. Q. Chen, T. J. Ahrens, and E. M. Stolper. Shock-wave equation of state of molten and solid fayalite. Physics of the Earth and Planetery Interiors, 134:35–52, 2002.

B. P. E. Clapeyron. Mémoire sur la puissance motrice de la chaleur. Journal de l'ecole polytechnique Paris, 14:153–190, 1834.

R. E. Cohen and Z. Gong. Melting and melt structure of MgO at high pressures. Physical Review B, 50(17):12301–12311, 1994.

K. D. Collerson, S. Hapugoda, B. S. Kamber, and Q. Williams. Rocks from the mantle transition zone: Majorite-bearing xenoliths from malaita, southwest pacific. Science, 288:1215–1223, 2000.

T. F. Cooney and S. K. Sharma. Structure of glasses in the systems Mg_2SiO_4-Fe_2SiO_4, Mn_2SiO_4-Fe_2SiO_4, Mg_2SiO_4-$CaMgSiO_4$, and Mn_2SiO_4-$CaMnSiO_4$. Journal of Non-Crystalline Solids, 122:10–32, 1990.

P. Courtial, E. Ohtani, and D. B. Dingwell. High-temperature densities of some mantle melts. Geochimica et Cosmochimica Acta, 61(15):3111–3119, 1997.

J. A. Dalton and D. C. Presnall. No liquid immiscibility in the system $MgSiO_3$-SiO_2 at 5.0 GPa. Geochimica et Cosmochimica Acta, 61(12):2367–2373, 1997.

B. T. C. Davis and J. L. England. Melting of forsterite up to 50 Kilobars. Journal of Geophysical Research, 69:1113–1116, 1964.

L. A. Davis and R.B. Gordon. Compression of mercury at high pressure. Journal of Chemical Physics, 46:2650, 1967.

N. P. de Koker, L. Stixrude, and B. B. Karki. Thermodynamics, structure, dynamics, and freezing of Mg_2SiO_4 liquid at high pressure. Geochimica et Cosmochimica Acta, 72:1427–1441, doi:10.1016/j.gca.2007.12.019, 2008a.

N. P. de Koker, L. Stixrude, and B. B. Karki. Self-consistent thermodynamic description of silicate liquids. to be submitted to Geophysical Journal International, 2008b.

D. B. Dingwell, R. Knoche, and S. L. Webb. A volume temperature relationship for liquid GeO_2 and some geophysically relevant derived parameters for network liquids. Physics and Chemistry of Minerals, 19:445–453, 1993.

P. I. Dorogokupets. Thermodynamic functions at zero pressure and their relation to equations of state of minerals. American Mineralogist, 85:329–337, 2000.

T. S. Duffy and T. J. Ahrens. Compressional sound velocity, equation of state, and constitutive response of shock-compressed magnesium oxide. Journal of Geophysical Research, 100(B1):529–542, 1995.

J. F. Elliott, M. Gleiser, and V. Ramakrishna. Thermochemistry of Steelmaking, Vol II. Addison-Wesley, 1963.

R. P. Feynman, N. Metropolis, and E. Teller. Equations of state of elements based on the generalized Fermi-Thomas theory. Physical Review, 75:1561–1572, 1949.

H. Flyvberg and H. G. Petersen. Error-estimates on averages of correlated data. Journal of Chemical Physics, 91:461–466, 1989.

G. P. Francis and M. C. Payne. Finite basis set corrections to total energy pseudopotential calculations. Journal of Physics - Condensed Matter, 2(19):4395–4404, 1990.

G. A. Gaetani, P. D. Asimow, and E. M. Stolper. Determination of the partial molar volume of SiO_2 in silicate liquids at elevated pressures and temperatures: A new experimental approach. Geochimica et Cosmochimica Acta, 62(14):2499–2508, 1998.

E. J. Garnero and D. V. Helmberger. A very slow basal layer underlying large-scale low-velocity anomalies in the lower mantle beneath the pacific: evidence from core phases. Physics of Earth and Planetary Interiors, 91:161–176, 1995.

M. S. Ghiorso. An equation of state for silicate melts. I. formulation of a general model. American Journal of Science, 304:637–678, 2004.

M. S. Ghiorso and R. O. Sack. Chemical mass transfer in magmatic processes IV. a revised and internally consistent thermodynamic model for the interpolation and extrapolation of liquid-solid equilibria in magmatic systems at elevated temperatures and pressures. Contributions to Mineralogy and Petrology, 119:197–212, 1995.

M. S. Ghiorso, M. M. Hirschmann, P. W. Reiners, and V. C. Kress. The pMELTS: A revision of MELTS for improved calculation of phase relations and major element partitioning related to partial melting of the mantle to 3 GPa. Geochemistry Geophysics Geosystems, 3(5):10.1029/2001GC000217, 2002.

M. S. Ghiorso, D. Nevins, and F. J. Spera. Molecular dynamics studies of $MgSiO_3$ liquid to 150 GPa: An equation of state (EOS), tracer diffusivities, and a detailed analysis of changes in atomic coordination statistics as a function of temperature and pressure. Eos Trans. AGU, 87(52):Fall Meeting Supplement, Abstract MR43B–1079, 2006.

M. J. Gillan, D. Alfe, J. P. Brodholt, L. Vočadlo, and G. D. Price. First-principles modelling of Earth and planetary materials at high pressures and temperatures. Reports on Progress in Physics, 69(8):2365–2441, 2006.

J. J. Gilvarry. The Lindemann and Grüneisen laws. Physical Review, 102:308–316, 1956.

P. Gomes Dacosta, O. H. Nielsen, and K. Kunc. Stress theorem in the determination of static equilibrium by the density functional method. Journal of Physics C - Solid State Physics, 19(17):3163–3172, 1986.

J. W. Greig. Immiscibility in silicate melts. American Journal of Science, 13(73): 1–44, 1927.

V. B. M. Hageman and H. A. J. Oonk. Liquid immiscibility in the $SiO_2 + MgO$, $SiO_2 + SrO$, $SiO_2 + LaO_3$, and $SiO_2 + Y_2O_3$ systems. Physics and Chemistry of Glasses, 27(5):194–198, 1986.

S. E. Haggerty and V. Sautter. Ultradeep (greater than 300 kilometers), ultramafic upper mantle xenoliths. Science, 248:993–996, 1990.

H. Halbach and N. D. Chatterjee. An empirical Redlich-Kwong-type equation of state for water to 1,000 °C and 100 Kbar. Contributions to Mineralogy and Petrology, 79:337–345, 1982.

T. C. Hanks and D. L. Anderson. The eartly thermal history of the earth. Physics of the Earth and Planetery Interiors, 2:19–29, 1969.

D. L. Heinz and R. Jeanloz. Measurement of the melting curve of $Mg_{0.9}Fe_{0.1}SiO_3$ at lower mantle conditions and its geophysical implications. Journal of Geophysical Research, 92(B11):11437–11444, 1987.

P. C. Hess. Polymerization model for silicate melts. In R. B. Hargraves, editor, Physics of Magmatic Processes, pages 3–48. Princeton University Press, Princeton, NJ, 1980.

P. C. Hess. Thermodynamic mixing properties and the structure of silicate melts. In J. F. Stebbins, P. F. McMillan, and D. B. Dingwell, editors, Structure, Dynamics and Properties of Silicate Melts, volume 32 of Review in Mineralogy and Geochemistry, pages 145–189. Mineralogical Society of America, Washington, D.C., 1995.

D. G. Hicks, T. R. Boehly, J. H. Eggert, J. E. Miller, P. M. Celliers, and G. W. Collins. Dissociation of liquid silica at high pressures and temperatures. Physical Review Letters, 97:doi:10.1103/PhysRevLett.97.025502, 2006.

A. M. Hofmeister. Interatomic potentials calculated from equations of state: Limitation of finite strain to moderate K'. Geophysical Research Letters, 20(7):635–638, 1993.

P. Hohenberg and W. Kohn. Inhomogeneous electron gas. Physical Review B., 136: B864, 1964.

K. G. Holland and T. J. Ahrens. Melting of $(\mathrm{Mg},\mathrm{Fe})_2\mathrm{SiO}_4$ at the core-mantle boundary of the Earth. Science, 275:1623–1625, 1997.

T. Holland and R. Powell. A compensated-Redlich-Kwong (CORK) equation for volumes and fugacities of CO_2 and H_2O in the range 1 bar to 50 kbar and $100 - 1600\,^\circ\mathrm{C}$. Contributions to Mineralogy and Petrology, 109:265–273, 1991.

P. Hudon, I.-H. Jung, and D. R. Baker. Melting of β-quartz up to 2.0 GPa and thermodynamic optimization of the silica liquidus up to 6.0 GPa. Physics of the Earth and Planetery Interiors, 130:159–174, 2002.

D. G. Isaak, O. L. Anderson, and T. Goto. Measured elastic moduli of single-crystal MgO up to 1800 K. Physics and Chemistry of Minerals, 16:704–713, 1989.

I. Jackson and T. J. Ahrens. Shock wave compression of single-crystal forsterite. Journal of Geophysical Research, 84(B6):3039–3048, 1979.

R. Jeanloz and S. Morris. Temperature distribution in the crust and mantle. Annual Reviews of Earth and Planetary Sciences, 14:377–415, 1986.

R. Jeanloz and M. Roufosse. Anharmonic properties - ionic model of the effects of compression and coordination change. Journal of Geophysical Research, 87: 763–772, 1982.

B. B. Karki, R. M. Wentzcovitch, S. De Gironcoli, and S. Baroni. High-pressure lattice dynamics and thermoelasticity of MgO. Physical Review B, 61(13):8793–8800, 2000a.

B. B. Karki, R. M. Wentzcovitch, S. de Gironcoli, and S. Baroni. Ab initio lattice dynamics of $MgSiO_3$ perovskite at high pressure. Physical Review B, 62(22):14750–14756, 2000b.

B. B. Karki, L. Stixrude, and R. M. Wentzcovitch. High-pressure elastic properties of major materials of Earth's mantle from first principles. Reviews of Geophysics, 39:507–534, 2001.

B. B. Karki, D. Bhattarai, and L. Stixrude. First principles calculations of the structural, dynamical and electronic properties of liquid MgO. Physical Review B, 73:174208, 2006.

B. B. Karki, D. Bhattarai, and L. Stixrude. First-principles simulations of liquid silica: Structural and dynamical behavior at high pressure. Physical Review B, 76: 104205, 2007.

T. Kato and M. Kumazawa. Effect of high-pressure on the melting relation in the system Mg_2SiO_4-$MgSiO_3$. 1. eutectic relation up to 7 GPa. Journal of Physics of the Earth, 33(6):513–524, 1985.

J. Kieffer and C. A. Angell. Structural incompatibilities and liquid-liquid phase separation in molten binary silicates: A computer simulation. Journal of Chemical Physics, 90(9):4982–4991, 1989.

J. G. Kirkwood. Quantum statistics of almost classical assemblies. Physical Review, 44:31–37, 1933.

E. Knittle and R. Jeanloz. Melting curve of $(Mg, Fe)SiO_3$ perovskite to 96 GPa, evidence for a structural transition in lower mantle melts. Geophysical Research Letters, 16(5):421–424, 1989.

L. Knopoff and J. N. Shapiro. Pseudo-Grüneisen parameter of liquids. Physical Review B., 1:3893, 1970.

L Knopoff and R. J. Uffen. The densities of compounds at high pressures and the state of the Earth's interior. Journal of Geophysical Research, 59:471–484, 1954.

S. Kohara, K. Suzuya, K. Takeuchi, C. K. Loong, M. Grimsditch, J. K. R. Weber, J. A. Tangeman, and T. S. Key. Glass formation at the limit of insufficient network formers. Science, 303:1649–1652, 2004.

W. Kohn and L. J. Sham. Self-consistent equations including exchange and correlation effects. Physical Review, 140:1133, 1965.

G. Kresse and J. Furthmüller. Efficiency of ab-initio total energy calculations for metals and semiconductors using a plane-wave basis set. Computational Materials Science, 6:15–50, 1996.

G. Kresse and J. Hafner. Norm-conserving and ultrasoft pseudopotentials for first-row and transition-elements. Journal of Physics - Condensed Matter, 6:8245–8257, 1994.

J. D. Kubicki and A. C. Lasaga. Molecular-dynamics simulations of pressure and temperature effects on $MgSiO_3$ and Mg_2SiO_4 melts and glasses. Physics and Chemistry of Minerals, 17:661–673, 1991.

J. D. Kubicki, G. E. Muncill, and A. C. Lasaga. Chemical diffusion in melts on the $CaMgSi_2O_6$-$CaAl_2Si_2O_8$ join under high-pressures. Geochimica et Cosmochimica Acta, 54(10):2709–2715, 1990.

D. J. Lacks, D. B. Rear, and J. A. Van Orman. Molecular dynamics investigation of viscosity, chemical diffusivities and partial molar volumes of liquids along the MgO-SiO_2 join as functions of pressure. Geochimica et Cosmochimica Acta, 71: 1312–1323, 2007.

R. A. Lange. A revised model for the density and thermal expansivity of K_2O-Na_2O-CaO-MgO-Al_2O_3-SiO_2 liquids from 700 to 1900 K: extension to crustal magmatic temperatures. Contributions to Mineralogy and Petrology, 130:1–11, 1997.

R. A. Lange. The fusion curve of albite revisited and the compressibility of $NaAlSi_3O_8$ liquid with pressure. American Mineralogist, 88:109–120, 2003.

R. A. Lange. The density and compressibility of $KAlSi_3O_8$ liquid to 6.5 GPa. American Mineralogist, 92:114–123, 2007.

R. A. Lange and I. S. E. Carmichael. Densities of Na_2O-K_2O-CaO-MgO-FeO-Fe_2O_3-$Al_2O_3 - TiO_2$-SiO_2 liquids - new measurements and derived partial molar properties. Geochimica et Cosmochimica Acta, 51:2931–2946, 1987.

R. A. Lange and A. Navrotsky. Heat capacities of Fe_2O_3-bearing silicate liquids. Contributions to Mineralogy and Petrology, 110:311–320, 1992.

Y. Laudernet, J. Clérouin, and S. Mazevet. Ab initio simulations of the electrical and optical properties of shock-compressed SiO_2. Physical Review B, 70:165108, 2004.

F. A. Lindemann. über die berechnung molekularer eigenfrequenzen. Physikalische Zeitschrift, 11:609–612, 1910.

S. N. Luo, J. L. Mosenfelder, P. D. Asimow, and T. J. Ahrens. Direct shock wave loading of stishovite to 235 GPa: Implications for perovskite stability relative to an oxide assemblage at lower mantle conditions. Geophysical Research Letters, 29 (14):36, 2002.

S. N. Luo, J. A. Akins, T. J. Ahrens, and P. D. Asimow. Shock-compressed $MgSiO_3$ glass, enstatite, olivine, and quartz: Optical emission, temperatures, and melting. Journal of Geophysical Research, 109:B05205, 2004.

C. H. P. Lupis. Chemical Thermodynamics of Materials. Prentice-Hall Inc., New York, 1983.

S. P. Marsh. LASL Shock Hugoniot Data. University of California Press, Berkeley, CA, 1980.

R. E. Marshak and H. A. Bethe. The generalized Thomas-Fermi method as applied to stars. Astrophysical Journal, 91:239–243, 1940.

B. Martin, F. J. Spera, and D. Nevins. Thermodynamic and structural properties of liquid Mg_2SiO_4 at high temperatures and pressure in the range $0 - 150$ GPa from molecular dynamics simulation. Eos Trans. AGU, 87(52):Fall Meeting Supplement, Abstract MR43B–1080, 2006.

K. N. Matsukage, Z. Jing, and S. Karato. Density of hydrous silicate melt at the conditions of Earth's deep upper mantle. Nature, 438:488–491, 2005.

D. McKenzie and M. J. Bickle. The volume and composition of melt generated by extension of the lithosphere. Journal of Petrolgy, 29(3):625–679, 1988.

P. McMillan. A Raman spectroscopic study of glasses in the system CaO-MgO-SiO_2. American Mineralogist, 69:645–659, 1984.

D. A. McQuarrie. Statistical Mechanics. University Science Books, Sausalito, CA, 1984.

N. D. Mermin. Thermal properties of inhomogeneous electron gas. Physical Review, 137:1441, 1965.

G. H. Miller, E. M. Stolper, and T. J. Ahrens. The equation of state of a molten komatiite. 1. shock wave compression to 36 GPa. Journal of Geophysical Research, 96(B7):11849–11864, 1991a.

G. H. Miller, E. M. Stolper, and T. J. Ahrens. The equation of state of a molten komatiite. 2. application to komatiite petrogenesis and the hadean mantle. Journal of Geophysical Research, 96(B7):11849–11864, 1991b.

H. J. Monkhorst and J. D. Pack. Special points for Brillouin-zone integrations. Physical Review B., 13(12):5188–5192, 1976.

M. Mookherjee, L. Stixrude, and B. B. Karki. Hydrous silicate melt at high pressure. Nature, in press, 2008.

R. M. More, K. H. Warren, D. A. Young, and G. B. Zimmerman. A new quitidian equation of state (QEOS) for hot dense matter. Physics of Fluids, 31(10):3059–3078, 1988.

J. L. Mosenfelder, P. D. Asimow, and T. J. Ahrens. Thermodynamic properties of Mg_2SiO_4 liquid at ultra-high pressures from shock measurements to 200 GPa on forsterite and wadsleyite. Journal of Geophysical Research, 112(B06208): doi:10.1029/2006JB004364, 2007.

R. L. Mozzi and B. E. Warren. The structure of vitreous silica. Journal of Applied Crystallography, 2:164–172, 1969.

A. Navrotsky, D. Ziegler, R. Oestrike, and P. Maniar. Calorimetry of silicate melts at 1773 K - measurement of enthalpies of fusion and of mixing in the systems diopside-anorthite-albite and anorthite-forsterite. Contributions to Mineralogy and Petrology, 101:122–130, 1989.

A. Ng, B. K. Godwal, J. Waterman, L. DaSilva, N. W. Ashcroft, and R. Jeanloz. Nonequilibrium shock behavior in quartz. Physical Review B, 44(10):4872–5876, 1991.

S. Nosé. A unified formulation of the constant temperature molecular dynamics methods. Journal of Chemical Physics, 81:511–519, 1984.

A. R. Oganov and P. I. Dorogokupets. All-electron and pseudopotential study of MgO: Equation of state, anharmonicity, and stability. Physical Review B, 67:doi: 10.1103/PhysRevB.67.224110, 2003.

A. R. Oganov, J. Brodholt, and G. D. Price. Ab initio elasticity and thermal equation of state of $MgSiO_3$ perovskite. Earth and Planetary Science Letters, 184:555–560, 2001a.

A. R. Oganov, J. P. Brodholt, and G. D. Price. The elastic constants of $MgSiO_3$ perovskite at pressures and temperatures of the Earth's mantle. Nature, 411:934–937, 2001b.

E. Ohtani. Chemical stratification of the mantle formed by melting in the early stage of the terrestrial evolution. Tectonophysics, 154:201–210, 1988.

E. Ohtani and M. Kumazawa. Melting of forsterite Mg_2SiO_4 up to 15 GPa. Physics of Earth and Planetary Interiors, 27:32–38, 1981.

E. Ohtani and H. Sawamoto. Melting experiment on a model chondritic mantle composition at 25 GPa. Geophysical Research Letters, 14(7):733–736, 1987.

E. Ohtani, A. Suzuki, and T. Kato. Flotation of olivine in the peridotite melt at high pressure. Proceedings of the Japan Academy. Series B, 69:23–28, 1993.

Y. I. Ol'Shanskii. Equilibria of two immiscible liquids. Doklady Akademii Nauk SSSR, 76:93–96, 1951.

A. Pavese. Pressure-volume-temperature equations of state: a comparative study based on numerical simulations. Physics and Chemistry of Minerals, 29:43–51, 2002.

A. C. Phillips. The Physics of Stars. John Wiley & Sons, Chichester, 1994.

K. S. Pitzer and S. M. Sterner. Equations of state valid continuously from zero to extreme pressures for H_2O and CO_2. Journal of Chemical Physics, 101(4):3111–3116, 1994.

D. C. Presnall and T. Gasparik. Melting of enstatite ($MgSiO_3$) from 10 to 16.5 GPa and the forsterite (Mg_2SiO_4) - majorite ($MgSiO_3$) eutectic at 16.5 GPa: Implications for the origin of the mantle. Journal of Geophysical Research, 95:15771–15777, 1990.

D. C. Presnall and M. J. Walter. Melting of forsterite, Mg_2SiO_4, from 9.7 to 16.5 GPa. Journal of Geophysical Research, 98:19777–19783, 1993.

D. C. Presnall, Y. H. Weng, C. S. Milholland, and M. J. Walter. Liquidus phase relations in the system $MgO - MgSiO_3$ at pressures up to 25 GPa - constraints on crystallization of a molten hadean mantle. Physics of the Earth and Planetery Interiors, 107:83–95, 1998.

O. Redlich and J. N. S. Kwong. On the thermodynamics of solutions. 5. an equation of state - fugacities of gaseous solutions. Chemical Reviews, 44(1):233–244, 1949.

J. E. Reid, B. T. Poe, D. C. Rubie, N. Zotov, and M. Wiedenbeck. The self-diffusion of silicon and oxygen in diopside ($CaMgSi_2O_6$) liquid up to 15 GPa. Chemical Geology, 174:77–86, 2001.

J. Revenaugh and R. Meyer. Seismic evidence of partial melt within a possibly ubiquitous low-velocity layer at the base of the mantle. Science, 277:670–673, 1997.

J. Revenaugh and S. A. Sipkin. Seismic evidence for silicate melt atop the 410 km mantle discontinuity. Nature, 369(6480):474–476, 1994.

P. Richet and Y. Bottinga. Thermochemical properties of silicate glasses and liquids: A review. Reviews of Geophysics, 24(1):1–25, 1986.

S. M. Rigden, T. J. Ahrens, and E. M. Stolper. Densities of liquid silicates at high pressures. Science, 226(4678):1071–1074, 1984.

S. M. Rigden, T. J. Ahrens, and E. M. Stolper. Shock compression of molten silicate: Results for a model basaltic composition. Journal of Geophysical Research, 93(B1): 367–382, 1988.

S. M. Rigden, T. J. Ahrens, and E. M. Stolper. High-pressure equation of state of molten anorthite and diopside. Journal of Geophysical Research, 94(B7):9508–9522, 1989.

B. Riley. The determination of melting points at temperatures above 2000° celcius. Revue international des hautes temperatures et des refractaires, 3(3):327–336, 1966.

M. L. Rivers and I. S. E. Carmichael. Ultrasonic studies of silicate melts. Journal of Geophysical Research, 92:9247–9270, 1987.

Y. Rosenfeld and P. Tarazona. Density functional theory and the asymptotic high density expansion of the free energy of classical solids and fluids. Molecular Physics, 95(2):141–150, 1998.

M. Ross. Generalized Lindemann melting law. Physical Review, 184(1):233–242, 1969.

L. Ruff and D. L. Anderson. Core formation, evolution and convection: A geophysical model. Physics of the Earth and Planetery Interiors, 21:181–201, 1980.

I. Saika-Voivod, F. Sciortino, and P. H. Poole. Computer simulations of liquid silica: Equation of state and liquid-liquid phase transition. Physical Review E, 63: doi:10.1103/PhysRevE.63.011202, 2001.

T. Sakamaki, A. Suzuki, and E. Ohtani. Stability of hydrous melt at the base of the Earth's upper mantle. Nature, 439:192–194, 2006.

G. Shen and P. Lazor. Measurement of melting temperatures of some minerals under lower mantle pressures. Journal of Geophysical Research, 100(B9):17699–17713, 1995.

J. C. Slater and H. M. Krutter. Thomas-Fermi method for metals. Physical Review, 47:559–568, 1935.

V. S. Solomatov and D. J. Stevenson. Nonfractional crystallization of a terrestrial magma ocean. Journal of Geophysical Research, 98(E3):5391–5406, 1993.

T. R. A. Song, D. V. Helmberger, and S. P. Grand. Low-velocity zone atop the 410 km seismic discontinuity in the northwestern United States. Nature, 427(6974): 530–533, 1994.

R. Span and W. Wagner. On the extrapolation behaviour of empirical equations of state. International Journal of Thermophysics, 18(6):1415–1443, 1997.

J. F. Stebbins and I. Farnan. Effects of high temperature on silicate liquid structure: A multinuclear NMR study. Science, 255(5044):586–589, 1992.

J. F. Stebbins, I. S. E. Carmichael, and L. K. Moret. Heat-capacities and entropies of silicate liquids and glasses. Contributions to Mineralogy and Petrology, 86: 131–148, 1984.

L. Stixrude. First principles theory of mantle and core phases. In R. T. Cygan and J. D. Kubicki, editors, Molecular Modeling Theory: Applications in the Geosciences, volume 42 of Review in Mineralogy and Geochemistry, pages 319–

343. Geochemical Society and Mineralogical Society of America, Washington, D.C., 2001.

L. Stixrude and M. S. T. Bukowinski. Fundamental thermodynamic relations and silicate melting with implications for the constitution of the D″. Journal of Geophysical Research, 95(B12):19311–19325, 1990a.

L. Stixrude and M. S. T. Bukowinski. A novel topological compression mechanism in a covalent liquid. Science, 250:541–543, 1990b.

L. Stixrude and B. B. Karki. Structure and freezing of $MgSiO_3$ liquid in the Earth's lower mantle. Science, 310:297–299, 2005.

L. Stixrude and C. Lithgow-Bertelloni. Thermodynamics of mantle minerals - i. physical properties. Geophysical Journal International, 162:610–632, 2005.

L. Stixrude and C. Lithgow-Bertelloni. Influence of phase transformations on lateral heterogeneity and dynamics in earth's mantle. Earth and Planetary Science Letters, 263:45–55, 2007.

E. M. Stolper, D. Walker, B. H. Hager, and J. F. Hays. Melt segregation from partially molten source regions - the importance of melt density and source region size. Journal of Geophysical Research, 86:6261–6271, 1981.

A. Strachan, T. Çağin, and W. A. Goddard III. Reply to comment on 'phase diagram of MgO from density-functional theory and molecular-dynamics simulations'. Physical Review B, 63:doi: 10.1103/PhysRevB.63.096102, 2001.

O. Sugino and R. Car. Ab-initio molecular-dynamics study of first-order phase-transitions - melting of silicon. Physical Review Letters, 74:1823–1826, 1995.

N. Sun. Magma in Earth's Lower Mantle: First Principle Molecular Dynamics Simulations of Silicate Liquids. PhD thesis, University of Michigan, 2008.

A. Suzuki and E. Ohtani. Density of peridotite melts at high pressure. Physics and Chemistry of Minerals, 30:449–456, 2003.

B. Svendsen and T. J. Ahrens. Shock-induced temperatures of MgO. Geophysical Journal of the Royal Astronomical Society, 91:667–691, 1987.

J. S. Sweeney and D. L. Heinz. Melting of iron-magnesium-silicate perovskite. Geophysical Research Letters, 20(9):855–858, 1993.

J. S. Sweeney and D. L. Heinz. Laser-heating through a diamond-anvil cell: Melting at high pressures. In M. H. Manghnani and T. Yagi, editors, Properties of Earth and Planetary Materials at High Pressure and Temperature, Geophysical Monograph 101, pages 197–213. American Geophysical Union, Washington, D.C., 1998.

J. A. Tangeman, B. L. Phillips, A. Navrotsky, J. K. R. Weber, A. D. Hixson, and T. S. Key. Vitreous forsterite (Mg_2SiO_4): Synthesis, structure, and thermochemistry. Geophysical Research Letters, 28:2517–2520, 2001.

J. B. Thompson Jr. Thermodynamic properties of simple solutions. Researches in Geochemistry, 2:340–361, 1967.

J. W. Tomlinson, M. S. R. Heynes, and J. O. Bockris. The structure of liquid silicates, part 2. molar volumes and expansivities. Transations of the Faraday Society, 54:1822–1833, 1958.

W. B. Tonks and H. J. Melosh. Magma ocean formation due to giant impacts. Journal of Geophysical Research, 98(E3):5319–5333, 1993.

Y. S. Touloukian, R. K. Kirby, E. R. Taylor, and T. Y. R. Lee. Thermophysical Properties of Matter - the TPRC Data Series. Volume 13. Thermal Expansion - Nonmetallic Solids. IFI/Plenum, New York, 1977.

A. Trave, P. Tangney, S. Scandolo, A. Pasquarello, and R. Car. Pressure-induced structural changes in liquid SiO_2 from ab initio simulations. Physical Review Letters, 89(24):245504, 2002.

R. G. Trønnes and D. J. Frost. Peridotite melting and mineral-melt partitioning of major and minor elements at $22 - 24.5\,\mathrm{GPa}$. Earth and Planetary Science Letters, 197:117–131, 2002.

H. C. Urey. The cosmic abundances of potassium, uranium and thorium and the heat balances of the earth, the moon, and mars. Proceedings of the National Academy of Sciences of the United States of America, 41(3):127–144, 1955.

J. D. van der Waals. Over de Continuiteit van den Gas- en Vloeistoftoestand. A. W. Sijthoff, Leiden, 1873.

M. S. Vassiliou and T. J. Ahrens. Hugoniot equation of state of periclase to 200 GPa. Geophysical Research Letters, 8(7):729–732, 1981.

L. Vočadlo and G. D. Price. The melting of MgO - computer calculations via molecular dynamics. Physics and Chemistry of Minerals, 23:42–49, 1996.

L. Vočadlo, D. Alfe, M. J. Gillan, and G. D. Price. The properties of iron under core conditions from first principles calculations. Physics of Earth and Planetary Interiors, 140:101–125, 2003.

H. S. Waff. Pressure-induced coordination changes in magmatic liquids. Geophysical Research Letters, 2(5):193–196, 1975.

D. C. Wallace. Statistical Physics of Crystals and Liquids: A Guide to Highly Accurate Equations of State. World Scientific, Singapore, 2002.

J. T. K. Wan, T. S. Duffy, S. Scandolo, and R. Car. First-principles study of density, viscosity, and diffusion coefficients of liquid $MgSiO_3$ at conditions of the Earth's deep mantle. Journal of Geophysical Research, 112:B03208, 2007.

B. E. Warren and J. Biscoe. Fourier analysis of x-ray patterns of soda-silica glass. Journal of the American Ceramic Society, 21(7):259–265, 1938.

Y. Waseda and J. M. Toguri. The structure of molten binary silicate systems CaO-SiO_2 and MgO-SiO_2. Metallurgical Transactions B, 8(4):563–568, 1977.

E. A. Wasserman, D. A. Yuen, and R. Rustad. Compositional effects on the transport and thermodynamic properties of MgO-SiO_2 mixtures using molecular dynamics. Physics of the Earth and Planetery Interiors, 77:189–203, 1993.

J. P. Watt and T. J. Ahrens. Shock compression of single-crystal forsterite. Journal of Geophysical Research, 88(B11):9500–9512, 1983.

E. Wigner. On the quantum correction for thermodynamic equilibrium. Physical Review, 40:749–759, 1932.

Q. Williams. Molten $(Mg_{0.88}Fe_{0.12})_2SiO_4$ at lower mantle conditions - melting products and structure of quenched glasses. Geophysical Research Letters, 17:635–638, 1990.

Q. Williams and E. J. Garnero. Seismic evidence for partial melt at the base of Earth's mantle. Science, 273:1528–1530, 1996.

Q. Williams and R. Jeanloz. Spectroscopic evidence for pressure-induced coordination changes in silicate glasses and melts. Science, 239:902–905, 1988.

Q. Williams, P. McMillan, and T. F. Cooney. Vibrational spectra of olivine composition glasses: the $\mathrm{Mg} - \mathrm{Mn}$ join. Physics and Chemistry of Minerals, 16:352–359, 1989.

Q. Williams, E. Knittle, and R. Jeanloz. The high-pressure melting curve of iron - a technical discussion. Journal of Geophysical Research, 96(B2):2171–2184, 1991.

G. H. Wolf and R. Jeanloz. Lindemann melting law - anharmonic correction and test of its validity for minerals. Journal of Geophysical Research, 89:7821–7835, 1984.

G. H. Wolf, D. J. Durben, and P. F. McMillan. High-pressure Raman spectroscopic study of sodium tetrasilicate ($Na_2Si_4O_9$) glass. Journal of Chemical Physics, 93 (4):2280–2288, 1990.

X. Xue, J. F. Stebbins, M. Kanzaki, P. F. McMillan, and B. Poe. Pressure-induced silicon coordination and tetrahedral structural changes in alkali oxide-silica melts up to 12 GPa: NMR, Raman, and infrared spectroscopy. American Mineralogist, 76:8–26, 1991.

I.-C. Yeh and G. Hummer. System-size dependence of diffusion coefficients and viscosities from molecular dynamics simulations with periodic boundary conditions. Journal of Physical Chemistry B, 108:15873–15879, 2004.

D. A. Young and E. M. Corey. A new global equation of state model for hot, dense matter. Journal of Applied Physics, 78(6):3748–3755, 1995.

A. Zerr and R. Boehler. Melting of $(\mathrm{Mg}, \mathrm{Fe})\mathrm{SiO}_3$-perovskite to 625 Kilobars: Indication of a high melting temperature in the lower mantle. Science, 262:553–555, 1993.

A. Zerr and R. Boehler. Constraints on the melting temperature of the lower mantle from high-pressure experiments on MgO and magnesiowüstite. Nature, 371:506–508, 1994.

J. Zhang, R. C. Liebermann, T. Gasparik, and C. T. Herzberg. Melting and subsolidus relations of SiO_2 at $9-14$ GPa. Journal of Geophysical Research, 98(B11): 19785–19793, 1993.

Y. Zhang, G. Guo, K. Refson, and Y. Zhao. Finite-size effect at both high and low temperatures in molecular dynamics calculations of the self-diffusion coefficient and viscosity of liquid silica. Journal of Physics - Condensed Matter, 16:9127–9135, 2004.

Y. Zhou and G. H. Miller. Constraints from molecular dynamics on the liquidus and solidus of the lower mantle. Geochimica et Cosmochimica Acta, 61(14):2957–2976, 1997.